

## **Capítulo 5 Lentes multiplexadas**

Otra aproximación diferente de la mostrada en el capítulo anterior para modificar el perfil de intensidad a lo largo del eje óptico consiste en la implementación simultánea de lentes difractivas de focales distintas en un mismo LCSLM. De este modo es posible incrementar la profundidad de foco si lentes con distancias focales próximas producen distribuciones de amplitud a lo largo del eje que se solapan. Como las lentes difractivas de Fresnel presentan valores sólo de fase, se pueden implementar directamente en un modulador sólo de fase, sin necesidad de codificación alguna. Esto supone una ventaja respecto al método descrito en el capítulo 4, ya que los únicos órdenes de difracción que aparecen en el plano imagen y en los planos desenfocados son los debidos a la estructura pixelada del modulador. Con el LCSLM utilizado en este trabajo, estos órdenes están suficientemente separados como para poder trabajar con imágenes extensas.

En el presente capítulo se proponen tres métodos diferentes para la implementación de múltiples lentes de Fresnel en un LCSLM en configuración de modulación sólo de fase. El primer método consiste en la distribución de las lentes entre diferentes sectores, el segundo consiste en la distribución de las lentes en anillos de diferentes radios y áreas iguales y, por último, se propone su distribución por grupos de píxeles distribuidos de manera aleatoria. En el apartado 5.1 se explican en detalle estos métodos de multiplexado. En los siguientes apartados se ha evaluado experimentalmente la respuesta de cada uno de los métodos de multiplexado en relación al incremento de la DOF de un sistema y a la respuesta transversal del sistema en los diferentes planos.

El LCSLM utilizado es el descrito en el apartado 2.3. Se trata de un modulador SONY LCX012BL extraído de un videoproyector SONY modelo VPL-V500, con resolución VGA. Las lentes generadas tienen 480 píxeles de diámetro, que equivalen a 19,68 mm.

Al muestrear una lente de Fresnel para implementarla en un modulador pixelado aparecen múltiples lentes si la frecuencia de muestreo es menor que la frecuencia de Nyquist. Para reducir este efecto, las lentes que se han diseñado en este trabajo tienen distancias focales del orden de 1 m para la línea violeta del láser de Argón ( $\lambda=458$  nm). En la Figura 5.1 mostramos una lente de Fresnel de 1 m de focal para esa longitud de onda. Las estructuras circulares adicionales que aparecen en la imagen son debidas a la resolución limitada del muestreo y de las técnicas de impresión.

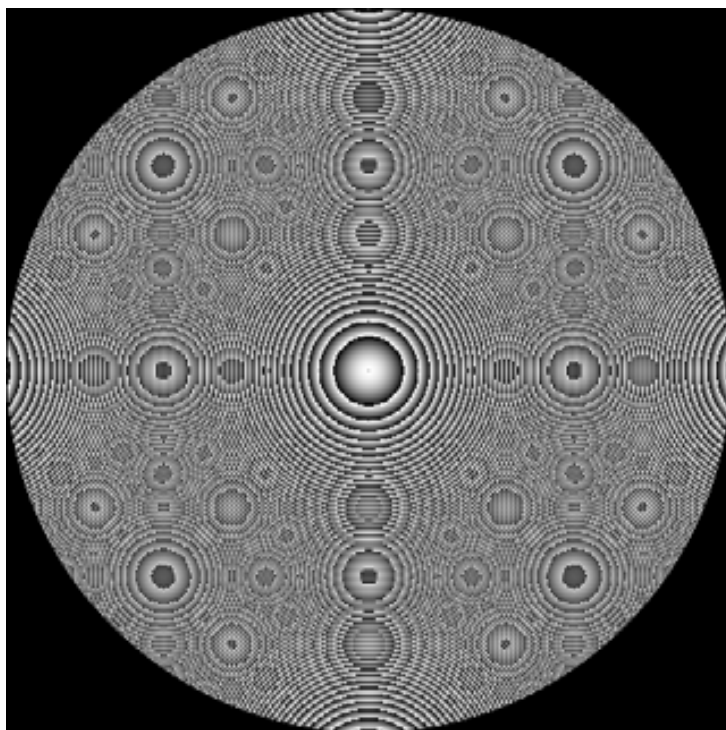


Figura 5.1. Lente de Fresnel de 1m de focal para  $\lambda=458$ nm. Las estructuras circulares adicionales que aparecen en la imagen son debidas a las limitaciones en la resolución.

Para generar las lentes multiplexadas se ha escogido un conjunto de lentes que abarca las focales de 920mm a 1080mm, con un rango en las distancias focales de 16 cm de profundidad. En la Figura 5.2 se presenta una muestra de las lentes de Fresnel utilizadas. En los casos en que se han multiplexado 33 lentes se han

utilizado todas las lentes del conjunto, con focales  $f=920, 925, 930, \dots, 1080\text{mm}$ . Para los casos en que se han multiplexado 17 lentes se han utilizado las de focales  $f = 920, 930, \dots, 1080 \text{ mm}$ . Y en aquellos casos en que se han multiplexado 9 lentes se han utilizado las de focales  $f = 920, 940, \dots 1080 \text{ mm}$ .

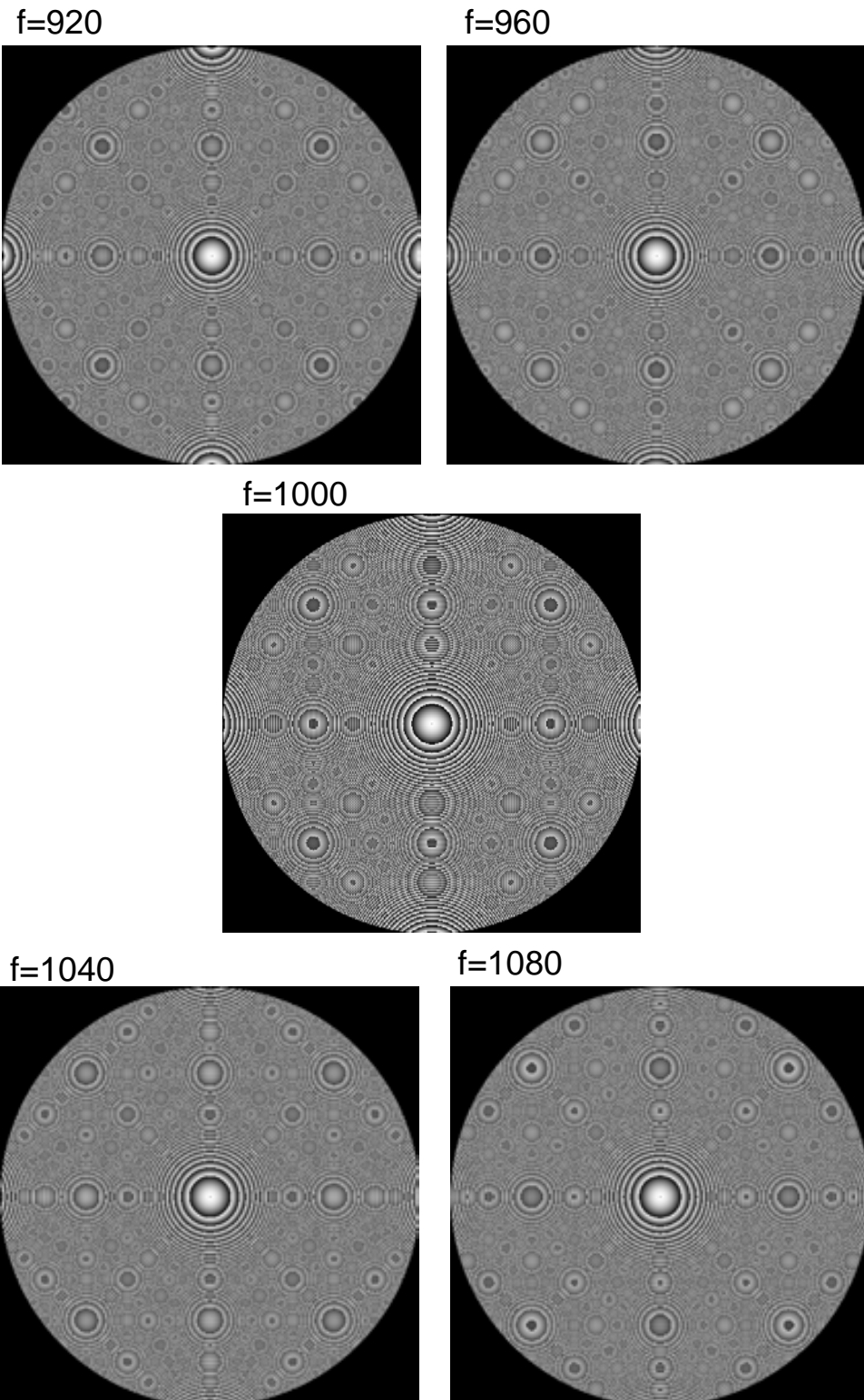


Figura 5.2. Conjunto de lentes de Fresnel de diferentes focales. Las distancias focales están expresadas en mm.

Una vez diseñadas las lentes multiplexadas se han adaptado a la respuesta del modulador según el polinomio de ajuste (*Look Up Table*) obtenido experimentalmente, tal y como se describe en el apartado 2.3. Mediante esta adaptación el valor de voltaje o nivel de gris enviado a cada celda del modulador se traduce en el valor de fase más cercano posible al valor deseado.

En la Figura 5.3 se observa la función de la lente SL de la Figura 5.1 adaptada a la respuesta del modulador según el polinomio de ajuste.

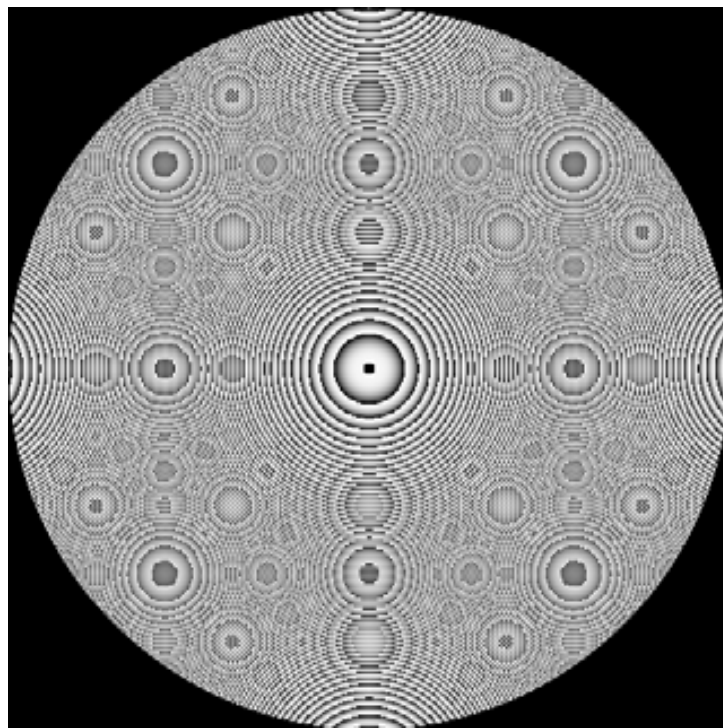


Figura 5.3. Lente sencilla SL de  $f=1000$  mm adaptada al polinomio de respuesta del modulador.

En los apartados 5.4, 5.5 y 5.6 se muestran los resultados obtenidos con cada método para la PSF a diferentes distancias del sistema y para el perfil de intensidad a lo largo del eje óptico.

En el apartado 5.7 se ha calculado la MTF numérica con multiplexado aleatorio, el más satisfactorio en términos de incremento de la DOF y uniformidad de la PSF, y se ha estudiado la respuesta del sistema para la imagen de un objeto extenso con este tipo de multiplexado.

## 5.1 Métodos de multiplexado

Se muestran a continuación los tres métodos de multiplexado utilizados para generar las lentes.

### 5.1.1 Método de multiplexado por sectores

La técnica propuesta de multiplexado por sectores consiste en asignar a cada una de las  $N$  lentes de diferentes focales un número  $p$  de sectores en la lente multiplexada. La superficie del SLM correspondiente a la lente multiplexada se divide en  $p \times N$  sectores de igual área tal como muestra la Figura 5.4, donde cada trama representa una focal distinta. Los sectores se numeran desde  $k=1$  hasta  $k=p \times N$ , de manera que los valores de transmisión de fase de los píxeles del sector  $k$  se toman de los píxeles correspondientes de la lente  $k \% p$  ( $k$  módulo  $p$ ). Es decir, los sectores  $(1, N+1, 2N+1, \dots)$  se asignan a la lente 1; los sectores  $(j, N+j, 2N+j, \dots)$  a la lente  $j$ , y así sucesivamente.

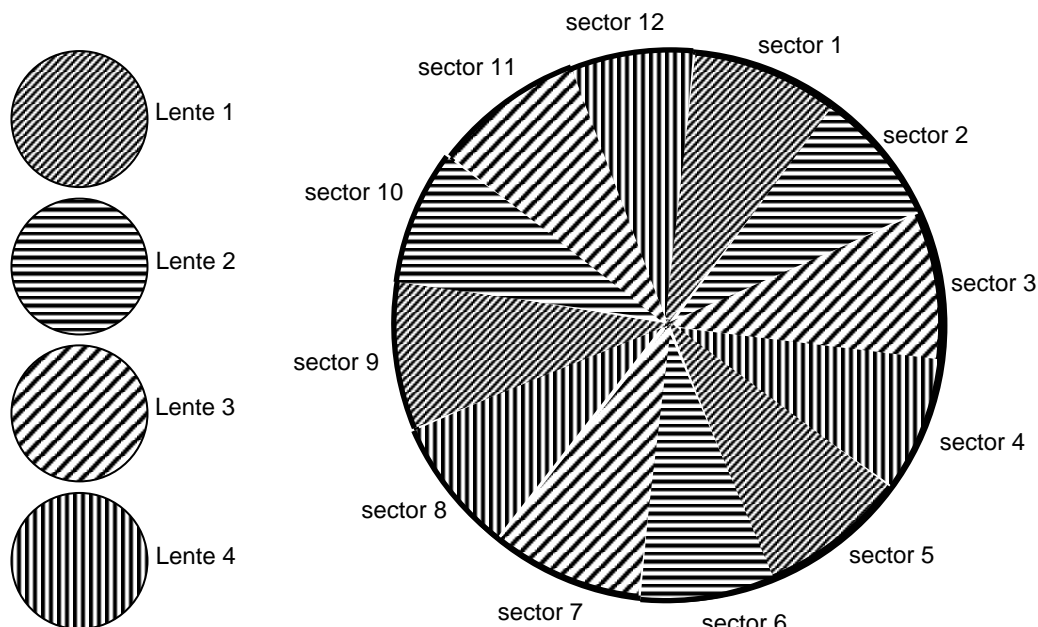


Figura 5.4. Esquema de la técnica de multiplexado por sectores para  $N=4$  lentes y  $p=3$  sectores por lente.  
Cada trama representa una lente de diferente focal.

La Figura 5.5 muestra una lente multiplexada construida mediante la técnica de multiplexado por sectores que se describe en este subapartado. Se han utilizado 9 lentes de focales distintas. En este caso el número de sectores por lente es  $p=1$ .

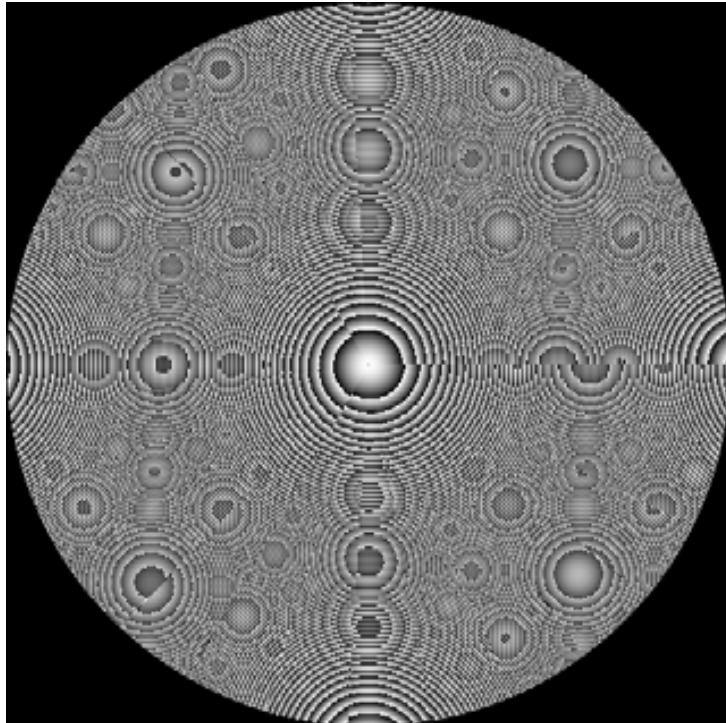


Figura 5.5. Conjunto de  $N=9$  lentes multiplexadas por sectores. En este caso a cada lente se le ha asignado un único sector,  $p=1$ .

### 5.1.2 Método de multiplexado por anillos

En la técnica de multiplexado basada en anillos la apertura se divide en  $p \times N$  anillos de igual área, y cada anillo se asigna a una lente con una distancia focal particular, según se muestra en la Figura 5.6. De manera equivalente a como se distribuyen las lentes entre los sectores en el método explicado en el apartado anterior, los anillos se numeran desde 1 hasta  $p \times N$ , de modo que los valores de transmisión de fase de los píxeles del anillo  $k$  se toman de los píxeles correspondientes de la lente  $k \% p$ . Es decir, los anillos  $(1, N+1, 2N+1, \dots)$  se asignan a la lente 1; los anillos  $(j, N+j, 2N+j, \dots)$  a la lente  $j$ , y así sucesivamente.

La técnica presenta una limitación en el número de lentes que se pueden implementar en un modulador de píxeles rectangulares, ya que al aumentar el número de anillos se pierde el control del área que tienen los más exteriores.

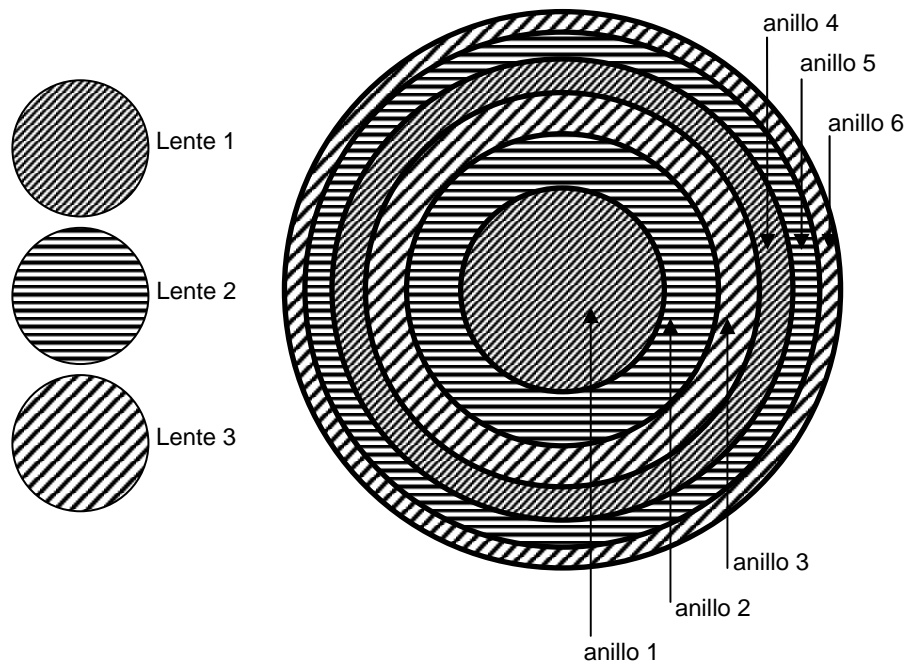


Figura 5.6. Esquema de la técnica de multiplexado por anillos para  $N=3$  lentes y  $p=3$  anillos por lente.  
Cada trama representa una lente de diferente focal.

La Figura 5.7 muestra una lente multiplexada construida mediante la técnica de multiplexado por anillos. Se han utilizado  $N=9$  lentes de focales distintas. En este caso el número de anillos por lente es  $p=3$ .

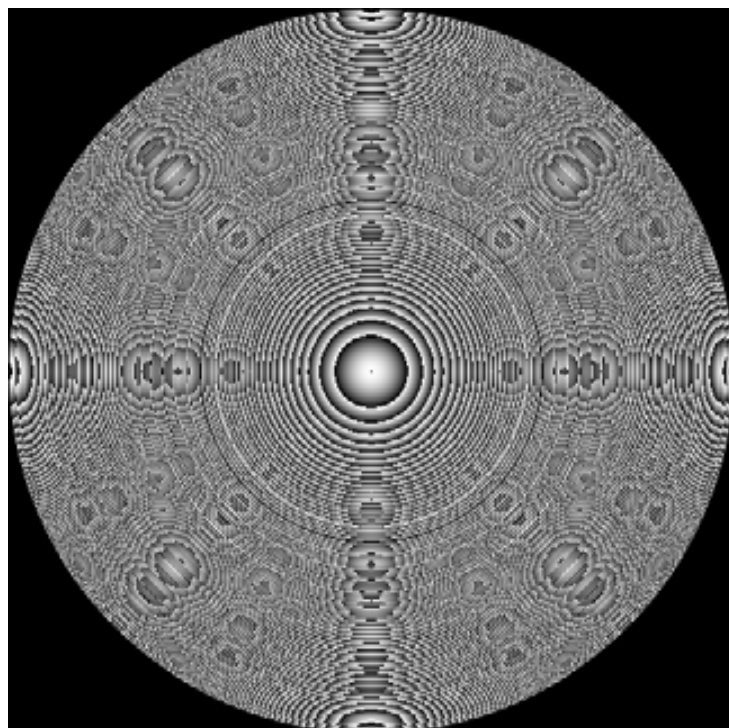


Figura 5.7. Conjunto de  $N=9$  lentes multiplexadas por anillos. A cada lente se le han asignado  $p=3$  anillos.

### 5.1.3 Método de multiplexado aleatorio

En la técnica de multiplexado aleatorio, la apertura se divide en subaperturas de  $p \times p$  píxeles. A cada subapertura se le asigna de manera aleatoria una de las lentes, y la transmisión de fase de los píxeles de esa subapertura se toma de la misma área en la lente correspondiente.

La asignación aleatoria se lleva a cabo de la siguiente manera. Para cada subapertura de la pupila se genera un número aleatorio  $k$  en el rango  $(0, N]$ . Si  $k$  está en el rango  $j - 1 < k \leq j$ , con  $j$  un número entero, entonces los valores de fase de los píxeles de esa subapertura corresponden a los de la misma zona de la lente  $j$ . En la Figura 5.8 se muestra un diagrama de esta técnica utilizada para construir una lente multiplexada de subaperturas de  $3 \times 3$  píxeles.

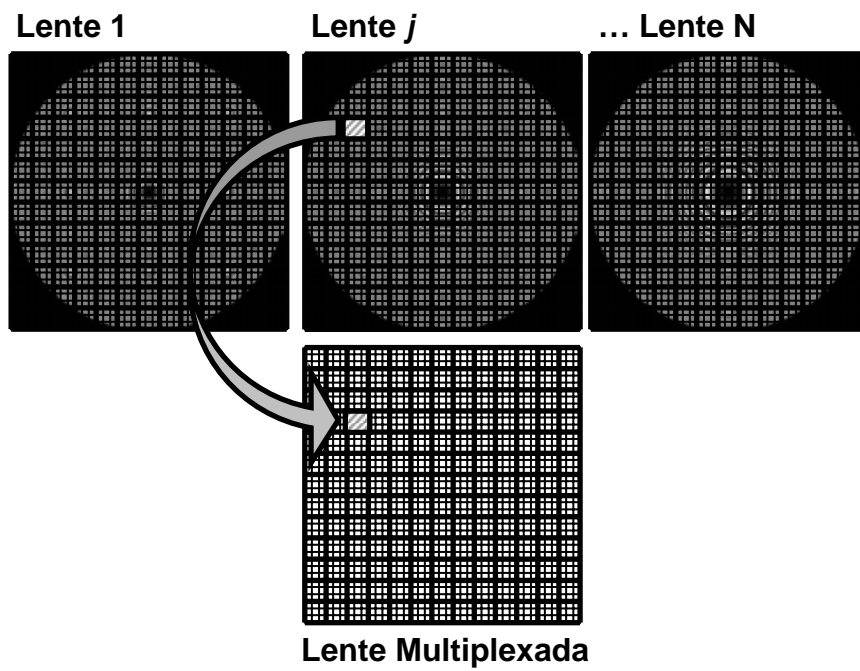


Figura 5.8. Esquema de la técnica de multiplexado aleatorio para construir una lente multiplexada de  $N$  lentes con subaperturas de  $3 \times 3$  píxeles.

La Figura 5.9 muestra una lente multiplexada construida mediante la técnica de multiplexado aleatorio que se describe en este subapartado. Se han utilizado 9 lentes de focales distintas. En este caso las subaperturas son de  $p=1$  píxeles.

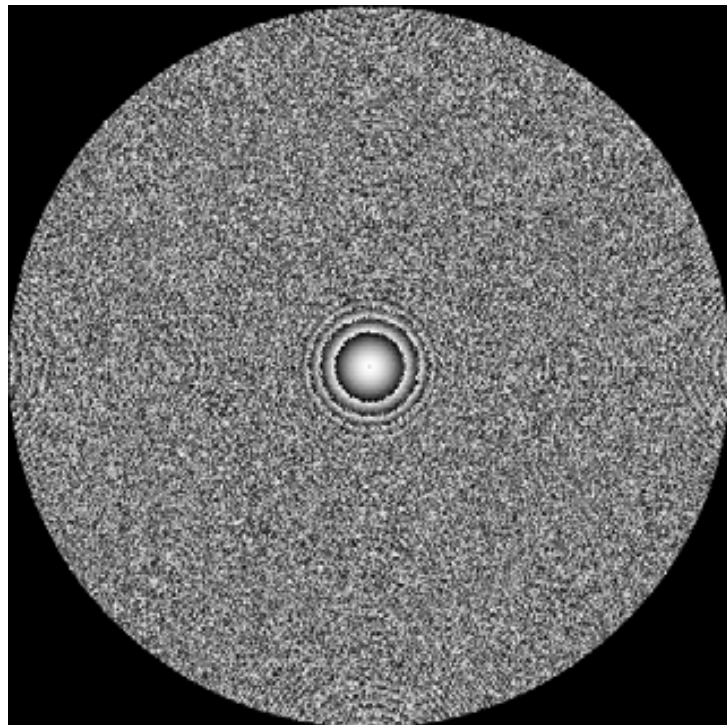


Figura 5.9. Conjunto de  $N=9$  lentes multiplexadas por la técnica de multiplexado aleatorio, con subaperturas de  $p=1$  pixel.

## 5.2 Diseño experimental para el estudio de la PSF

Para obtener la PSF de un sistema óptico con una pupila de salida consistente en una lente multiplexada diseñada según los diferentes métodos expuestos en el apartado 5.1 se ha utilizado el montaje experimental de la Figura 5.10.

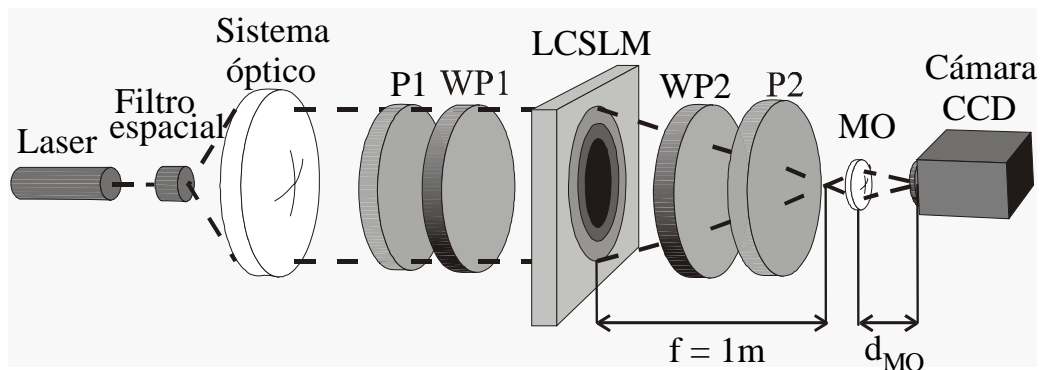


Figura 5.10. Montaje experimental para el estudio de las lentes multiplexadas. Las lentes se envían al LCSLM y enfocan la luz procedente del sistema óptico colimador. Los polarizadores  $P$  y las láminas retardadoras  $WP$  están configuradas de manera que el LCSLM actúa en configuración sólo de fase. Las imágenes son ampliadas mediante un objetivo de microscopio y capturadas mediante una cámara CCD.

Un haz láser de  $\lambda = 458$  nm incide de izquierda a derecha. Las posiciones de las láminas retardadoras (WP1 y WP2) y de los polarizadores lineales (P1 y P2) son las adecuadas para obtener una configuración de modulación sólo de fase en el modulador SONY LCX012BL según se expone en el apartado 2.3.

Un filtro espacial filtra y expande el haz del láser. La luz atraviesa un sistema óptico, un objetivo fotográfico zoom Nikon, que colima el haz procedente del filtro. Las lentes multiplexadas enviadas al LCSLM forman su imagen a diferentes distancias en el espacio imagen. Un objetivo de microscopio (OM) proyecta la imagen de la zona de interés de un plano perpendicular al eje óptico sobre una cámara CCD modelo PCO 2000 que la registra digitalmente, con un rango de 16.384 niveles de gris (14 bits). Desplazando el OM y la cámara CCD a lo largo del eje óptico se han capturado los planos transversales a diferentes distancias del LCSLM.

### **5.3 Resultados para una lente sencilla**

Con el fin de poder evaluar los resultados que se han obtenido para lentes multiplexadas con los diferentes métodos, se ha enviado previamente al modulador una lente de Fresnel sencilla (que denominaremos SL, de *single lens*) de  $f = 1000$  mm. Se ha obtenido para este caso el conjunto de PSF a diferentes distancias del modulador (Figura 5.11). Las imágenes tienen 0,3 mm de lado. En adelante, para poder observar la estructura transversal de las PSF en planos a diferentes distancias, para cada plano se han renormalizado los niveles de gris que representan las intensidades, de modo que el valor máximo correspondiese al blanco y el mínimo al negro. Las distancias z indicadas en la figura están en referencia a la distancia focal  $f=1000$  mm. Los valores negativos corresponden a posiciones más cercanas al SLM, mientras que los valores positivos corresponden a posiciones más alejadas.

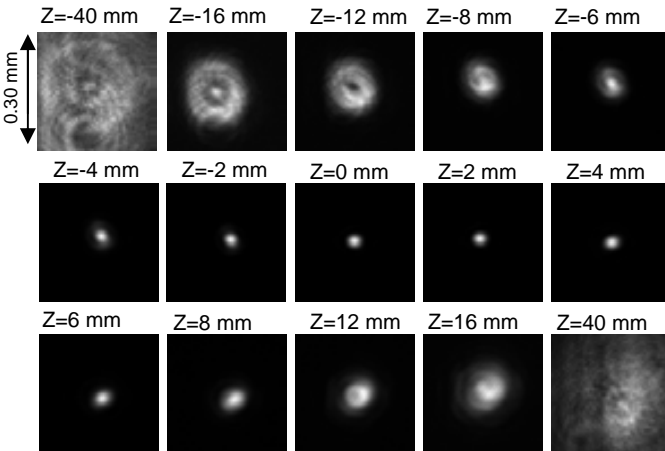


Figura 5.11. PSF a diferentes distancias del plano de mejor imagen para la lente sola SL,  $f=1000\text{mm}$ .  $Z=0\text{mm}$  corresponde a la distancia focal.

El perfil de intensidad a lo largo del eje para la SL se puede observar en la Figura 5.12. Corresponde al perfil para una lente convergente, una función  $\text{sinc}^2(z)$ , con un máximo pronunciado en  $Z = 0$  y dos lóbulos laterales. De hecho, se ha definido el origen  $Z = 0$  en el punto en que se obtiene el valor máximo de intensidad. La profundidad de foco, determinada a partir del FWHM, es de unos 10 mm. En la Figura 5.11 se puede apreciar cómo la anchura de la PSF es prácticamente constante en posiciones cercanas al punto focal ( $z = -4 \text{ mm}$  a  $z = 6 \text{ mm}$ ). Al decrecer la intensidad la PSF se hace más extensa y presenta ceros a ciertas distancias (por ejemplo, ver  $Z = -12 \text{ mm}$  en la Figura 5.11). La PSF presenta, en todos los planos, simetría axial.

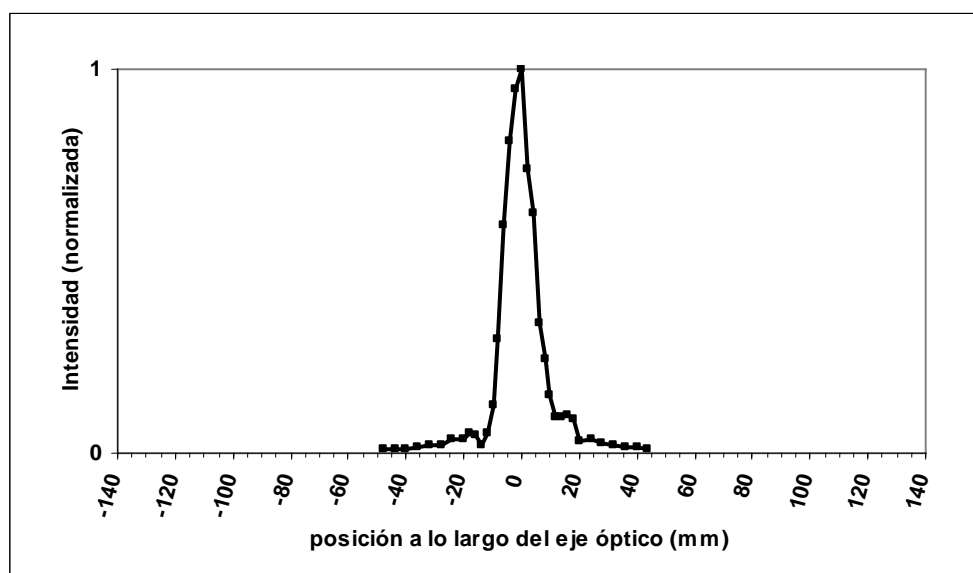
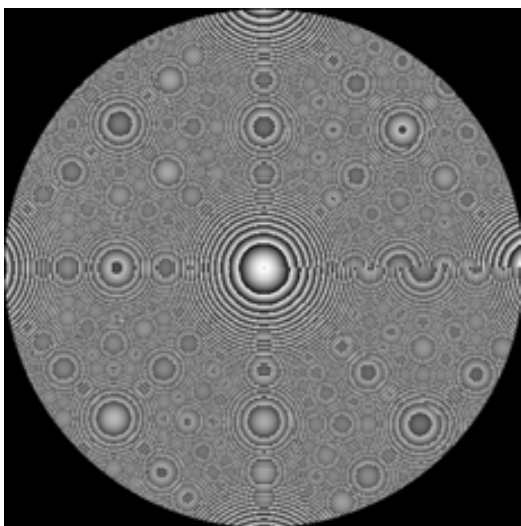


Figura 5.12. Intensidad a lo largo del eje óptico para la SL de  $f=1000 \text{ mm}$ . Los valores positivos son los más alejados del modulador.  $Z=0$  indica el plano focal imagen.

## 5.4 Resultados del multiplexado por sectores

Utilizando la técnica de multiplexado por sectores se han construido lentes multiplexadas de  $N=9$  y de  $N=33$  lentes, de un sector por cada lente, a las que llamaremos en adelante M9sect1 y M33sect1, con el primer número en referencia a la cantidad N de lentes y el segundo número en referencia a la cantidad p de sectores. En la Figura 5.13 se muestran las lentes multiplexadas construidas con este método.

(a) M9sect1



(b) M33sect1

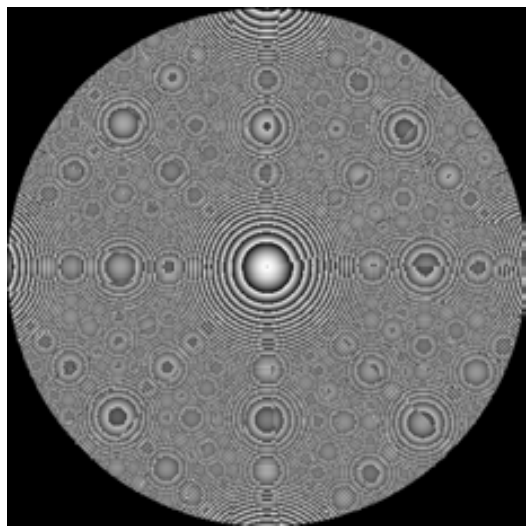
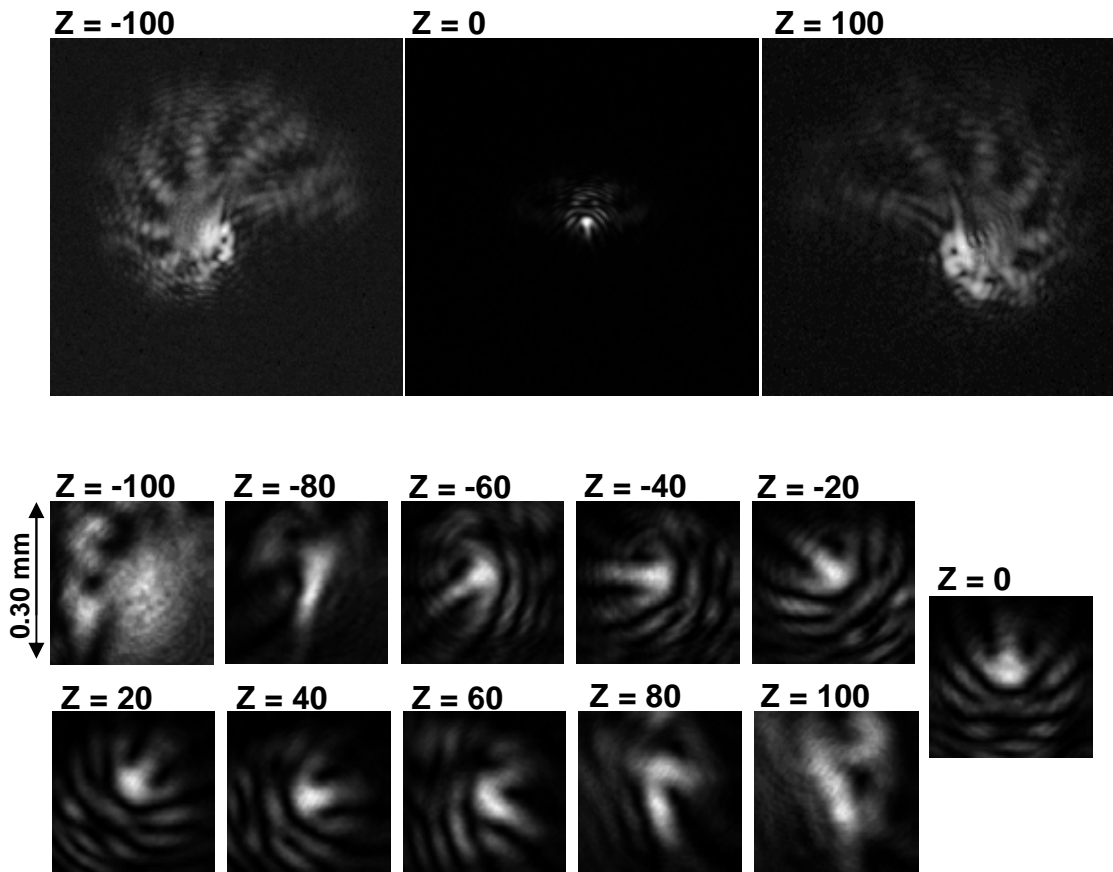


Figura 5.13. Lentes multiplexadas por sectores. (a) Lente M9sect1, constituida por 9 lentes con un sector por cada lente. (b) Lente M33sect1, constituida por 33 lentes con un sector por cada lente.

En la Figura 5.14 se muestran los resultados obtenidos al capturar las PSF a diferentes distancias del plano de mejor imagen, expresadas en milímetros, para la lente multiplexada M9sect1. En la fila superior se muestran tres capturas del plano transversal al eje óptico para  $z = -100$  mm,  $z = 0$  mm y  $z = +100$  mm sin ampliar las imágenes mediante el objetivo de microscopio. En estas capturas se puede apreciar la estructura espiral de las PSF en los planos desenfocados. La tabla de niveles de gris (*Look Up Table*) de estas imágenes ha sido modificada para hacer más evidente la estructura espiral. Esta estructura está causada por la división en sectores de la pupila, ya que cada sector focaliza en un plano diferente y entre dos sectores contiguos hay una rotación.

En la parte inferior de la Figura 5.14 se muestran las PSF obtenidas a diferentes distancias del plano focal, ampliadas mediante el objetivo de microscopio (por lo que están invertidas respecto a las de la fila superior). Muestran una distribución sin simetría axial. Con el fin de visualizar mejor la estructura transversal de las PSF, para cada plano se han renormalizado los niveles de gris que representan las intensidades, de modo que el valor máximo correspondiese al blanco y el mínimo al negro.



*Figura 5.14. PSF capturadas a diferentes distancias Z (en mm) del plano de mejor imagen, para la lente multiplexada M9sect1. Arriba, imágenes captadas por la CCD sin utilizar un objetivo de microscopio. La tabla de niveles de gris (LUT) de estas imágenes ha sido modificada para hacer más evidente la estructura espiral Abajo, la zona central de las PSF ampliada por el objetivo de microscopio. A fin de mostrar la estructura transversal para diferentes valores de Z, las intensidades representadas mediante los niveles de gris se han renormalizado en cada plano.*

En la Figura 5.15 se muestran los resultados obtenidos para la lente multiplexada por sectores M33sect1. Se observa que el hecho de incrementar el número de lentes representadas en la lente multiplexada por sectores no mejora la simetría de

la PSF, aunque sí reduce las estructuras transversales asimétricas en la zona central.

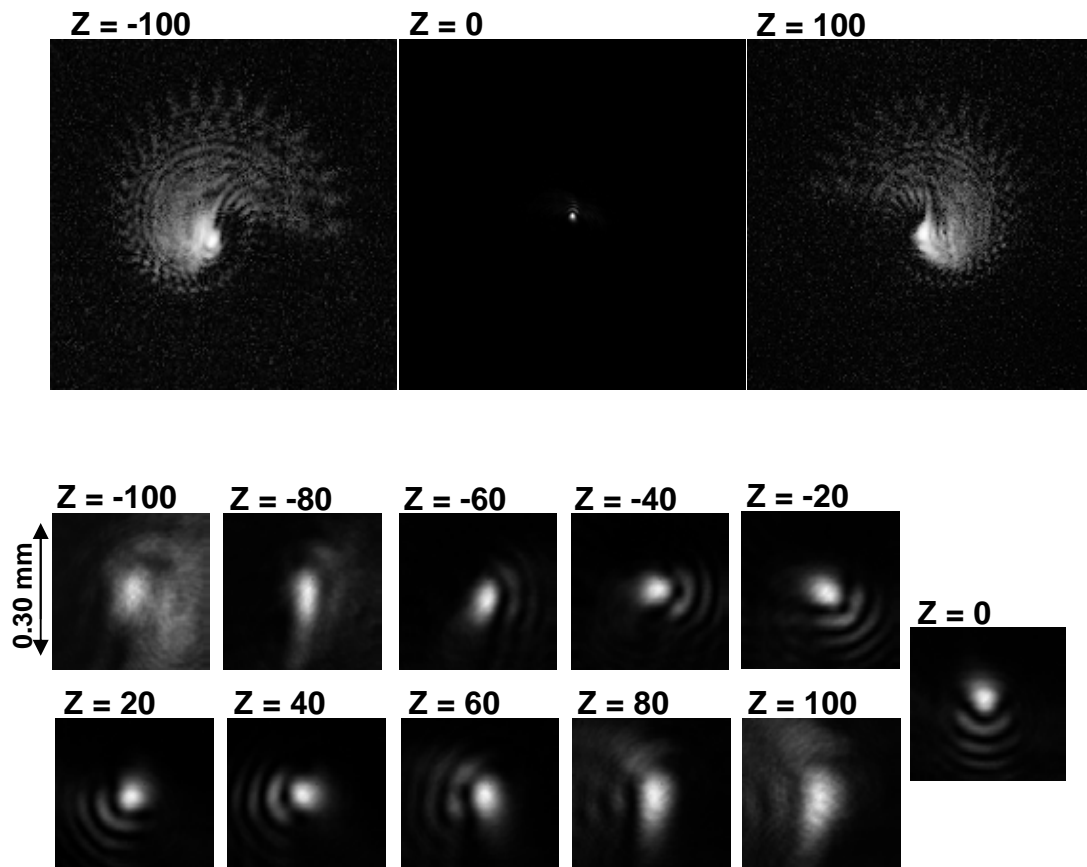


*Figura 5.15. PSF capturadas a diferentes distancias  $Z$  (en mm) del plano de mejor imagen, para la lente multiplexada M33sect1. Arriba, imágenes captadas por la CCD sin utilizar un objetivo de microscopio. La tabla de niveles de gris (LUT) de estas imágenes ha sido modificada para hacer más evidente la estructura. Abajo, la zona central de las PSF ampliada por el objetivo de microscopio. A fin de mostrar la estructura transversal para diferentes valores de  $Z$ , las intensidades representadas mediante los niveles de gris se han renormalizado en cada plano.*

En la parte inferior de la Figura 5.14 y de la Figura 5.15 se puede observar cómo se produce una rotación en la estructura a medida que nos desplazamos a lo largo de  $Z$ .

Debido a la falta de simetría axial observada en las PSF y a la presencia de estructuras demasiado extensas incluso en el plano de mejor imagen, no se ha calculado la intensidad a lo largo del eje para este tipo de multiplexado y se ha descartado su uso para incrementar la DOF, así como para obtener imágenes de objetos extensos.

## 5.5 Resultados del multiplexado por anillos

Se ha estudiado el comportamiento de lentes multiplexadas construidas mediante la técnica de multiplexado por anillos, con  $N=9$  y  $N=33$  lentes, y en cada caso con  $p=1$  y  $p=3$  anillos asignados a cada lente (en adelante M9ani1, M33ani1, M9ani3 y M33ani3, donde el primer número se refiere a la cantidad  $N$  de lentes y el segundo número hace referencia a la cantidad  $p$  de anillos asignados a cada lente).

En la Figura 5.16 se muestra el conjunto de lentes multiplexadas construidas mediante este método.

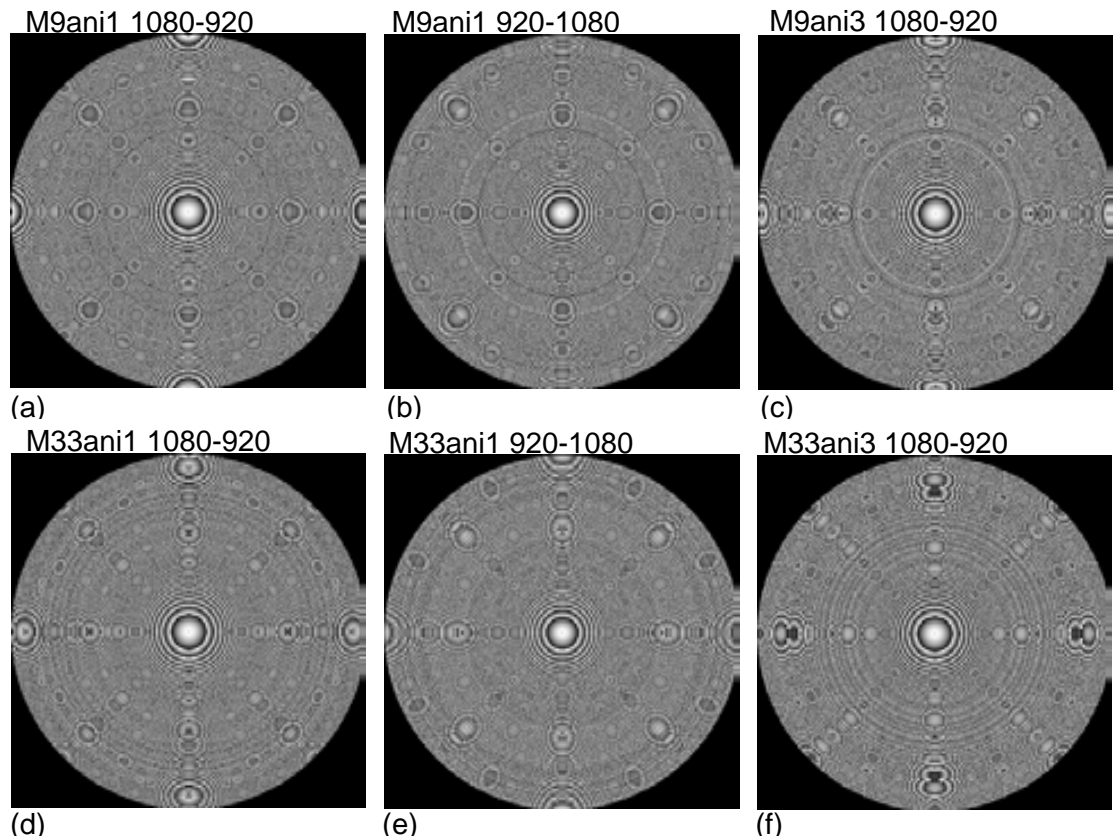


Figura 5.16. Lentes multiplexadas en anillos para 9 lentes (fila superior) y para 33 lentes (fila inferior). 1080-920 indica que las focales están ordenadas de manera que en el centro de la lente se encuentra la focal más larga (1080 mm), y en el perímetro la más corta (920 mm), y viceversa. (a),(b),(d) y (e) corresponden a un anillo por focal. (c) y (f) corresponden a 3 anillos por focal.

En la fila superior de la Figura 5.16 se muestran las lentes multiplexadas en anillos para 9 lentes. La Figura 5.16 (a) muestra la lente M9ani1, multiplexado de 9 lentes de focales distintas con un anillo asignado a cada lente. Los números

1080-920 indican que las focales están ordenadas de manera que en el centro de la lente se encuentra la focal más larga (1080 mm), y en el perímetro la más corta (920 mm). La Figura 5.16 (b) muestra una lente multiplexada con las mismas características, pero en este caso las focales están ordenadas de manera que en el centro de la lente se encuentra la focal más corta (920 mm), y en el perímetro la más larga (1080 mm). En la lente multiplexada de la Figura 5.16 (c) se asignan 3 anillos a cada focal.

En la fila inferior de la Figura 5.16 se muestran las lentes multiplexadas en anillos para 33 lentes. La Figura 5.16 (d) muestra la lente M33ani1, multiplexado de 33 lentes de focales distintas con un anillo asignado a cada lente, con la focal más larga ocupando el centro de la multiplexada. La Figura 5.16 (e) muestra una lente multiplexada con las mismas características que la anterior, pero con las focales en orden inverso. En la lente multiplexada de la Figura 5.16 (f) se asignan 3 anillos a cada focal.

Los resultados experimentales correspondientes a las lentes multiplexadas por anillos se mostrarán en las figuras que van desde la Figura 5.19 a la Figura 5.30. Se presentan las PSF obtenidas en diferentes planos transversales al eje óptico, así como los perfiles de intensidad a lo largo del eje para cada caso. Los valores de las curvas de intensidad están normalizados respecto al valor del máximo de intensidad para la lente SL.

Como veremos, en todos los casos se observa una diferencia, tanto en la estructura de las PSF como en el perfil de intensidad, para las posiciones  $Z>0$  respecto a las posiciones  $Z<0$ . Esto es debido a la influencia del orden de la distribución de las diferentes lentes entre los anillos, según si las focales más largas se sitúan hacia el exterior de la lente o a la inversa. Como se observa en la Figura 5.17 y en la Figura 5.18, la distribución de los rayos de luz no da resultados simétricos para valores  $Z<0$  y  $Z>0$ .

En el caso de las lentes multiplexadas con las focales más largas en el interior de la lente (Figura 5.17), la forma de las cáusticas implica que en los planos transversales para las focales situadas a  $Z<0$  aparecerán anillos bien definidos

rodeando el máximo central, mientras que para las focales más alejadas habrá mucha más concentración de luz en la zona más próxima al eje, lo que dará lugar a máximos de la PSF más amplios e intensos rodeados de anillos más difusos.

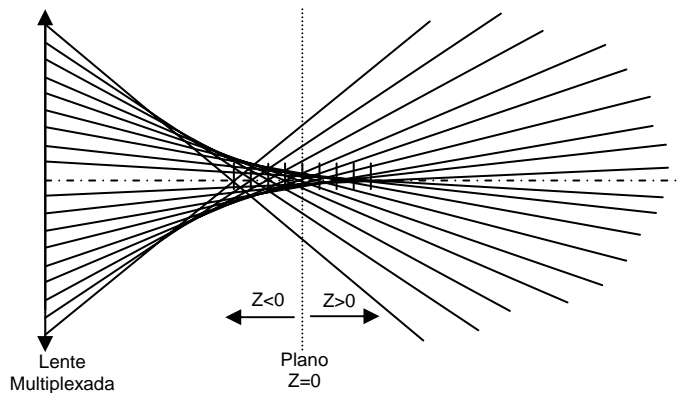


Figura 5.17. Esquema de la distribución de los rayos de luz a la salida de la lente multiplexada con las focales más largas situadas hacia el centro de la lente. Las líneas verticales en el eje representan las distancias focales de la lente. El plano  $Z=0$  representa el plano focal para la lente SL.

Por el contrario, si las focales largas se encuentran en las zonas exteriores de la lente (Figura 5.18), los planos transversales para las focales situadas a  $Z<0$  tendrán mucha más concentración de luz en la zona próxima al eje, lo que dará lugar a máximos de la PSF más intensos y amplios, con los anillos más difusos, mientras que para las focales más alejadas aparecerán anillos bien definidos y máximos centrales de menor diámetro.

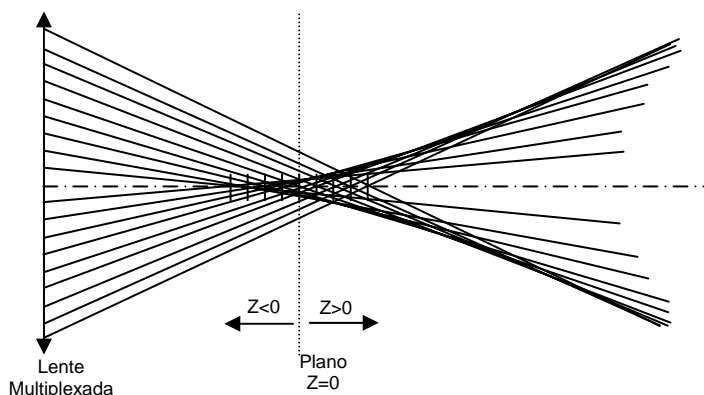


Figura 5.18. Esquema de la distribución de los rayos de luz a la salida de la lente multiplexada con las focales más cortas situadas hacia el centro de la lente. Las líneas verticales en el eje representan las distancias focales de la lente. El plano  $Z=0$  representa el plano focal para la lente SL.

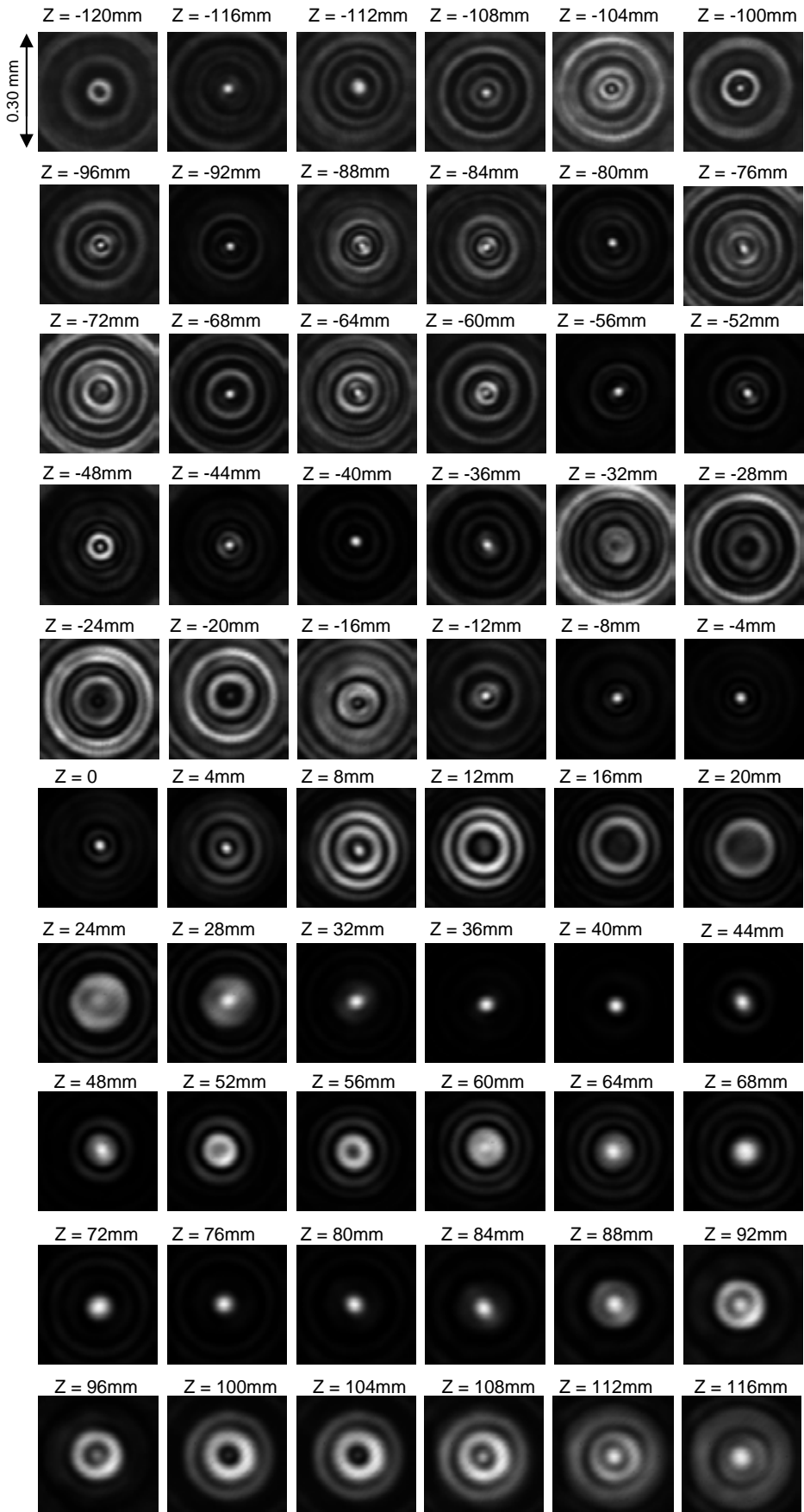


Figura 5.19. PSF experimentales obtenidas con la lente M9ani1. Las focales más largas están en el interior de la lente.

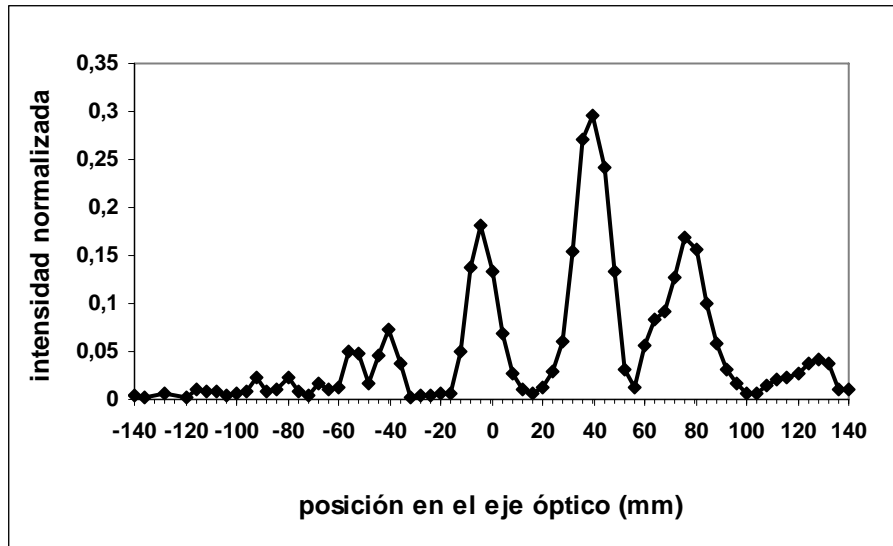


Figura 5.20 Perfil de intensidad a lo largo del eje óptico para la lente multiplexada M9ani1 con las focales largas en el interior de la lente. La intensidad está normalizada al valor máximo con la lente SL. El origen en el eje óptico corresponde al plano focal imagen para la lente SL.

En la Figura 5.19 se muestran los resultados experimentales de las PSF capturadas a diferentes distancias de la lente para la multiplexada M9ani1, es decir, construida a partir de 9 lentes de focales entre 920 y 1080 mm, mediante el sistema de multiplexado por anillos. En este caso las lentes están distribuidas de manera que la focal central corresponde a 1080 mm y el resto de las focales ocupan progresivamente los anillos desde el interior hacia el exterior. Se puede apreciar como, efectivamente, para  $Z>0$  el máximo central de cada PSF resulta más amplio y los anillos más difusos que para  $Z<0$ .

La Figura 5.20 muestra el perfil de intensidad a lo largo del eje óptico medido a partir de la intensidad central de las imágenes de la Figura 5.19. Aparecen oscilaciones en la intensidad correspondientes a las diferentes focales de las lentes que componen la multiplexada, con los valores más elevados de intensidad para los máximos situados en  $Z>0$ . El FWHM para cada uno de esos máximos es del orden del FWHM para la SL (ver Figura 5.12). Sin embargo, hay menos máximos de los que serían de esperar por el número de lentes que componen esta multiplexada (9 lentes con focales situadas en -80 mm, -60 mm, ..., 80 mm), posiblemente a causa de la interferencia destructiva producida entre los diferentes haces que focalizan a diferentes distancias.

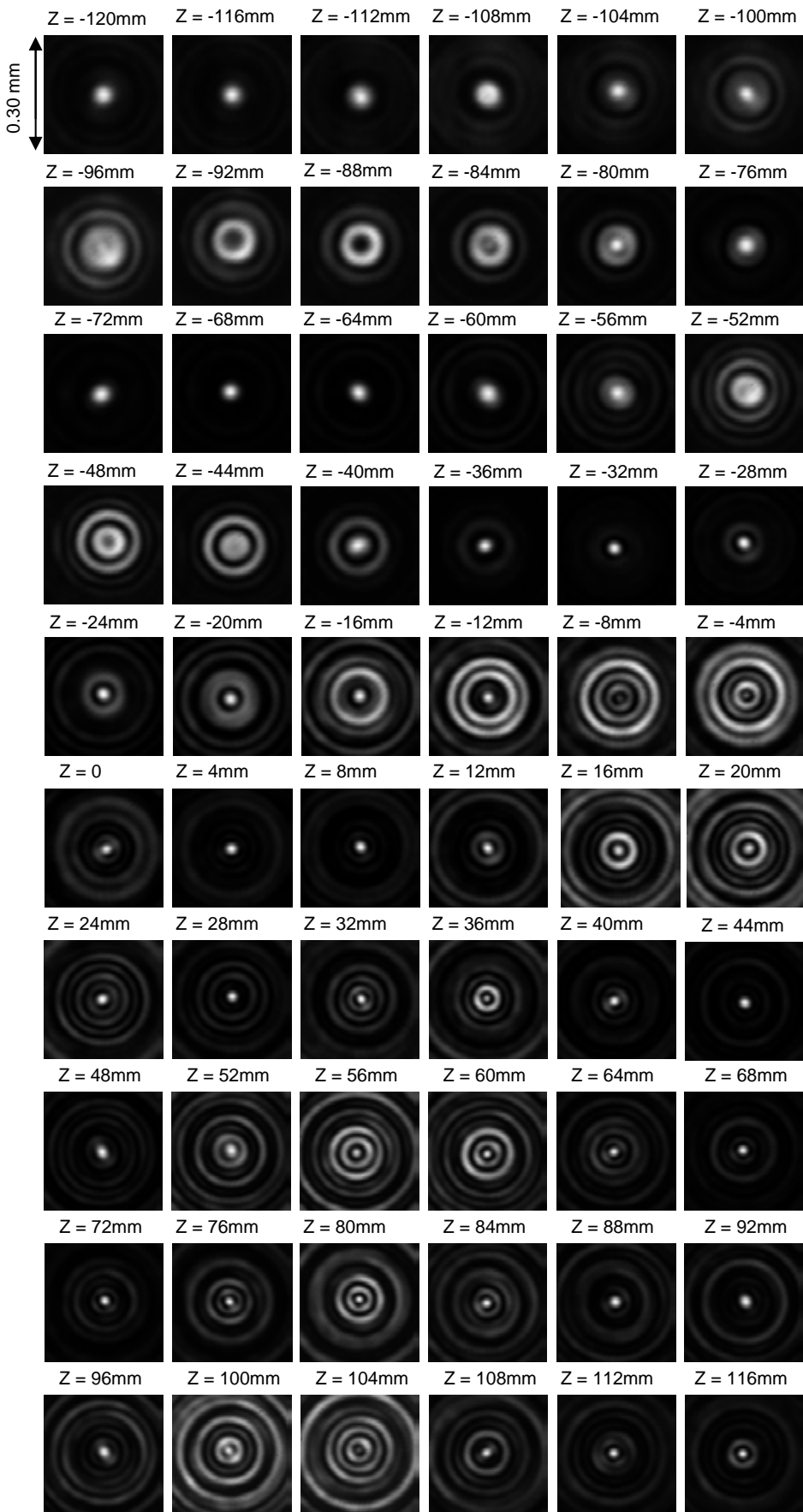


Figura 5.21. PSF experimentales obtenidas con la lente M9anil. Las focales más cortas están en el interior de la lente.

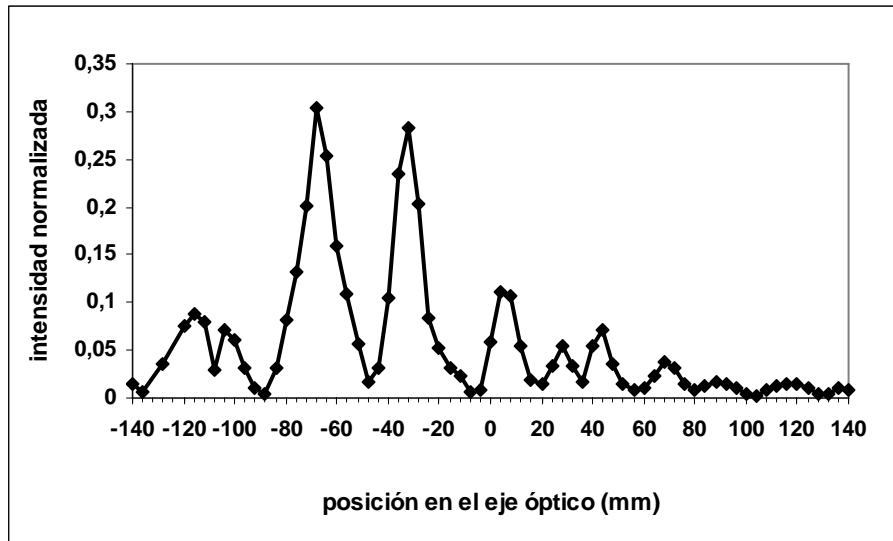


Figura 5.22. Perfil de intensidad a lo largo del eje óptico para la lente multiplexada M9ani1 con las focales cortas en el interior de la lente. La intensidad está normalizada al valor máximo con la lente SL. El origen en el eje óptico corresponde al plano focal imagen para la lente SL.

En la Figura 5.21 se muestran los resultados experimentales de las PSF capturadas a diferentes distancias de la lente para la misma multiplexada M9ani1, pero con las lentes distribuidas de manera que la focal central corresponde a 920 mm (la más corta) y el resto ocupan progresivamente los anillos desde el interior hacia el exterior. Se puede apreciar como, al contrario que en el caso anterior, para  $Z<0$  el máximo central de cada PSF resulta más amplio y los anillos más difusos que para  $Z>0$ .

La Figura 5.22 muestra el perfil de intensidad a lo largo del eje óptico medido a partir de la intensidad central de las imágenes de la Figura 5.21. Al igual que en el caso anterior, aparecen oscilaciones en la intensidad correspondientes a las diferentes focales de las lentes que componen la multiplexada, pero en este caso los valores más elevados de intensidad corresponden a los máximos situados en  $Z<0$ . El FWHM para cada uno de esos máximos también es del orden del FWHM para la SL (ver Figura 5.12). De nuevo aparecen menos máximos que los que serían de esperar por el número de lentes que componen esta multiplexada a causa, probablemente, de la interferencia destructiva producida entre los diferentes haces.

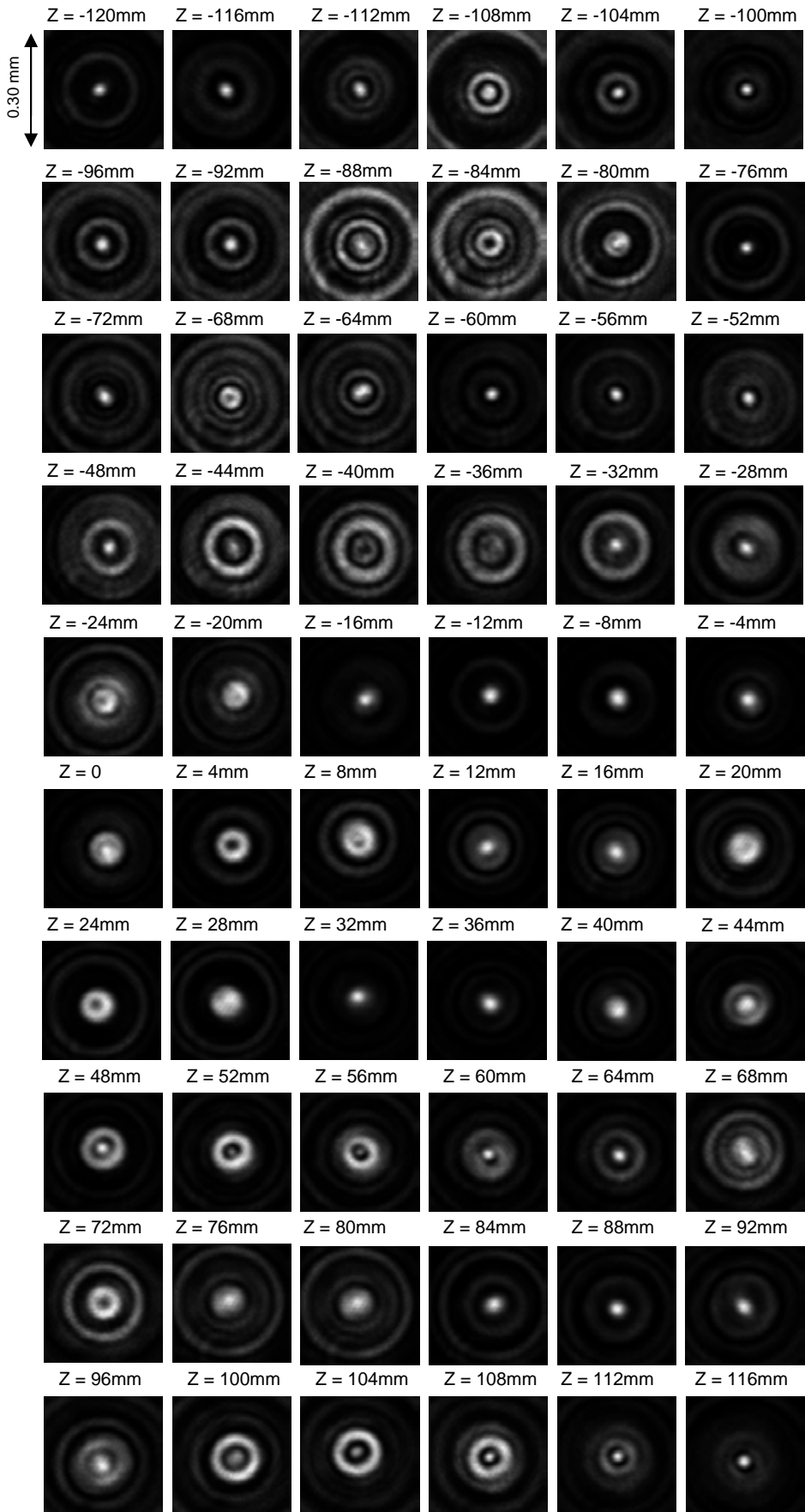


Figura 5.23. PSF experimentales obtenidas con la lente M9ani3. Las focales más largas están hacia el interior de la lente.

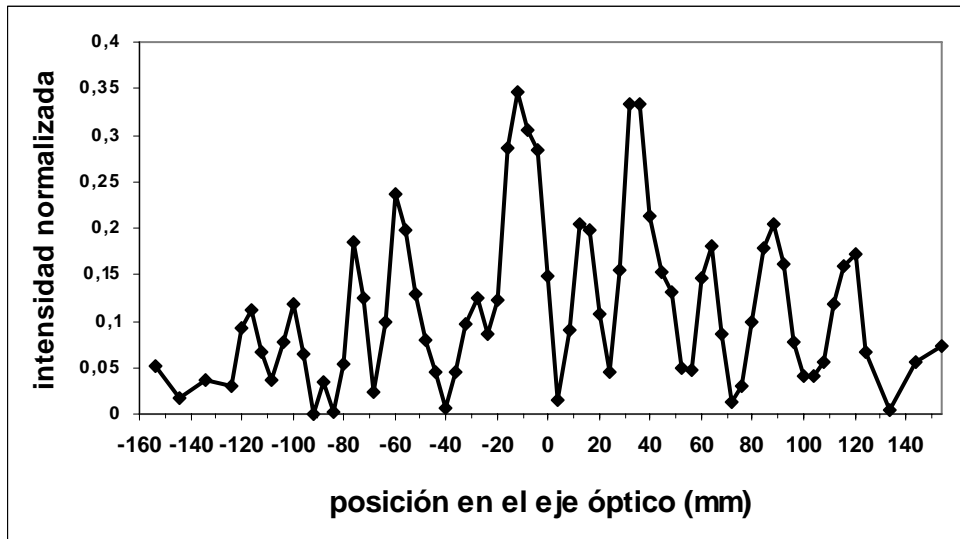


Figura 5.24. Perfil de intensidad a lo largo del eje óptico para la lente multiplexada M9ani3 con las focales largas hacia el interior de la lente. La intensidad está normalizada al valor máximo con la lente SL. El origen en el eje óptico corresponde al plano focal imagen para la lente SL.

En la Figura 5.23 se muestran los resultados experimentales de las PSF a diferentes distancias para la multiplexada M9ani3, construida a partir de 9 lentes de focales entre 920 y 1080 mm, con 3 anillos para cada focal. En este caso las lentes están distribuidas de manera que la focal central corresponde a 1080 mm y el resto ocupan progresivamente los anillos desde el interior hacia el exterior. Como a cada focal le corresponden 3 anillos el proceso se repite de manera que los anillos número 10 y número 30 vuelven a corresponder a la focal más larga.

La Figura 5.24 muestra el perfil de intensidad a lo largo del eje óptico medido a partir de la intensidad central de las imágenes de la Figura 5.23. Esta manera de distribuir los anillos hace desaparecer la asimetría que se presentaba tan evidente para el caso de un solo anillo por lente. En la Figura 5.23 y en la Figura 5.24 se puede observar que las asimetrías respecto a  $Z=0$  prácticamente desaparecen. En el perfil de intensidad se observan oscilaciones correspondientes a las diferentes focales que componen la multiplexada, con el FWHM de cada uno de los máximos similar al de la SL (Figura 5.12). En este caso la correspondencia entre el número de máximos y el de focales es mayor que en los casos anteriores, ya que los haces que convergen en cada focal proceden de 3 zonas diferentes de la lente y es más difícil que se den las condiciones de interferencia destructiva.

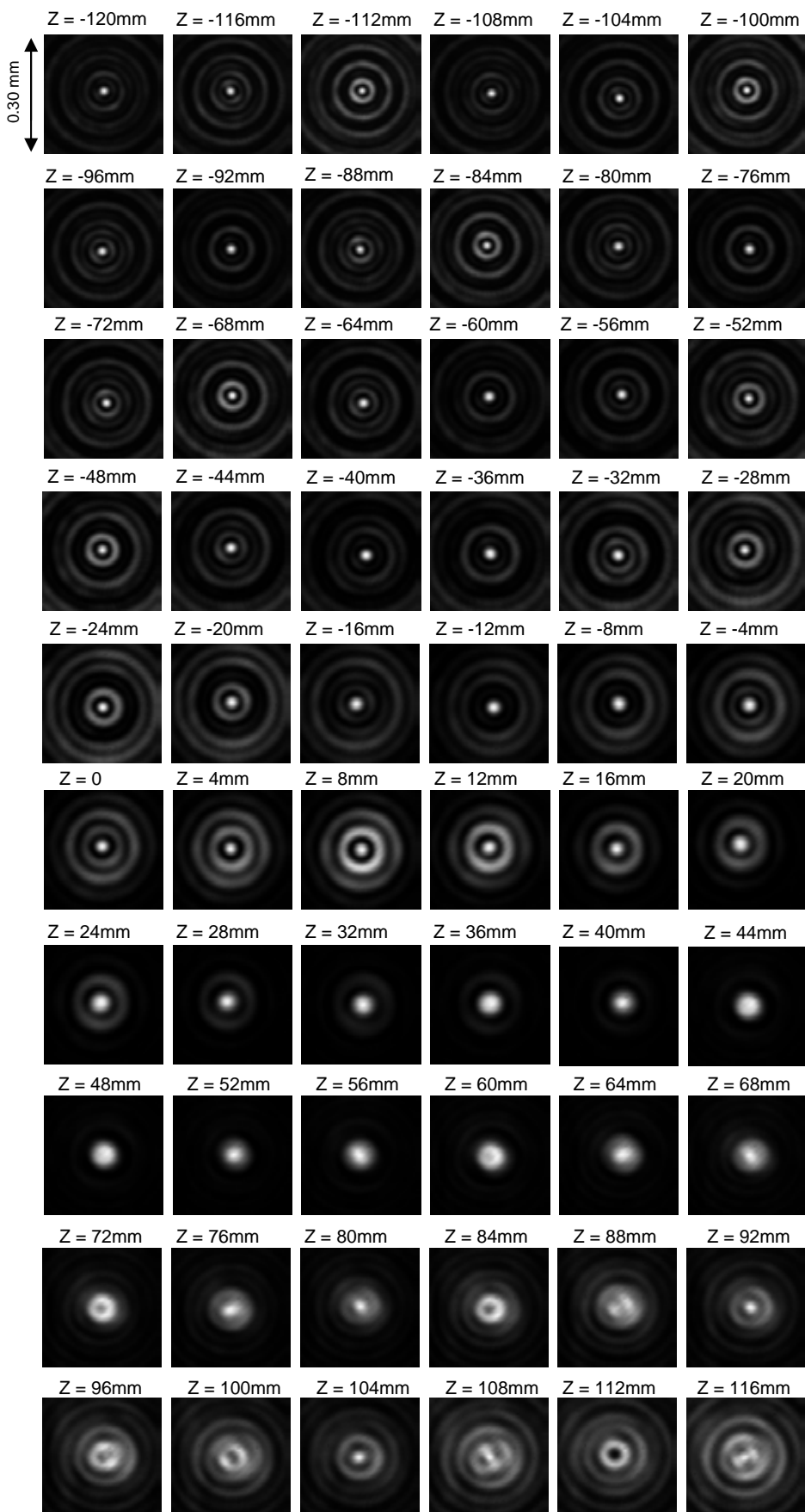


Figura 5.25. PSF experimentales obtenidas con la lente M33ani1. Las focales más largas están en el interior de la lente.

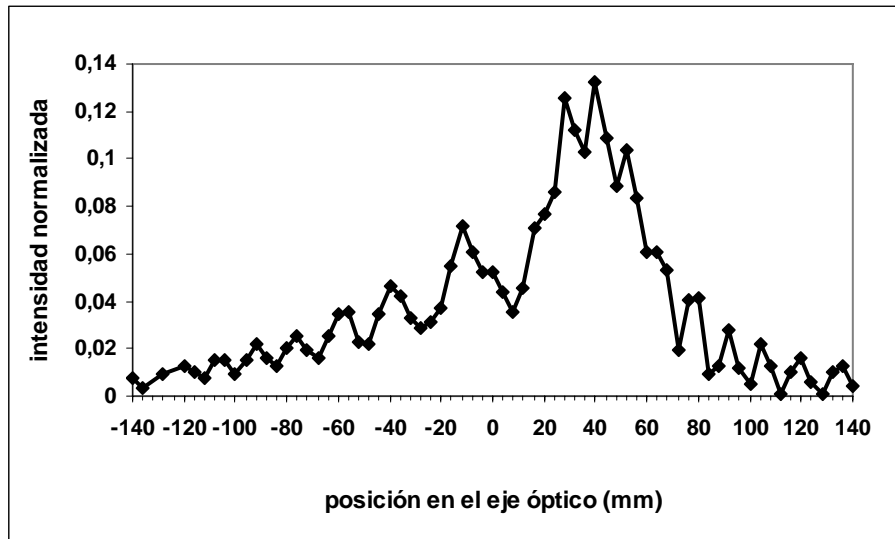


Figura 5.26. Perfil de intensidad a lo largo del eje óptico para la lente multiplexada M33ani1 con las focales largas en el interior de la lente. La intensidad está normalizada al valor máximo con la lente SL. El origen en el eje óptico corresponde al plano focal imagen para la lente SL.

En la Figura 5.25 se muestran los resultados experimentales de las PSF capturadas a diferentes distancias de la lente para la multiplexada M33ani1, es decir, construida a partir de 33 lentes de focales entre 920 y 1080 mm, mediante el sistema de multiplexado por anillos. En este caso las lentes están distribuidas de manera que la focal central corresponde a 1080 mm y el resto ocupan progresivamente los anillos desde el interior hacia el exterior. Al igual que en el caso de la lente M9ani1, se puede apreciar como el máximo central de cada PSF resulta más amplio y los anillos más difusos para valores de  $Z>0$ .

La Figura 5.26 muestra el perfil de intensidad a lo largo del eje óptico medido a partir de la intensidad central de las imágenes de la Figura 5.25. Aparecen oscilaciones en la intensidad correspondientes a las diferentes focales de las lentes que componen la multiplexada, con los valores más elevados de intensidad para los máximos situados en  $Z>0$ . Sin embargo, en este caso el número de focales multiplexadas en la lente es mayor que en el caso anterior (33 focales en lugar de 9). Esto produce un solapamiento de los máximos que produce un máximo más amplio centrado aproximadamente en  $z = 40\text{mm}$  y con un FWHM de unos 40 mm. Observando la Figura 5.25 vemos además que en esa zona, entre  $Z = 28\text{ mm}$  y  $Z = 68\text{ mm}$ , el máximo central de las PSF es uniforme y mucho más intenso que los anillos, por lo que puede ser una buena región para formar imágenes extensas y con mayor profundidad de foco que con la SL.

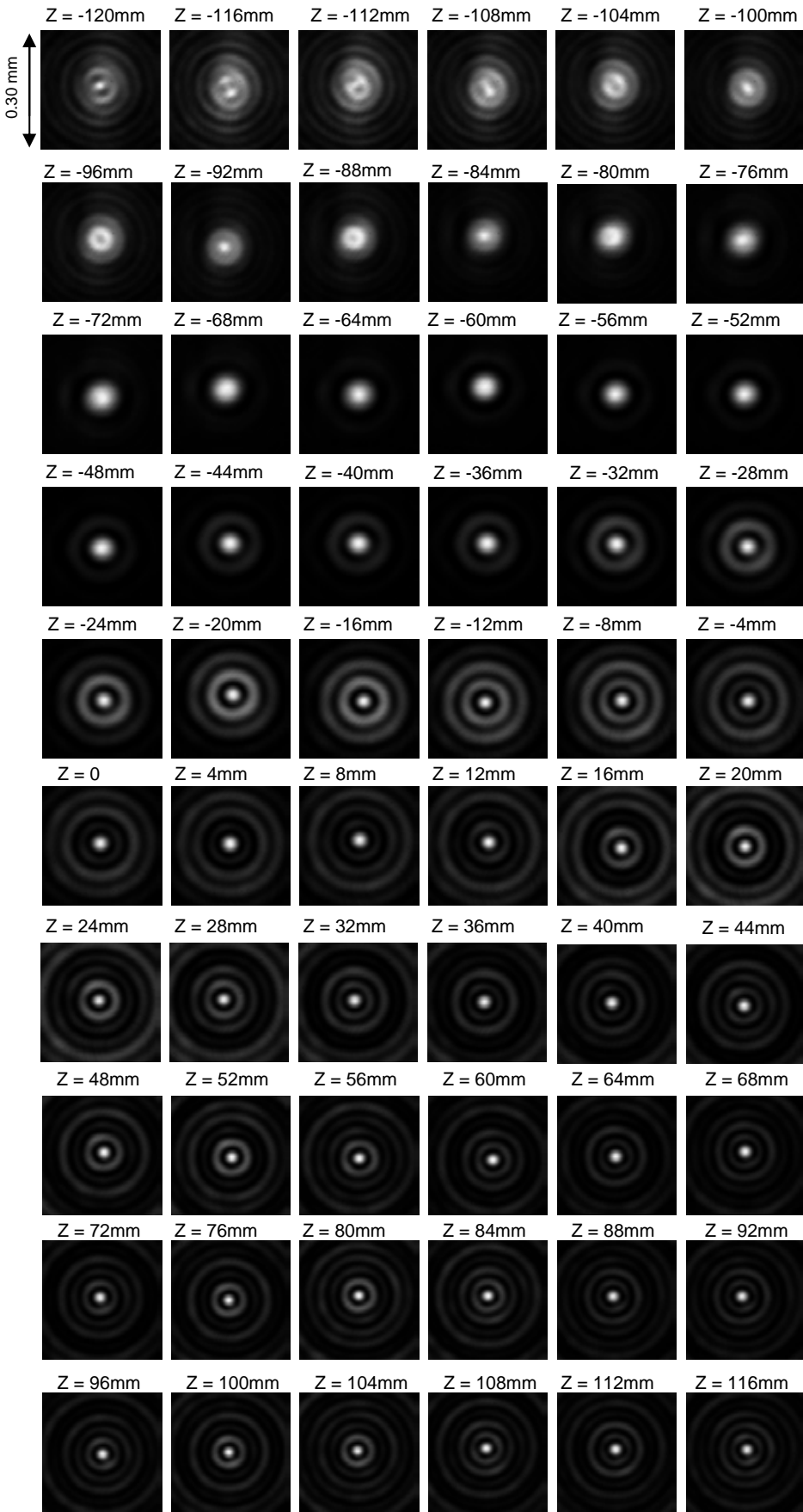


Figura 5.27. PSF experimentales obtenidas con la lente M33ani1. Las focales más cortas están en el interior de la lente.

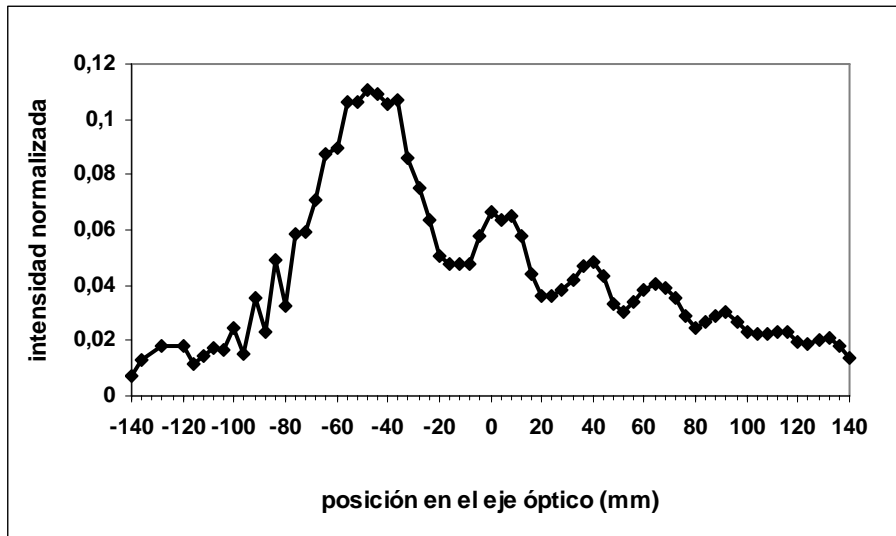


Figura 5.28. Perfil de intensidad a lo largo del eje óptico para la lente multiplexada M33ani1 con las focales cortas en el interior de la lente. La intensidad está normalizada al valor máximo con la lente SL. El origen en el eje óptico corresponde al plano focal imagen para la lente SL.

La Figura 5.27 corresponde a los resultados experimentales de las PSF capturadas a diferentes distancias de la lente para la multiplexada M33ani1. En este caso las lentes están distribuidas de manera que la focal central corresponde a la más corta, 920 mm, y el resto ocupan progresivamente los anillos desde el interior hacia el exterior. El máximo central de cada PSF resulta más amplio y los anillos son más difusos para valores de  $Z < 0$ .

La Figura 5.28 muestra el perfil de intensidad a lo largo del eje óptico medido a partir de la intensidad central de las imágenes de la Figura 5.27. De nuevo aparecen oscilaciones en la intensidad correspondientes a las diferentes focales de las lentes que componen la multiplexada, pero en este caso con los valores más elevados de intensidad para los máximos situados en  $Z < 0$ . El máximo más amplio debido al solapamiento de los diferentes máximos está centrado aproximadamente en  $Z = -50$  mm y con un FWHM de unos 45 mm. Observando la Figura 5.27 vemos además que en la zona entre  $Z = -80$  mm y  $Z = -52$  mm, el máximo central de las PSF es uniforme y mucho más intenso que los anillos, por lo que puede ser una buena región para formar imágenes extensas y con mayor profundidad de foco que con la SL.

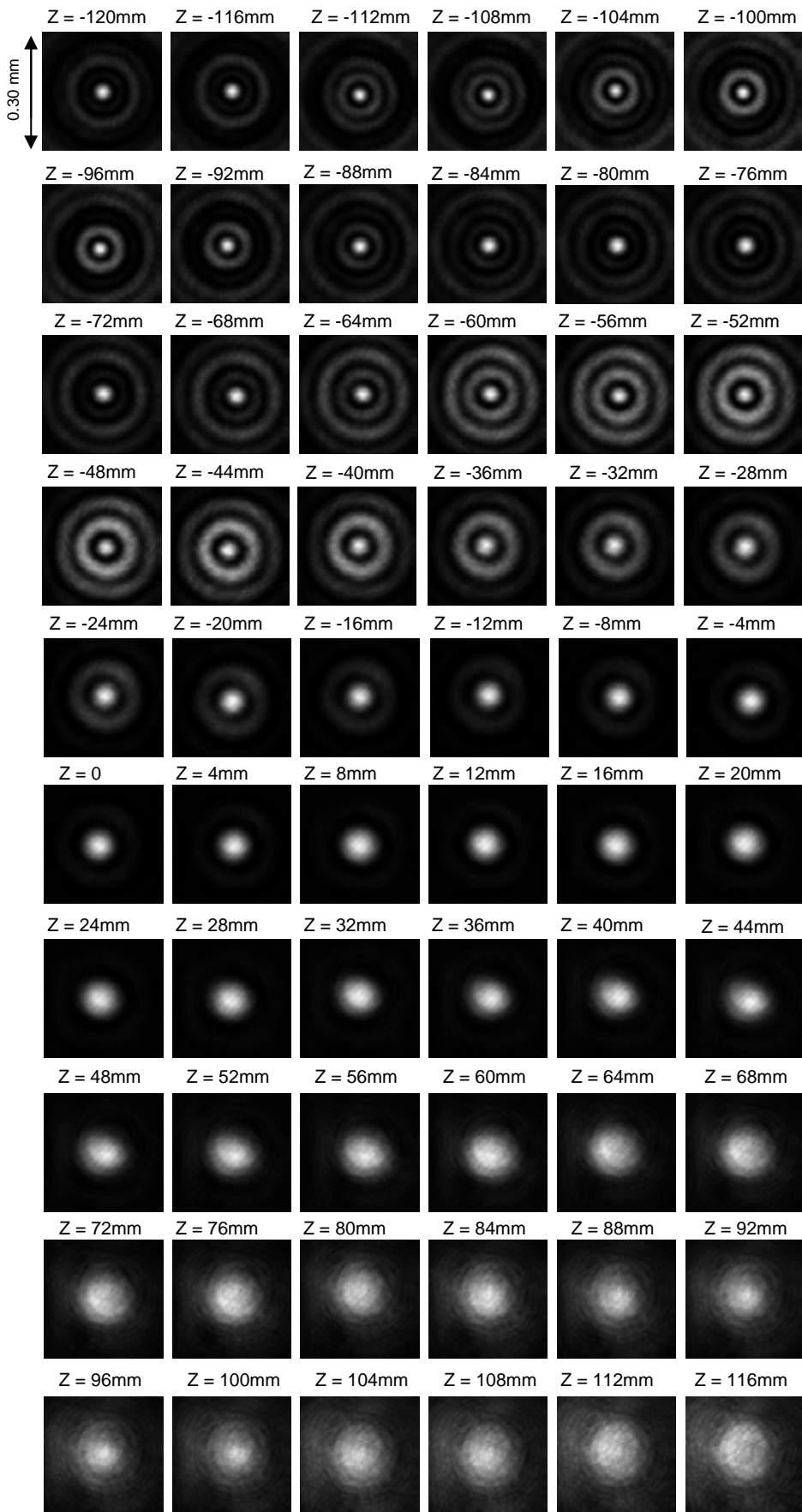


Figura 5.29. PSF experimentales obtenidas con la lente M33ani3. Las focales más largas están hacia el interior de la lente.

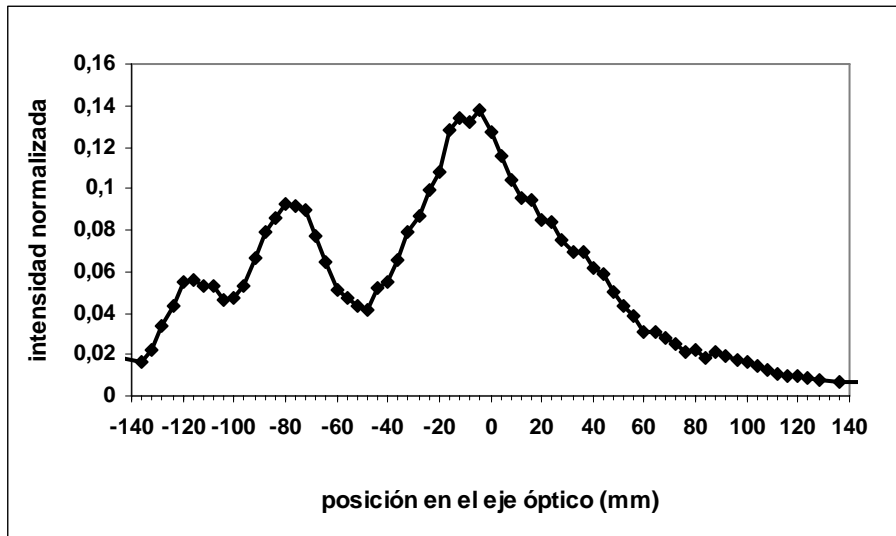


Figura 5.30. Perfil de intensidad a lo largo del eje óptico para la lente multiplexada M33ani3 con las focales largas hacia el interior de la lente. La intensidad está normalizada al valor máximo con la lente SL. El origen en el eje óptico corresponde al plano focal imagen para la lente SL.

En la Figura 5.29 se muestran los resultados experimentales de las PSF capturadas a diferentes distancias de la lente para la multiplexada M33ani3, es decir, construida a partir de 33 lentes de focales entre 920 y 1080 mm, mediante el sistema de multiplexado por anillos. En este caso las lentes están distribuidas de manera que la focal central corresponde a 1080 mm y el resto ocupan progresivamente los anillos desde el interior hacia el exterior. Como a cada focal le corresponden 3 anillos el proceso se repite de manera que los anillos número 34 y número 68 vuelven a corresponder a la focal más larga. A diferencia de lo que sucedía para la lente M9ani3, en este caso sí hay asimetría respecto a  $Z = 0$  y el máximo central de cada PSF resulta más amplio y los anillos más difusos para valores de  $Z > 0$ .

Sin embargo, la Figura 5.30 muestra cómo las intensidades más elevadas del perfil de intensidad se dan para los valores de  $Z < 0$ . El máximo de intensidad más amplio está centrado en  $Z = 0$ , con un FWHM de unos 60 mm. Sin embargo en esa misma zona se aprecia en las PSF el paso de un efecto hiperresolvente transversal a un efecto apodizante conforme nos desplazamos de valores negativos a positivos, de modo que el FWHM se incrementa respecto a la lente SL pero con una respuesta transversal y en intensidad que no es uniforme en ese intervalo.

## **5.6 Resultados del multiplexado aleatorio**

Para el multiplexado aleatorio hemos escogido subaperturas de  $1 \times 1$  píxeles y de  $8 \times 8$  píxeles para construir lentes multiplexadas que cubren un rango de distancias focales entre 920 mm y 1080 mm.

La Figura 5.31 muestra las lentes que se han estudiado: M9rand1 es el resultado de multiplexar 9 lentes, con un intervalo entre distancias focales consecutivas de 2 cm; M17rand1 es el resultado de multiplexar 17 lentes, con 1 cm entre focales consecutivas; M33rand1 es fruto de multiplexar 33 lentes, con un espaciado de 0,5 cm entre focales consecutivas, todas ellas con subaperturas de  $1 \times 1$  píxeles.

Se han construido también las lentes multiplexadas aleatorias con subaperturas de  $8 \times 8$  píxeles para 9 lentes (M9rand8) y para 33 lentes (M33rand8).

Los resultados experimentales correspondientes a las lentes multiplexadas por el método de asignación aleatoria se muestran en las figuras que van desde la Figura 5.32 a la Figura 5.41. Se presentan las PSF obtenidas en diferentes planos transversales al eje óptico, así como los perfiles de intensidad a lo largo del eje para cada caso. Los valores de las curvas de intensidad están normalizados respecto al valor del máximo de intensidad para la lente SL.

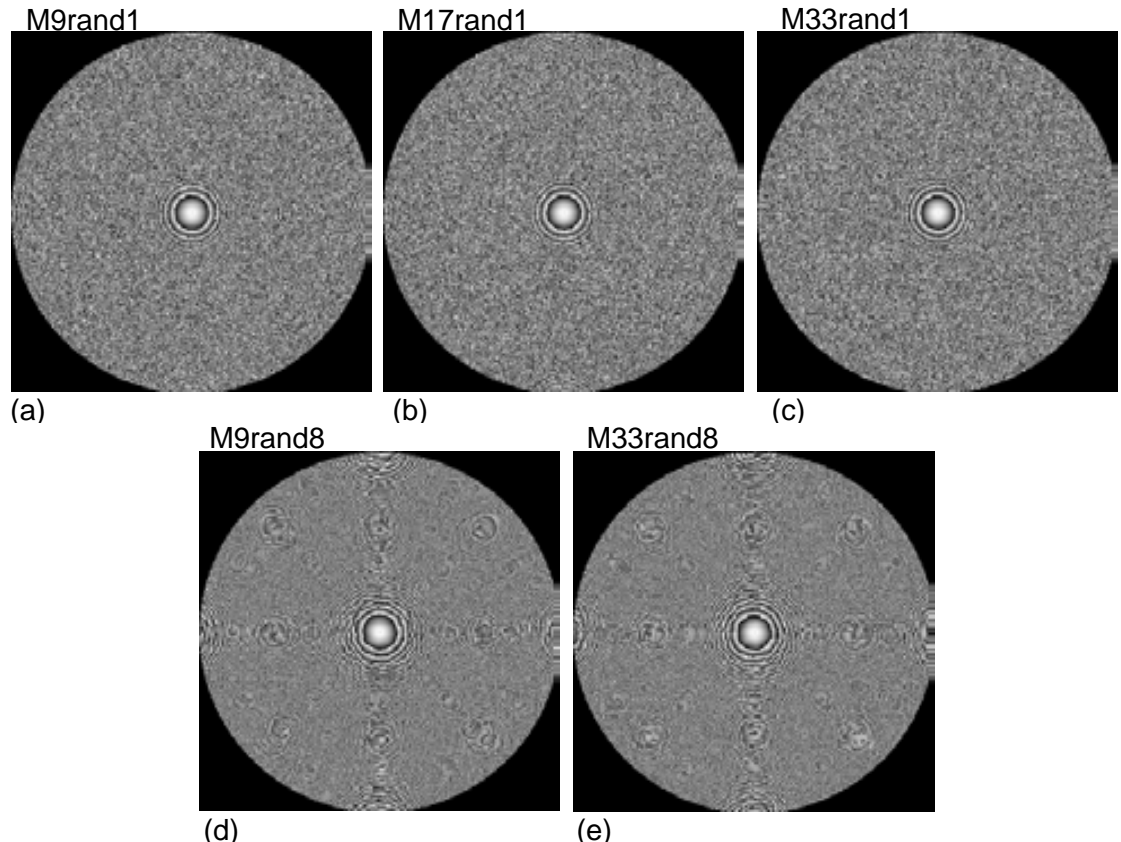


Figura 5.31. Lentes multiplexadas por el método aleatorio: (a), (b) y (c) corresponden a multiplexadas de 9, 17 y 33 lentes respectivamente, con subaperturas de  $1 \times 1$  píxeles; (d) y (e) corresponden a multiplexadas de 9 y 33 lentes respectivamente, con subaperturas de  $8 \times 8$  píxeles.

El multiplexado aleatorio elimina las asimetrías producidas por las técnicas de multiplexado anteriores, por anillos o por sectores, en la distribución de las diferentes focales en la lente multiplexada. Esto implica una respuesta a lo largo del eje más simétrica respecto de  $Z = 0$  que en los casos anteriores.

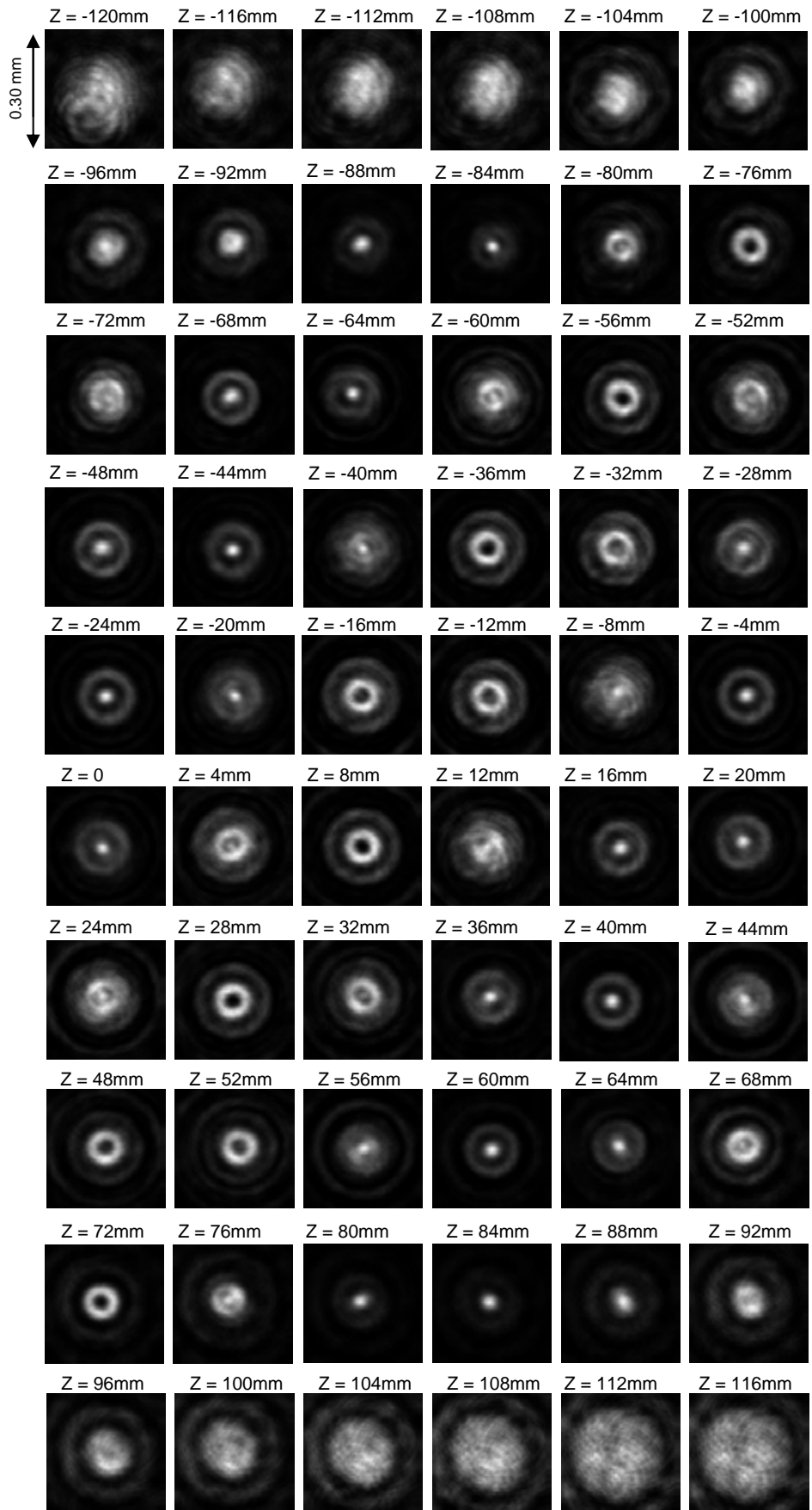


Figura 5.32. PSF experimentales obtenidas con la lente M9rand1.

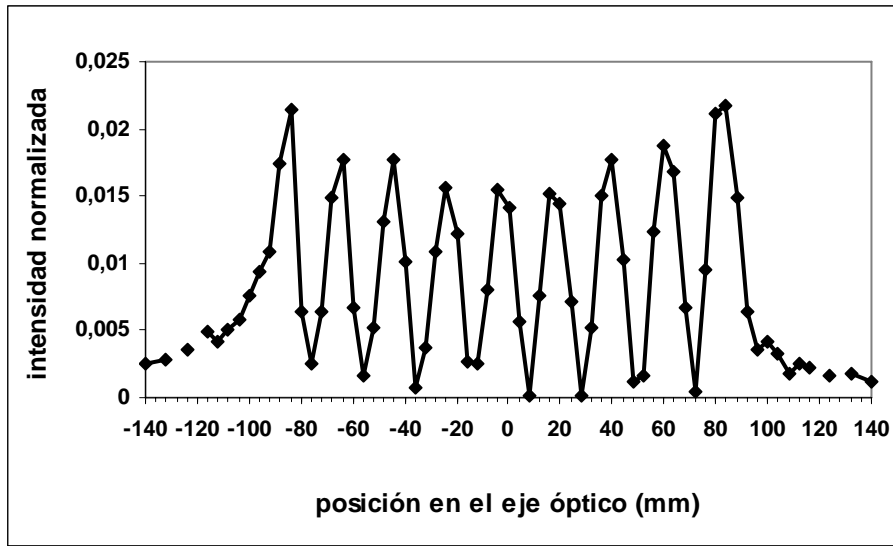


Figura 5.33. Perfil de intensidad a lo largo del eje óptico para la lente multiplexada M9rand1. La intensidad está normalizada al valor máximo con la lente SL. El origen en el eje óptico corresponde al plano focal imagen para la lente SL.

En la Figura 5.32 se muestran los resultados experimentales de las PSF capturadas a diferentes distancias de la lente para la multiplexada M9rand1, es decir, construida a partir de 9 lentes de focales entre 920 mm y 1080 mm, mediante el sistema de multiplexado aleatorio. En este caso las subaperturas son de un solo píxel. En casi todo el rango de distancias estudiado aparecen estructuras anulares. En el centro de cada PSF se van alternando máximos y mínimos a medida que nos desplazamos a lo largo del eje óptico. Estas oscilaciones de intensidad se aprecian claramente en la curva de intensidad a lo largo del eje que se muestra en la Figura 5.33. Aparece un máximo por cada una de las 9 focales que componen la lente multiplexada.

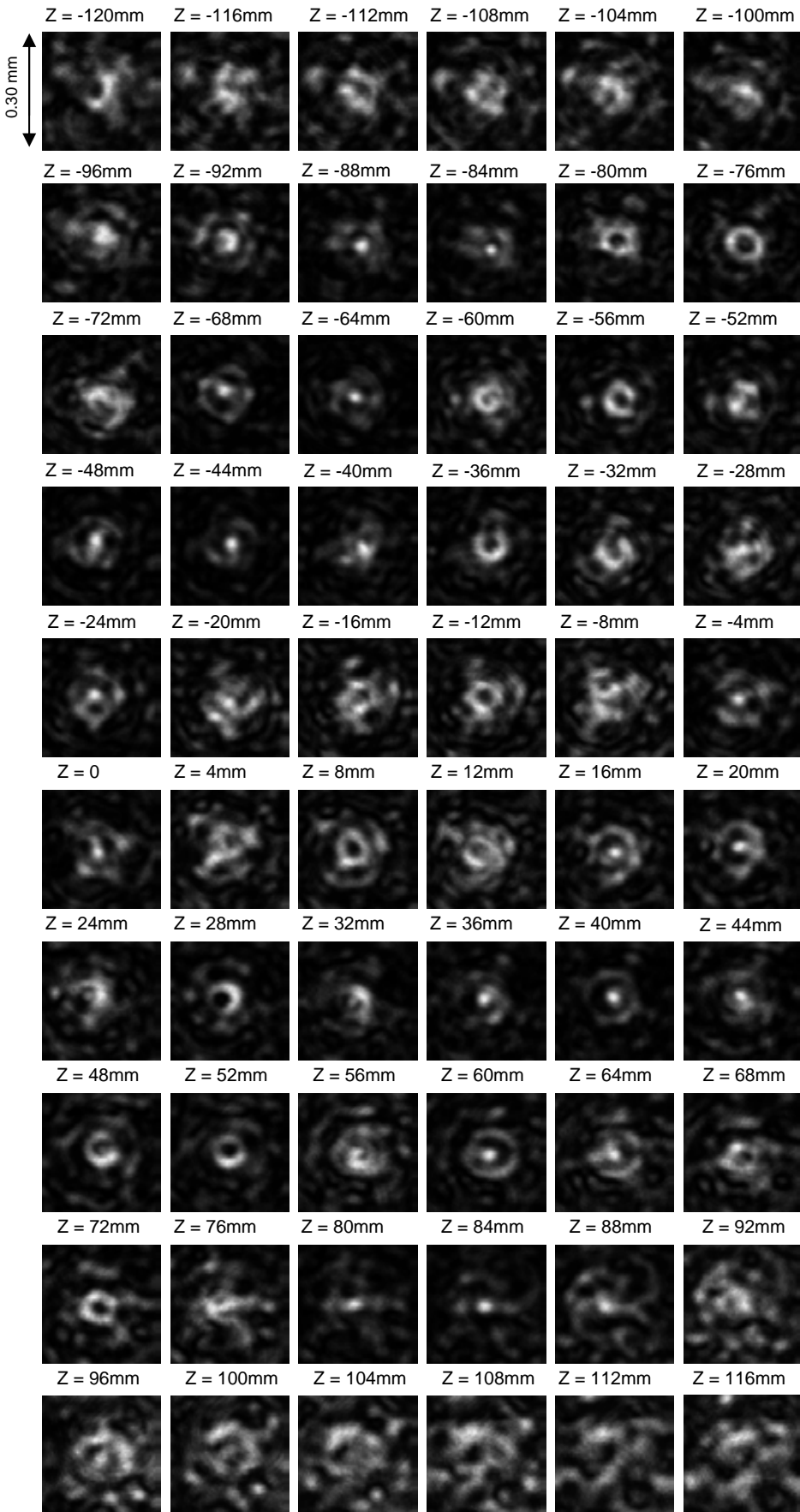


Figura 5.34. PSF experimentales obtenidas con la lente M9rand8.

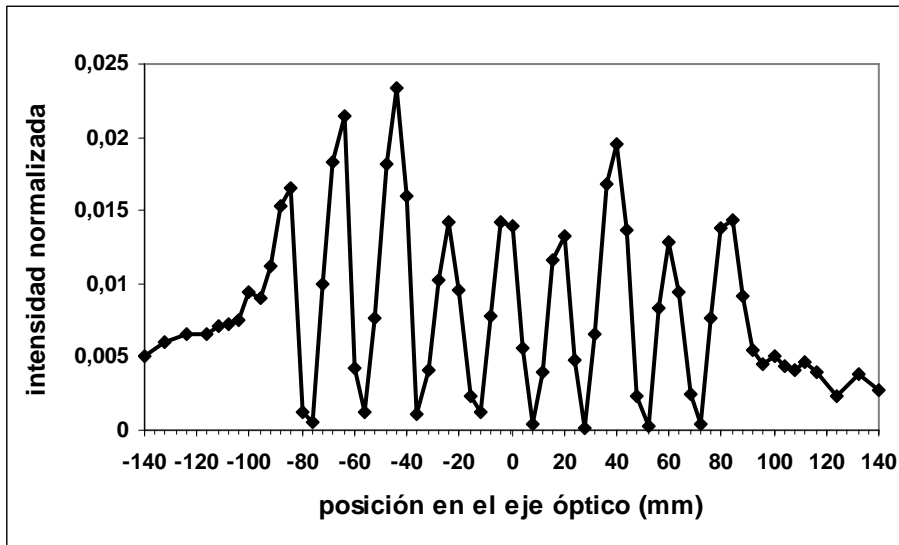


Figura 5.35. Perfil de intensidad a lo largo del eje óptico para la lente multiplexada M9rand8. La intensidad está normalizada al valor máximo con la lente SL. El origen en el eje óptico corresponde al plano focal imagen para la lente SL.

Al incrementar el tamaño de las subaperturas de la distribución aleatoria a  $8 \times 8$  píxeles los resultados empeoran. La Figura 5.34 muestra los resultados experimentales de las PSF capturadas a diferentes distancias de la lente para la multiplexada M9rand8, construida de la misma manera que la lente multiplexada anterior, a partir de 9 lentes de focales distintas, pero con subaperturas de  $8 \times 8$  píxeles.

En este caso las estructuras transversales de las PSF a diferentes distancias a lo largo del eje muestran distribuciones de intensidad irregulares en el plano. La Figura 5.35 muestra la curva de intensidad a lo largo del eje, obtenida a partir de los valores centrales de las imágenes mostradas en la Figura 5.34. Se puede apreciar de nuevo la presencia de 9 máximos de intensidad separados a intervalos regulares, y que corresponden a las 9 focales de la lente multiplexada.

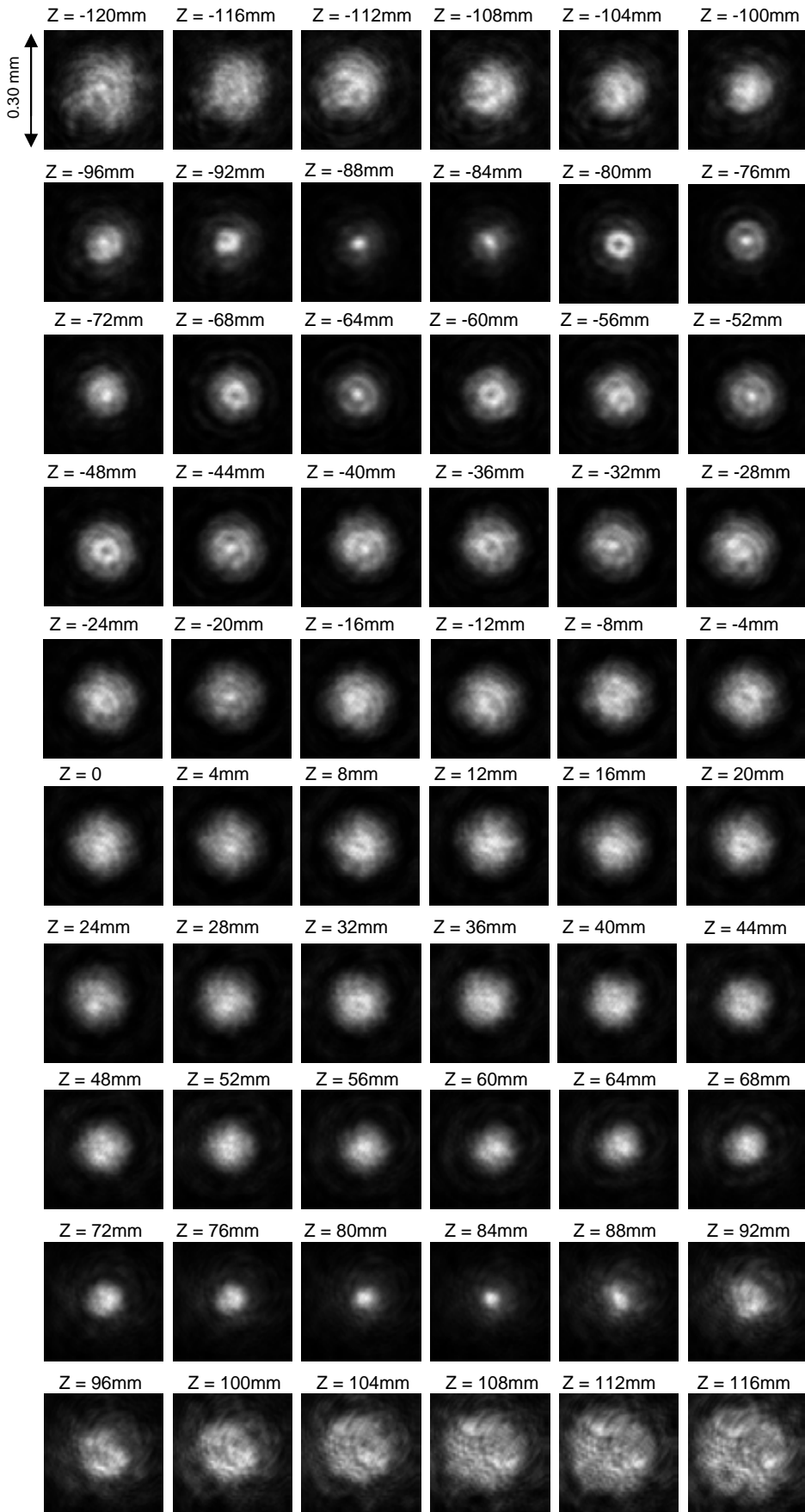


Figura 5.36. PSF experimentales obtenidas con la lente M17rand1.

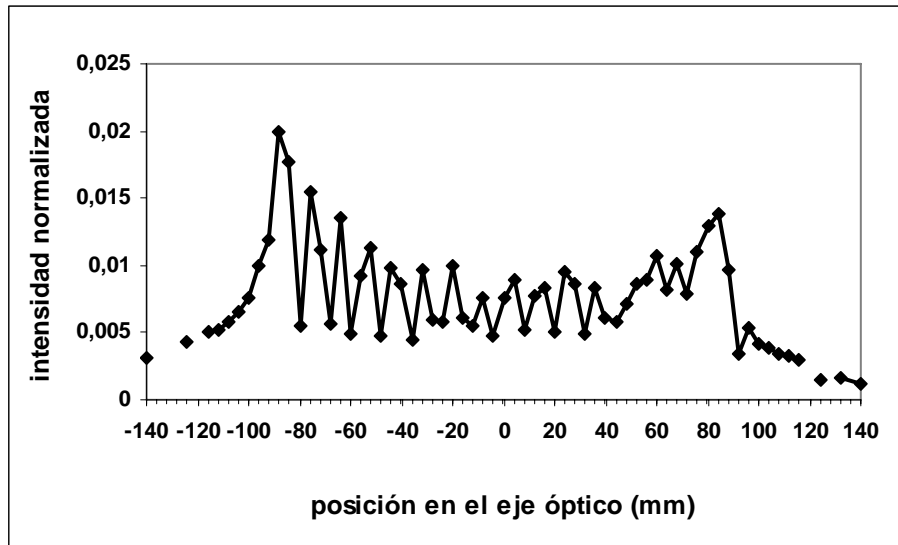


Figura 5.37. Perfil de intensidad a lo largo del eje óptico para la lente multiplexada M17rand1. La intensidad está normalizada al valor máximo con la lente SL. El origen en el eje óptico corresponde al plano focal imagen para la lente SL.

La Figura 5.36 muestra los resultados experimentales de las PSF capturadas a diferentes distancias de la lente para la multiplexada M17rand1, construida a partir de 17 lentes de focales entre 920 mm y 1080 mm, con subaperturas de  $1 \times 1$  píxeles. En esta nueva lente multiplexada hay una nueva focal entre cada dos focales de la multiplexada anterior, compuesta por 9 lentes. En este caso la distribución transversal de la intensidad en los diferentes planos es muy uniforme en un rango de distancias que va desde aproximadamente  $z = -56$  mm hasta  $z = 56$  mm, aunque el máximo central es más ancho que en los casos anteriores.

El perfil de intensidad a lo largo del eje, mostrado en la Figura 5.37, muestra una serie de oscilaciones que corresponden a las focales de las 17 lentes que componen la multiplexada. El solapamiento de los máximos hace que las oscilaciones de intensidad sean menos pronunciadas que en el caso de 9 lentes.

Aunque el resultado es bastante satisfactorio, si se desea obtener una respuesta de intensidad a lo largo del eje más plana es necesario investigar la inserción de un número mayor de lentes en la lente multiplexada.

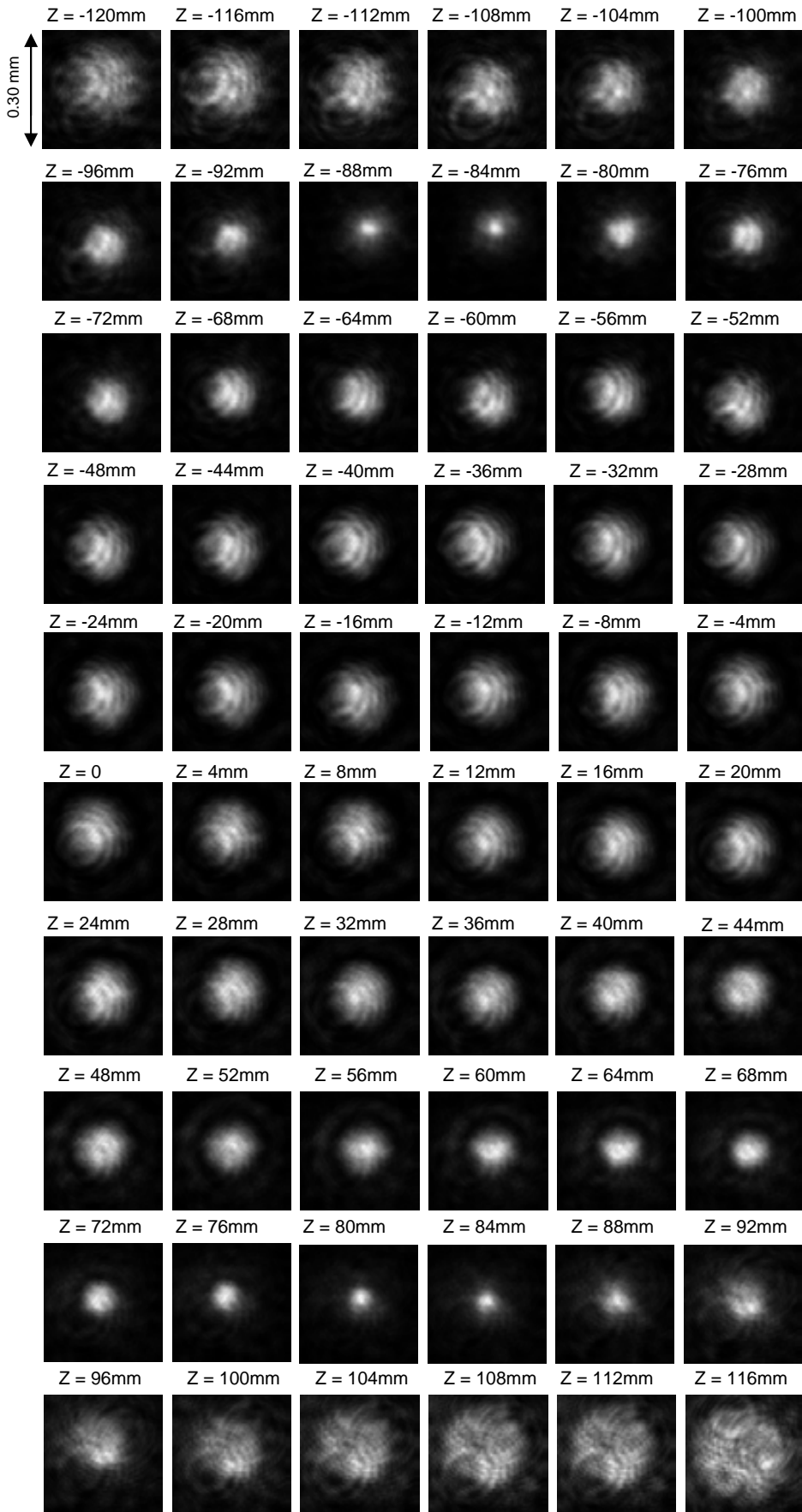


Figura 5.38. PSF experimentales obtenidas con la lente M33rand1.

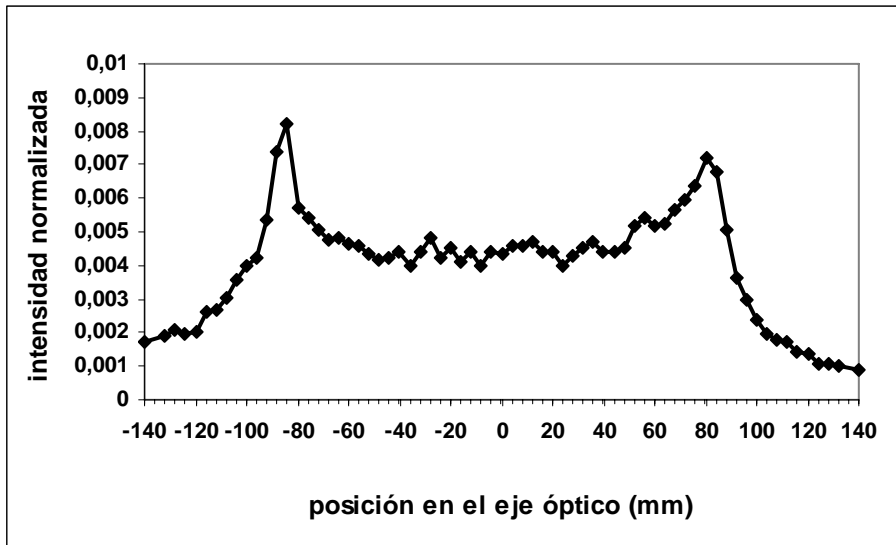


Figura 5.39. Perfil de intensidad a lo largo del eje óptico para la lente multiplexada M33rand1. La intensidad está normalizada al valor máximo con la lente SL. El origen en el eje óptico corresponde al plano focal imagen para la lente SL.

En la Figura 5.38 se muestran los resultados experimentales de las PSF capturadas a diferentes distancias de la lente para la multiplexada M33rand1, construida a partir de 33 lentes de focales entre 920 mm y 1080 mm, con subaperturas de 1×1 píxeles. Se trata de la lente multiplexada con mayor número de focales intermedias que hemos estudiado. El resultado muestra distribuciones muy uniformes para la PSF en los planos desenfocados conforme nos desplazamos a lo largo del eje. Podemos considerar toda una zona, con los límites alrededor de  $z = -56$  mm y  $z = 56$  mm, en la que el máximo central de la PSF tiene un radio uniforme sin anillos laterales, aunque mayor que el máximo central de la PSF para la SL. Aunque este incremento en el diámetro del máximo transversal de la PSF disminuye el poder resolutivo del sistema óptico, la respuesta de la intensidad a lo largo del eje es, pese a los dos picos que aparecen al principio y al final ( $z \approx \pm 80$  mm), mucho más plana que en todos los casos anteriores a lo largo de una gran distancia (Figura 5.39). Concretamente, el FWHM de este perfil corresponde a un valor de aproximadamente 200 mm.

Podemos considerar que el multiplexado aleatorio con 33 lentes con focales entre 920mm y 1080mm representa una técnica satisfactoria para incrementar la profundidad de foco de nuestro sistema óptico. El principal inconveniente es que la intensidad es muy baja en comparación con la SL. Además, como se verá, para imágenes extensas será necesario utilizar una cámara con gran rango dinámico.

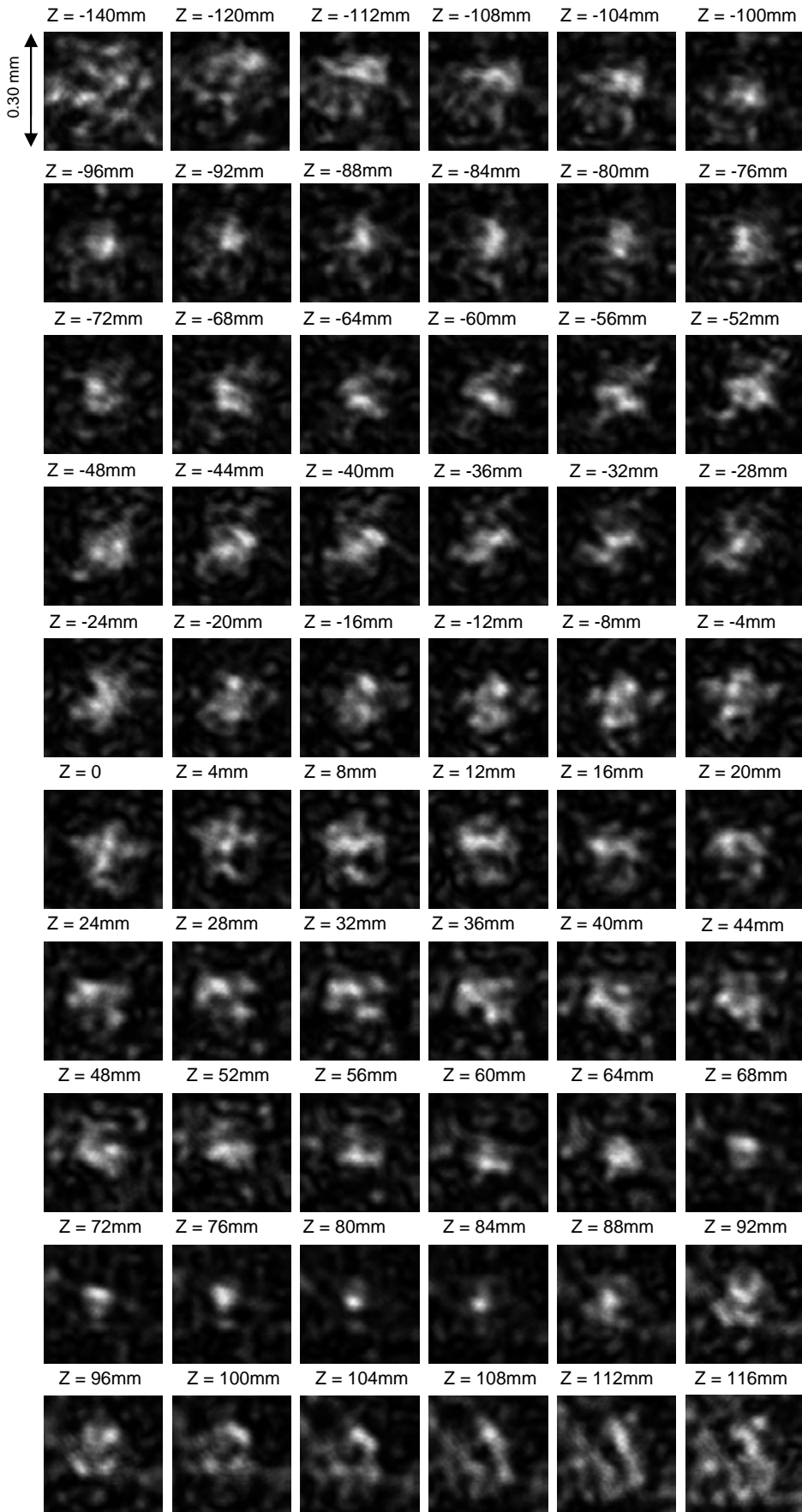


Figura 5.40. PSF experimentales obtenidas con la lente M33rand8.

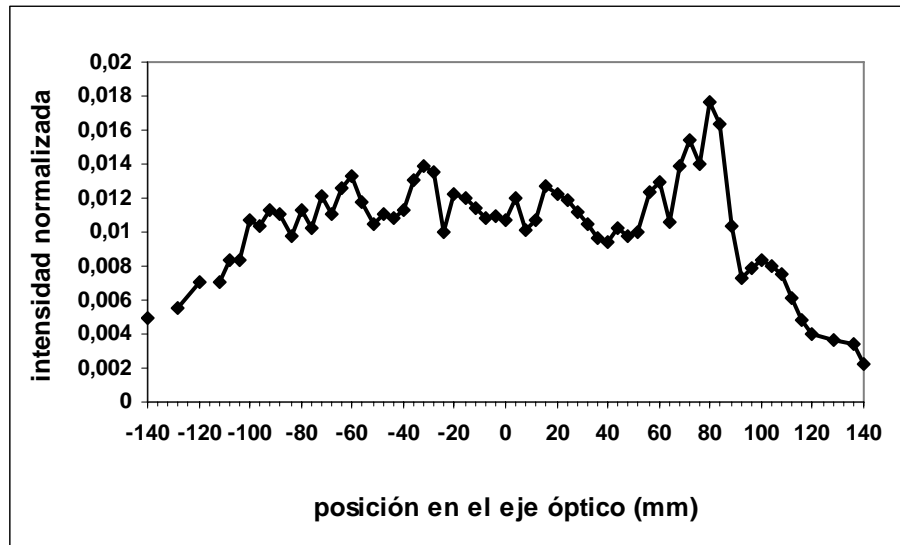


Figura 5.41. Perfil de intensidad a lo largo del eje óptico para la lente multiplexada M33rand8. La intensidad está normalizada al valor máximo con la lente SL. El origen en el eje óptico corresponde al plano focal imagen para la lente SL.

En la Figura 5.40 se muestran los resultados experimentales de las PSF capturadas a diferentes distancias de la lente para la multiplexada M33rand8, construida a partir de 33 lentes de focales entre 920 mm y 1080 mm, pero en este caso con subaperturas de  $8 \times 8$  píxeles. Tal como vimos con la lente M9rand8, el hecho de incrementar el tamaño de las subaperturas empeora la respuesta transversal de las PSF a distancias desenfocadas, presentando estructuras irregulares. El perfil de intensidad en este caso (Figura 5.41) es menos uniforme respecto al obtenido para 33 lentes y subaperturas de 1 píxel.

En el próximo apartado se estudiará la respuesta de la técnica de multiplexado aleatorio con objetos extensos.

## 5.7 Resultados para objetos extensos

### 5.7.1 Cálculo de la MTF

Con el fin de estudiar el efecto de las lentes multiplexadas en la formación de imágenes con objetos extensos en los planos desenfocados, se ha evaluado en primer lugar la MTF (*Modulation Transfer Function*) para la lente sencilla SL, y para las lentes multiplexadas M9rand1 y M33rand1. Como se vio en el apartado 3.5, la MTF proporciona la modulación del sistema para cada frecuencia espacial de la distribución de intensidad del objeto, generalmente con valores menores que 1, excepto para la frecuencia cero.

La MTF se ha calculado en tres planos: el plano de mejor imagen ( $Z=0$ ) y los planos desenfocados  $Z = -60$  mm y  $Z = -100$  mm (60 mm y 100 mm más cercanos al SLM que el plano  $Z=0$ ).

Para obtener la MTF teórica del sistema óptico se calcula la PSF a una distancia  $z'$  de la pupila, a partir de la propagación de la función pupila por difracción de Fresnel. Con el fin de evaluar las transformadas de Fourier por el algoritmo de FFT, se han ampliado las funciones pupila circulares con un diámetro de 480 puntos a matrices cuadradas de  $1024 \times 1024$  puntos, rellenando con valores 0. Si la función de pupila de fase  $f(x,y) = \exp[i\varphi(x,y)]$  es la matriz de la lente multiplexada, calculamos la PSF en  $z'$  (la función  $G(\xi,\eta)$ ) a partir de la expresión (3-27), es decir:

$$G(\xi,\eta)|_{z'} = PSF(\xi,\eta)|_{z'} = \left| \text{FFT} \left[ f(x,y) \exp \left[ i\pi / \lambda z' (x^2 + y^2) \right] \right] \right|^2 \quad (5-1)$$

Calculando la FFT de  $G(\xi,\eta)$  obtenemos la OTF (función de transferencia óptica), cuyo módulo, la función  $M(\mu,\nu)$ , es la MTF del sistema.

$$M(\mu,\nu) = |FT[G(\xi',\eta')]|. \quad (5-2)$$

En las siguientes figuras se muestra el resultado de la MTF para las pupilas consistentes en las lentes SL, M9rand1 y M33 rand1, a las distancias  $Z = 0$ ,  $Z = -60$  mm y  $Z = -100$  mm.

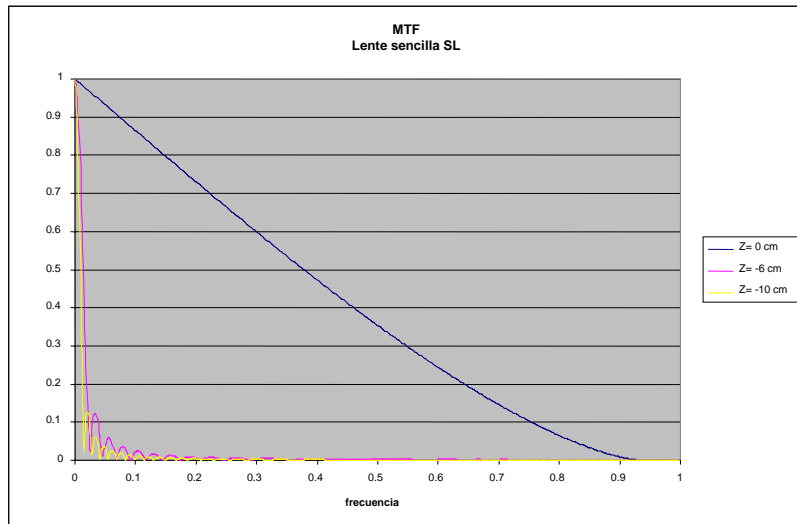


Figura 5.42. MTF de la lente sencilla SL en el plano de mejor imagen ( $Z=0$ ) y en dos planos desenfocados.

La Figura 5.42 muestra la MTF producida por la lente sencilla SL. Podemos observar una buena respuesta en el plano  $Z = 0$ , mientras que la respuesta se deteriora claramente para los planos desenfocados. Si nos centramos en las frecuencias más bajas de la gráfica para los planos desenfocados, la zona que se muestra ampliada en la Figura 5.43, vemos que existen numerosas inversiones de contraste. Cada vez que el valor de la MTF es 0 se produce una de estas inversiones de contraste, por lo que la información de la imagen correspondiente a esas frecuencias se pierde aunque se lleve a cabo un post-procesado de la imagen. Por ello, en estos planos desenfocados la calidad de la imagen obtenida es muy deficiente.

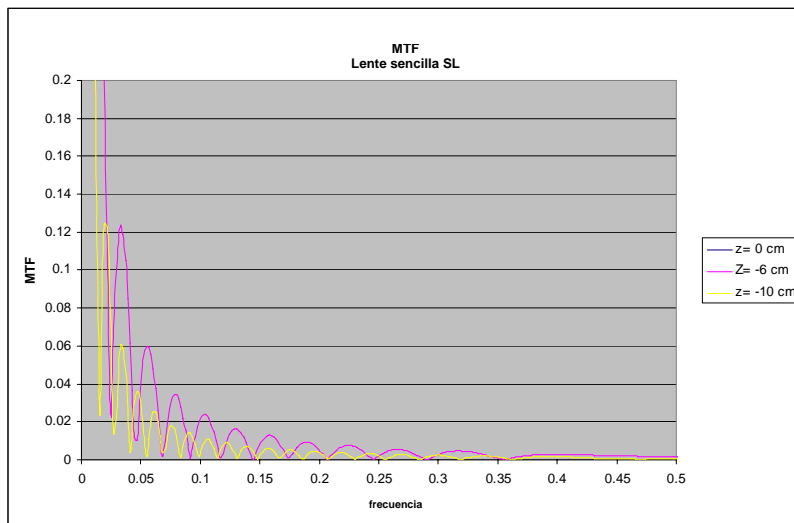


Figura 5.43. MTF de la lente sencilla SL en dos planos desenfocados, ampliación de la zona de frecuencias más bajas.

La Figura 5.44 y la Figura 5.45 muestran las MTF producidas por las lentes multiplexadas M9rand1 y M33rand1 respectivamente, en  $Z=0$  y en dos planos desenfocados. Si comparamos estas figuras con las obtenidas para la SL vemos que la MTF en el plano de mejor imagen es claramente mejor en la lente SL que en las multiplexadas. Ambas lentes multiplexadas producen un fuerte descenso en los valores de la MTF al separarnos ligeramente de la frecuencia espacial 0, por lo que es de esperar un fondo muy intenso superpuesto a la imagen del objeto extenso que se puede apreciar en los resultados experimentales del siguiente apartado. Este ruido de fondo se puede eliminar si se substraer un valor constante umbral al conjunto de la imagen. Para ello es necesario el uso de una cámara CCD con un gran rango dinámico que permita capturar correctamente la imagen.

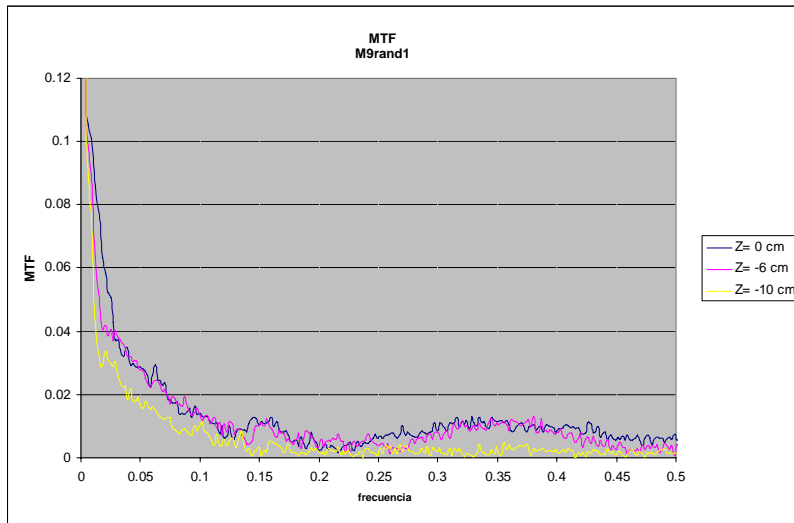


Figura 5.44. MTF de la lente multiplexada M9rand1 en el plano de mejor imagen ( $Z=0$ ) y en dos planos desenfocados.

La ventaja de utilizar las lentes multiplexadas M9rand1 y M33rand1 radica en que ofrecen una respuesta mucho mejor que la SL en los planos desenfocados. En la Figura 5.44 se puede observar cómo la lente M9rand1 no produce ninguna inversión de contraste en el rango de frecuencias espaciales [0-0,1], mientras que la SL produce hasta 4 inversiones de contraste para  $Z = -10$  cm en la misma zona del espectro (Figura 5.43). Sin embargo, con esta lente se producen dos inversiones en la región [0,1-0,45] para los planos  $Z = 0$  y  $Z = -60$  mm.

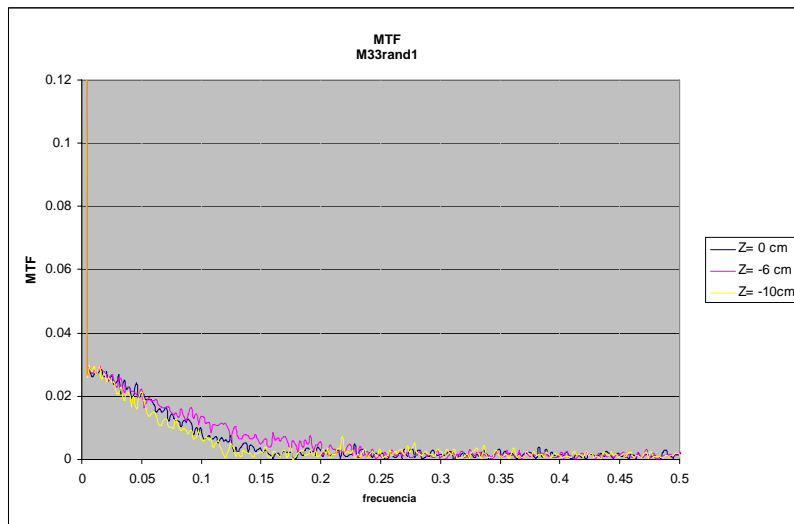


Figura 5.45. MTF de la lente multiplexada M33rand1 en el plano de mejor imagen ( $Z=0$ ) y en dos planos desenfocados.

La MTF para la lente M33rand1 (Figura 5.45) muestra un comportamiento todavía mejor para los planos desenfocados, con una caída suave sin inversiones

de contraste. Por ello, es de esperar una mejora en la calidad de la imagen en los planos desenfocados con esta lente multiplexada, respecto a los resultados obtenidos para la lente sencilla SL.

### 5.7.2 Resultados experimentales

Para obtener los resultados experimentales de las imágenes de objetos extensos producidas por las pupilas multiplexadas por el método aleatorio se ha realizado el montaje de la Figura 5.46.

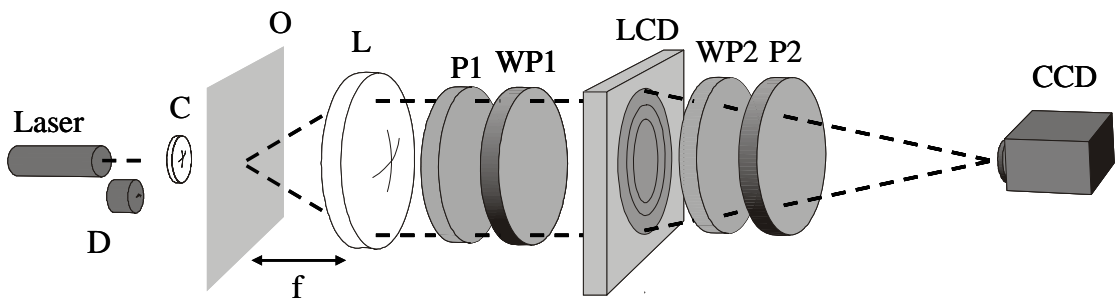


Figura 5.46. Montaje experimental para el estudio de las lentes multiplexadas con objetos extensos. El esquema es idéntico al de la Figura 5.10 salvo la inserción de un difusor rotatorio D y una pequeña lente condensadora C, así como la sustitución del filtro espacial puntual por un objeto extenso O. En este caso, además, las imágenes no se amplían y son capturadas directamente sobre la matriz CCD.

En este caso el montaje es idéntico al realizado para obtener las PSF (Figura 5.10), pero se ha substituido el filtro espacial por un conjunto formado por un difusor rotatorio D, con el fin de romper la coherencia de la fuente de luz y evitar efectos de interferencia indeseados, y un condensador C que ilumina de manera uniforme el objeto extenso O. Como se ha comentado anteriormente, la cámara CCD utilizada tiene un rango dinámico elevado, con 16.384 niveles de gris (14 bits).

Los objetos utilizados para llevar a cabo los experimentos han sido una estrella de Siemens y un test de resolución. En primer lugar se ha comparado la respuesta de la lente SL con las multiplexadas M9rand1 y M33rand1 en el plano Z=0. Los resultados se muestran en la Figura 5.47.

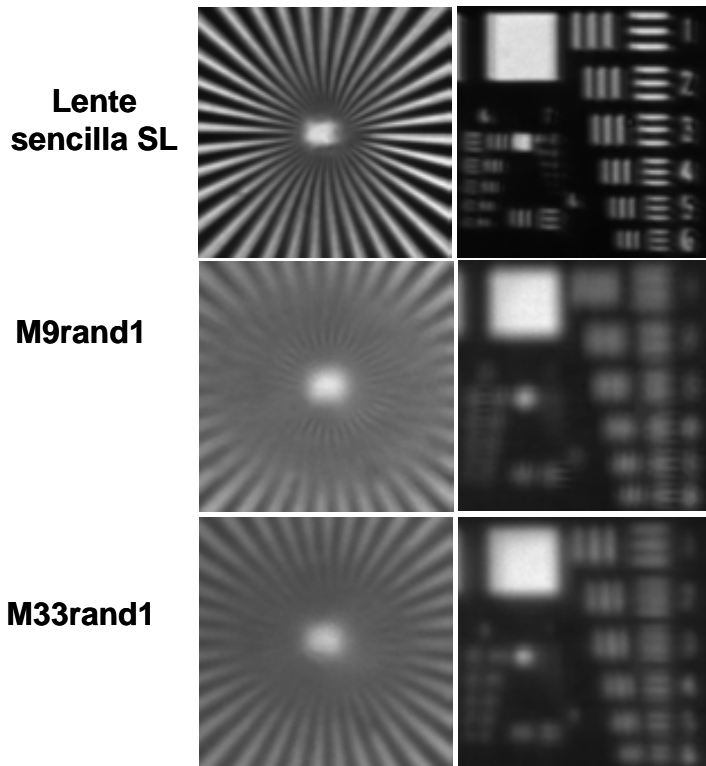


Figura 5.47. Comparación de los resultados experimentales para la imagen de la zona central del test de Siemens (columna de la izquierda) y para el test de resolución (columna de la derecha) en  $Z=0$ , utilizando la lente SL y las multiplexadas aleatorias de 9 lentes M9rand1 y de 33 lentes M33rand1.

Como es de esperar, la resolución empeora al utilizar las lentes multiplexadas respecto al resultado obtenido para la SL. Sin embargo, si se comparan los resultados entre la multiplexada de 9 lentes y la de 33 lentes se puede observar que en el test de Siemens obtenido con M9rand1 se producen dos inversiones de contraste, mientras que M33rand1 no produce inversiones de contraste en esta región de frecuencias espaciales, por lo que la calidad de la imagen mejora al incrementar el número de N de lentes en la multiplexada. Estos resultados están en concordancia con la MTF obtenida para estas dos lentes multiplexadas (ver apartado 5.7.1). Las imágenes del test de resolución (columna de la derecha de la Figura 5.47) también muestran que el comportamiento es más satisfactorio en el caso de la lente M33rand1 que al utilizar la lente M9rand1.

La Figura 5.48 muestra la zona central de la estrella de Siemens en Z=0 y en planos desenfocados con la lente sencilla SL y con la lente multiplexada M33rand1.

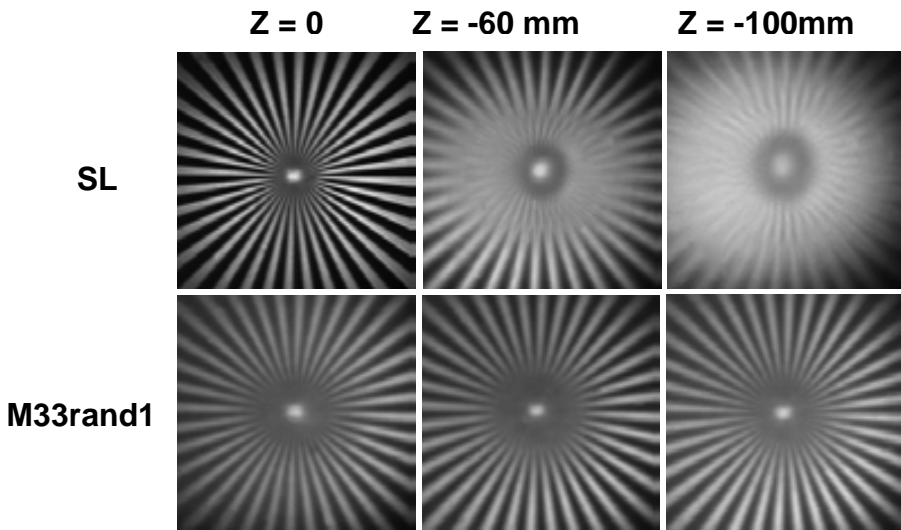


Figura 5.48. Imágenes de la estrella de Siemens capturadas en el plano de mejor imagen ( $Z=0$ ) y en planos desenfocados ( $Z = -60 \text{ mm}$  y  $Z = -100 \text{ mm}$ ) para una lente sencilla SL y para la lente multiplexada M33rand1.

Cuando se utiliza la lente multiplexada la imagen mantiene la misma calidad al desplazarnos a lo largo del eje óptico. Sin embargo, la lente SL ofrece la mejor calidad en el plano de mejor imagen  $Z = 0$  pero ésta decrece rápidamente al alejarnos de la lente.

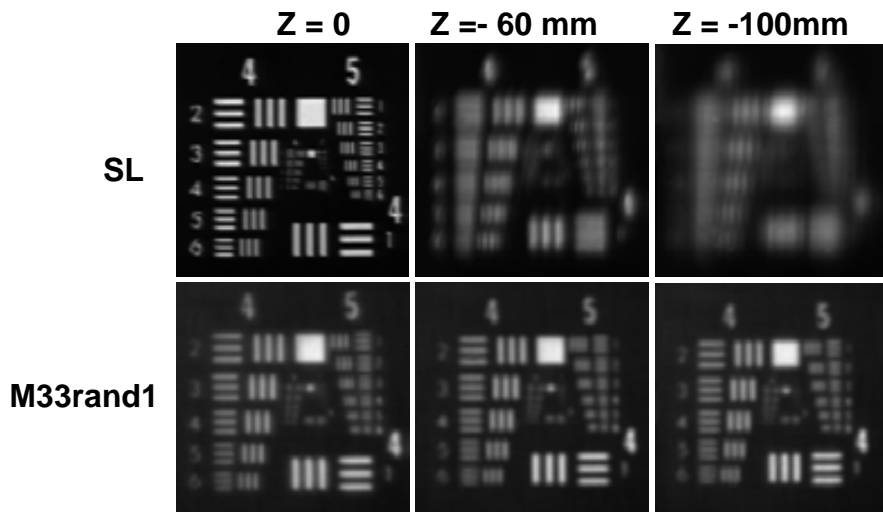


Figura 5.49. Imágenes de un test de resolución capturadas en el plano de mejor imagen ( $Z=0$ ) y en planos desenfocados ( $Z = -60 \text{ mm}$  y  $Z = -100 \text{ mm}$ ) para una lente sencilla SL y para la lente multiplexada M33rand1.

Lo mismo sucede con el test de desenfoque. Tal como se puede apreciar en la Figura 5.49, para  $Z=0$  la lente multiplexada produce un contraste y una resolución menores que la lente sencilla SL. Sin embargo, al capturar la imagen en planos desenfocados la lente multiplexada mantiene la resolución y el contraste mientras que con la SL la calidad de la imagen decrece considerablemente al alejarnos del plano de mejor imagen.

Estos resultados muestran que la calidad de una imagen extensa, en términos de resolución y contraste, se mantiene a lo largo de la distancia focal extendida al utilizar la lente multiplexada aleatoria de 33 lentes con subaperturas de un píxel.



## **Capítulo 6 Conclusiones**

En esta tesis se han investigado diferentes técnicas para generar elementos ópticos difractivos que modifican el perfil de intensidad a lo largo del eje y las propiedades de apodización e hiperresolución transversales de un sistema óptico. Los elementos ópticos difractivos que se han generado se han implementado en moduladores espaciales de luz de cristal líquido (LCSLM) y se han obtenido experimentalmente tanto las PSF en planos transversales a diferentes distancias del sistema, como la intensidad a lo largo del eje óptico.

La primera de las técnicas propuestas ha consistido en el diseño de pupilas complejas de transmisión no uniforme basado en la relación de Transformada de Fourier que existe entre la función compleja radial de una pupila con simetría axial y la función del perfil de intensidad a lo largo del eje óptico. Las pupilas se han obtenido mediante un algoritmo iterativo que tiene en cuenta las restricciones de resolución y tamaño del modulador, con el objeto de modificar arbitrariamente, según un determinado perfil deseado, el perfil de la intensidad a lo largo del eje en las proximidades del plano imagen. En el estudio de esta técnica se ha llegado a las siguientes conclusiones:

- Se ha implementado un método de cálculo numérico iterativo para el diseño de pupilas basado en la relación de Transformada de Fourier entre la función compleja radial de la pupila y la función del perfil de intensidad a lo largo del eje óptico, y que tiene en cuenta las restricciones de la pupila.

- Se ha comprobado numéricamente que el método iterativo propuesto para el diseño de las pupilas converge a funciones pupila que ofrecen respuestas en intensidad a lo largo del eje similares a los perfiles de intensidad deseados.
- Se ha realizado un montaje experimental para implementar las pupilas en un modulador espacial de luz y medir la respuesta en planos transversales a diferentes distancias a lo largo del eje óptico.
- Se ha comprobado que la codificación de estas pupilas complejas en fase y la implementación en moduladores sólo de fase mediante una técnica de codificación en fase basada en la difracción da resultados experimentales satisfactorios para la modificación del perfil de intensidad a lo largo del eje, en la dirección correspondiente al orden 1 de difracción.
- Se ha comprobado experimentalmente que la técnica modifica satisfactoriamente el perfil de intensidad a lo largo del eje dentro de su rango de validez, es decir, para zonas del eje óptico cercanas al plano de mejor imagen, tanto para perfiles rectangulares de diferentes anchuras (diferentes profundidades de foco) como para un perfil triangular, un perfil consistente en dos rectángulos de la misma altura (doble foco) y un perfil asimétrico consistente en dos rectángulos de diferentes alturas.
- Se ha comprobado experimentalmente que las pupilas obtenidas tienen un efecto hiperresolvente en los planos transversales desenfocados donde se fuerza que la intensidad en el eje sea elevada, en comparación con las imágenes obtenidas con una pupila uniforme.
- En el caso de los perfiles rectangulares se ha comprobado experimentalmente que la técnica es especialmente útil para el incremento de la profundidad de foco del sistema. Se han conseguido profundidades de foco de unos 60 mm para un sistema óptico que ofrece una profundidad de foco de unos 8 mm con pupila uniforme. Sin embargo, la técnica no

permite obtener hiperresolución a lo largo del eje, ya que para el caso extremo de un perfil deseado de tan sólo 2 puntos de anchura el resultado experimental es similar al obtenido mediante la pupila uniforme.

- En el caso del perfil consistente en dos rectángulos de la misma altura se ha comprobado experimentalmente que la técnica permite obtener de manera satisfactoria un sistema óptico bifocal a partir de un sistema óptico convergente.
- En el caso del perfil asimétrico consistente en dos rectángulos de diferentes alturas se ha comprobado que, al obtener los valores experimentales, se mantiene la relación de intensidades entre los máximos correspondientes a los dos rectángulos.

La segunda parte de este trabajo ha consistido en la propuesta de tres métodos para implementar lentes difractivas de potencias distintas en un solo LCSLM en configuración de modulación sólo de fase, y se ha evaluado su respuesta en relación al incremento de la DOF, al comportamiento hiperresolvente o apodizante en los planos transversales, y a la posibilidad de formar imágenes de objetos extensos. Se han propuesto los siguientes métodos: el multiplexado por sectores, el multiplexado por anillos y el multiplexado aleatorio. Se han obtenido resultados experimentales con los diferentes métodos para la PSF transversal a diferentes distancias, así como para el perfil de intensidad a lo largo del eje y se ha llegado a las siguientes conclusiones:

- Mediante el multiplexado por sectores se obtienen PSF transversales sin simetría axial. Se ha observado que la simetría de las PSF cerca del eje óptico no mejora al incrementar el número de lentes incluidas en la lente multiplexada. Debido a esta falta de simetría en la PSF se ha considerado que no es una técnica adecuada para incrementar la DOF ni para obtener imágenes de objetos extensos.

- Se ha observado que en el multiplexado por anillos es importante el orden en que se distribuyen las lentes de diferentes potencias en la lente multiplexada, es decir, si las lentes de mayor potencia están hacia el interior o hacia el exterior de la multiplexada.
- Se ha observado que el multiplexado por anillos proporciona perfiles de intensidad con máximos y mínimos muy definidos si el número de anillos es bajo. Al incrementar el número de anillos por lente los resultados mejoran. Se ha observado que la multiplexada compuesta por 33 lentes con 1 anillo asignado a cada potencia es la que proporciona los mejores resultados de cara a incrementar la DOF y formar imágenes extensas, con una profundidad de foco de unos 45 mm a lo largo de la cual la estructura de las PSF transversales se mantiene uniforme.
- Se ha observado que en el multiplexado aleatorio también proporciona perfiles de intensidad con máximos y mínimos muy definidos si el número de lentes es bajo.
- Se ha observado que asignar subaperturas de 1x1 píxeles para generar las lentes multiplexadas ofrece resultados notablemente mejores que asignar subaperturas de 8x8 píxeles, por lo que se refiere a la calidad de las PSF.
- Se ha observado que el multiplexado aleatorio con 33 lentes es el más satisfactorio para incrementar la DOF del sistema óptico, ya que permite obtener una DOF de 200 mm en un sistema óptico con una DOF original (para una sola lente de  $f=1000\text{mm}$  implementada en el modulador) de 10 mm. Esta opción de multiplexado proporciona un perfil de intensidad uniforme a lo largo de toda la DOF y una estructura de las PSF también uniforme a lo largo de ese intervalo, por lo que es muy adecuado para la formación de imágenes extensas.

- Se ha obtenido numéricamente la MTF para los multiplexados aleatorios de 9 lentes y de 33 lentes y se ha observado que el multiplexado de 33 lentes ofrece una respuesta mejor que la lente sola y que la multiplexada de 9 lentes en los planos desenfocados, con ausencia de inversiones de contraste.
- Por último, se ha comprobado experimentalmente la respuesta del multiplexado aleatorio para objetos extensos. Se ha observado que el multiplexado aleatorio de 33 lentes ofrece la mejor calidad, en términos de resolución y de contraste, a lo largo de toda la distancia focal extendida, en comparación con la multiplexada de 9 lentes (que presenta inversiones de contraste) y con la lente sola (con un decrecimiento muy rápido de la calidad al alejarnos del plano de mejor imagen).



## Referencias

- [All88] J. P. Allebach y D. W. Sweeney, Proc. Soc. Photo-Opt. Instrum. Eng. **884**, 2 (1988).
- [Ars01] H. H. Arsenault y P. García Martínez, “Diffraction theory in terms of quantum mechanics and relativity”, Proceedings of SPIE – Vol. 4435, Wave optics and VLSI photonic devices for information processing, pp. 7-15 (2001).
- [Bar89] T. H. Barnes, T. Eiju, K. Matsuda y N. Ooyama, “Phase-only modulation using a twisted nematic liquid crystal television”, Appl. Opt. **28** (22), 4845-4852 (1989).
- [Ben03] E. Ben-Eliezer, Z. Zalevsky, E. Marom y N. Konforti, “All-optical extended depth of field imaging system”, J. Opt. A: Pure Appl. Opt. **5**, S164-S169 (2003).
- [Ber95] A. Bergeron, J. Gauvin, F. Gagnon, D. Gingras, H. H. Arsenault y M. Doucet, “Phase calibration and applications of a liquid-crystal spatial light modulator”, Appl. Opt. **34**, 5133-5139 (1995).
- [Ber04] S. Bergamini, B. Darquié, M. Jones, L. Jacobowicz, A. Browaeys y P. Gragier, “Holographic generation of microtrap arrays for single atoms by use of a programmable phase modulator”, J. Opt. Soc. Am. B **21**, 1889-1894 (2004).
- [Bou97] J. L. de Bougrenet de la Tocnaye y L. Dupont, “Complex amplitude modulation by use of liquid-crystal spatial light modulators”, Appl. Opt. **36**, 1730-1741 (1997).
- [Bro66] B. R. Brown y A. W. Lohmann. “Complex spatial filtering with binary masks”, Appl. Opt. **5** (6), 967 (1966).

- [Bro69] B. R. Brown y A.W. Lohmann. “Computer-generated binary holograms”, IBM J. Res. Develop. 160-168 (Mar. 1969).
- [Bur70] C. B. Burckhardt, “A simplification of Lee’s method of generating holograms by computer”, Appl. Opt. **9**, 1949 (1970).
- [Cam00] J. Campos, A. Márquez, M. J. Yzuel, J. A. Davis, D. M. Cottrell e I. Moreno, “Fully complex synthetic discriminant functions written onto phase-only modulators”, Appl. Opt. **39**, 5965-5970 (2000).
- [Cat02] W. T. Cathey y E. R. Dowski, “New paradigm for imaging systems”, Appl. Opt. **41**, 6080-6092 (2002).
- [Chu73] D. S. Chu, I. R. Fienup y J. W. Goodman. “Multiemulsion on-axis computer generated hologram”, Appl. Opt **12**, 1386-1388, 1973.
- [Chu88] C. S. Chung y H. H. Hopkins, “Influence of non-uniform amplitude on PSF”, J. Mod. Opt. **35**, 1485-1511 (1988).
- [Coy96] J. A. Coy, M. Zaldarriaga, D. F. Grosz y O. E. Martínez, “Characterization of a liquid crystal television as a programmable spatial light modulator”, Opt. Eng. **35**, 15-99 (1996).
- [Dav94] J. A. Davis y D. Cottrell, “Random mask encoding of multiplexed phase-only and binary phase-only filters”, Opt. Lett. **19**, 496 (1994).
- [Dav99a] J. A. Davis, J. C. Escalera, J. Campos, A. Márquez, M. J. Yzuel y C. Iemmi, “Programmable axial apodizing and hyperresolving amplitude filters with a liquid-crystal spatial light modulator”, Opt. Lett. **24**, 628-630 (1999).
- [Dav99b] J. A. Davis, D. M. Cottrell, J. Campos, M. J. Yzuel e I. Moreno, “Encoding amplitude information onto phase only filters”, Appl. Opt. **38**, 5004-5013 (1999).

- [Dou95] R. Dou y M. K. Giles, “Close-loop adaptive optics system with a liquid crystal television as a phase retarder”, Opt. Lett. **20**, 1583-1585 (1995).
- [Dow95] E. R. Dowski Jr y W. T. Cathey, “Extended depth of field through wave-front coding”, Appl. Opt. **34**, 1859-1865 (1995).
- [Duf46] P. M. Duffieux, L'integrale de Fourier et ses applications a l'optique, Faculté des Sciences, Besançon (1946).
- [Efr95] U. Efron, editor, Spatial light modulator technology: materials, devices and applications, Marcel Dekker, New York (1995).
- [Esc95] J. C. Escalera, M. J. Yzuel y J. Campos, “Control of the polychromatic response of an optical system through the use of annular colour filters”, Appl. Opt. **34**, 1655-1663 (1995).
- [Fuk92] H. Fukuda, “A new pupil filter for annular illumination in optical lithography”, Jap. J. App. Phys. **31**, 4126-4139 (1992).
- [Goo04] J. W. Goodman, Introduction to Fourier Optics, McGraw-Hill, 3<sup>rd</sup> ed. (2004).
- [Gre86] D. A. Gregory, “Real-time pattern recognition using a modified liquid crystal television in a coherent optical correlator”, Appl. Opt. **25**, 467-469 (1986).
- [Hee75] E. W. S. Hee, “Fabrication of apodized apertures for laser beam attenuation”, Opt. Laser Tech. **4**, 75-79 (1975).
- [Heg85] Z. S. Hegedus, “Annular pupil arrays. Application to confocal scanning”, Opt. Acta. **32**, 815-826 (1985).
- [Her96] H. P. Herzig, editor, Micro-optics, Taylor & Francis, London (1996).

[Hil97] R. Hild, M. J. Yzuel y J. C. Escalera, “High focal depth imaging of small structures”, Microelectron. Engrg. **34**, 195-214 (1997).

[Hop49] H. H. Hopkins, “The disturbance near the focus of waves of radially non-uniform amplitude”, Proc. Phys. Soc. B **62**, 22 (1949)

[Hop50] H. H. Hopkins, Wave aberration theory, Oxford Clarendon Press (1950).

[Hop70] H. H. Hopkins y M. J. Yzuel, “The computation of diffraction patterns in the presence of aberrations”, Optica Acta **17**, 157-182 (1970).

[Hsu78] C. K. Hsueh y A. A. Sawchuck. “Computer-generated double-phase holograms”, Appl. Opt. **17** (24) 3874-3883 (1978).

[Huy1690] C. Huygens, Traite de Lumière, Academie des Sciences, Paris (1690).

[Ind84] G. Indebetow y H. Bai, “Imaging with Fresnel zone pupil masks: extended depth of field”, Appl. Opt. **23**, 4299-4302 (1984).

[Jac64] P. Jacquinot y B. Roizen-Dossier, “Apodisation”, in E.Wolf Ed. Progress in Optics, Vol. **3**, North Holland, (1964).

[Kir92] J. C. Kirsch, D. A. Gregory, M. W. Thie y B. K. Jones, “Modulation characteristics of the Epson liquid-crystal television”, Opt. Eng. **31**, 963-970 (1992).

[Kud97] A. V. Kudryashov, J. Ginglewski, S. Browne y R. Highland, “Liquid crystal phase modulator for adaptive optics. Temporal performance characterization”, Opt. Commun. **141**, 247-253 (1997).

[Lau98] V. Laude, “Twisted-nematic liquid-crystal pixelated active lens”, Opt. Commun. **153**, 134-152 (1998).

- [Led05] S. Ledesma, J. C. Escalera, J. Campos, y M. J. Yzuel, “Evolution of the transverse response of an optical system with complex filters”, Opt. Commun. **249**, 183-192 (2005).
- [Lee70] W. H. Lee. “Sampled Fourier transform hologram generated by computer”, Appl. Opt. **9**, 639-643, 1970.
- [Les69] L. B. Lesem, P. Hirsch y J. A. Jordan Jr. “The Kinoform: a new wavefront reconstruction device”, IBM J. Res. Develop. **13**, 150-155 (1969).
- [Li06] Guoquiang Li, David L. Mathine, et al., “Switchable electro-optic diffractive lens with high efficiency for ophthalmic applications”, PNAS **103**, 6100-6104 (2006).
- [Liu85] H.-K. Liu, J. A. Davis y R. A. Lilly, “Optical-data-processing properties of a liquid-crystal television spatial light modulator”, Opt. Lett. **10**, 635-637 (1985).
- [Löf00] B. Löfving y S. Härd, “Optical switching with two FLC SLMs”, Opt. Comm. **174**, 81-90 (2000).
- [Loh67] A. W. Lohmann y D. P. Paris. “Binary Fraunhofer holograms generated by computer”, Apl. Opt. **6** (1967).
- [Lop97] O. López-Coronado, “Caracterización in situ de moduladores espaciales de luz en un correlador óptico”, Trabajo de investigación, Universitat Autònoma de Barcelona, Bellaterra (1997).
- [Lop98] O. López-Coronado, I. Moreno, J. Campos y M. J. Yzuel, “Full in situ characterization of spatial light modulators in an optical correlator. Filter adaptation to operating curves”, J. Mod. Opt. **45**, 2461-2472 (1998).
- [Lov97] G. D. Love, “Wave-front production and correction of Zernike modes with a liquid-crystal spatial light modulator”, Appl. Opt. **36**, 1517-1524 (1997).

[Lu90] K. Lu y B. E. A. Saleh, “Theory and design of the liquid crystal TV as an optical spatial phase modulator”, Opt. Eng. **29**, 240-246 (1990).

[Mar00a] A. Márquez, J. Campos, M. J. Yzuel, I. Pascual, A. Fimia y A. Beléndez, “Production of computer-generated phase holograms using graphic devices. Application to correlation filters”, Opt. Eng. **39**, 1612-1619 (2000).

[Mar00b] A. Márquez et al., “Characterization of edge effects in twisted nematic liquid crystal displays”, Opt. Eng. **39** (19) 3301-3307 (2000).

[Mar01a] A. Márquez, C. Iemmi, J. C. Escalera, J. Campos, S. Ledesma, J. Davis y M. J. Yzuel, “Amplitude apodizers encoded onto Fresnel lenses implemented on a phase-only spatial light modulator”, Appl. Opt. **40**, 2316-2322 (2001).

[Mar01b] A. Márquez, C. Iemmi, I. Moreno, J. A. Davis, J. Campos y M. J. Yzuel, “Quantitative prediction of the modulation behavior of twisted nematic liquid crystal displays based on a simple physical model,” Opt. Eng. **40**, 2558-2564 (2001).

[Mar01c] A. Márquez, Accurate predictive model for twisted nematic liquid crystal devices. Application for generating programmable apodizers and Fresnel lenses, Tesis doctoral, Bellaterra, Junio 2001.

[Mar05a] A. Márquez, C. Iemmi, J. Campos, J. C. Escalera, y M. J. Yzuel, “Programmable apodizer to compensate chromatic aberration effects using a liquid crystal spatial light modulator”, Opt. Express **13**, 716-730 (2005).

[Mar05b] A. Márquez, C. Iemmi, I. Moreno, J. Campos y M. J. Yzuel, “Anamorphic and spatial frequency dependent phase modulation on liquid crystal displays. Optimization of the modulation difraction efficiency”, Opt. Express **13**, 2111-2119 (2005).

- [Mar06] A. Márquez, C. Iemmi, J. Campos, y M. J. Yzuel, “Achromatic diffractive lens written onto a liquid crystal display”, Opt. Lett. **31**, 392-394 (2006).
- [Mer82] N. S. Merzlyakov y L. P. Yaroslavky. Prikl. Vopr. Hologr. Tem. Sb., p.175 (1982).
- [Mil86] J. P. Mills y B. J. Thompson, “Effect of aberrations and apodization on the performance of coherent optical systems. I. The amplitude impulse response”, J. Opt. Soc. Am. **3**, 694-703 (1986).
- [Mil96] J. P. Mills y B. J. Thompson, editors, Selected papers on apodization-coherent optical systems, SPIE Milestone Series Vol. MS **119** (1996).
- [Mil06] M. S. Millán, J. Otón, E. Pérez-Cabré, “Chromatic compensation of programmable Fresnel lenses”, Opt. Express **14** (13) 6226-6242 (2006).
- [Mon06] M. Montes-Usategui, E. Pleguezuelos, J. Andilla y E. Martín-Badosa, “Fast generation of holographic optical tweezers by random mask encoding of Fourier components”, Opt. Express **14** (6) 2101-2107 (2006).
- [Mor95a] I. Moreno, C. Goreki, J. Campos, M. J. Yzuel, “Comparison of computer-generated holograms produced by laser printers and lithography: application to pattern recognition”, Opt. Eng. **34**, 3520-3525 (1995).
- [Mor95b] I. Moreno, J. Campos, C. Goreki y M. J. Yzuel, “Effects of amplitude and phase mismatching errors in the generation of a kinoform for pattern recognition”, Jap. J. Appl. Phys. **34**, 6423-6434 (1995).
- [Oje85] J. Ojeda-Castañeda, L. R. Berriel Valdos y E. Montes, “Spatial filter for increasing the depth of focus”, Opt. Lett. **10**, 520-522 (1985).
- [Oje86] J. Ojeda-Castañeda, P. Andrés y A. Díaz, “Annular apodizers for low sensitivity to defocus and to spherical aberration”, Opt. Lett. **11**, 487, 489 (1986).

[Oje89] J. Ojeda-Castañeda, E. Tepichin y A. Díaz, “Arbitrarily high focal depth with quasioptimum real and positive transmittance apodizer”, *Appl. Opt.* **28**, 2666-2670 (1989).

[Oje90] J. Ojeda-Castañeda y L. R. Berriel-Valdos, “Zone plate for arbitrarily high focal depth”, *Appl. Opt.* **29**, 994-996 (1990).

[Pas00] I. Pascual, A. Márquez, A. Beléndez, A. Fimia, J. Campos, M. J. Yzuel, “Copying low spatial frequency diffraction gratings in photopolymer as phase holograms”, *J. Mod. Opt.* **47**, 1089-1097 (2000).

[Pas92] I. Pascual, A. Beléndez y A. Fimia, “Holographic system for copying holograms by using partially coherent light”, *Appl. Opt.* **31**, 3312-3319 (1992).

[Ren05] J. Renu, J. Joby y S. Kehar, “Content-addressable Holographic Digital Data Storage Based on Hybrid Ternary Modulation with a Twisted-Nematic Liquid-Crystal Spatial Light Modulator”, *Opt. Rev.* **12**, 155-160 (2005).

[Ros91] J. Rosen y J. Shamir, “Application of the projection-onto-constraint sets algorithm for optical pattern recognition”, *Opt. Lett.* **16**, 752-754 (1991).

[Sau04] Sauceda A. y Ojeda-Castañeda J., “High focal depth with fractional-power wave fronts”, *Opt. Lett.* **29** (6), 560-562 (2004).

[Sal97] T. R. M Sales y G. M. Morris, “Diffractive superresolution elements”, *J. Opt. Soc. Am. A* **14**, 1637-1646 (1997).

[Ser99] S. Serati y K. Bauchert, “SLMs meet the challenge of new applications”, *Laser Focus World*, May, 229-233, (1999).

[She88] C. J. R. Sheppard y Z. S. Hegedus, “Influence of non-uniform amplitude on PSF” *J. Mod. Optics* **35** 1485-1511 (1988).

- [Shm76] E. K. Shmaryov. Opt. Spektrosk **41**, 905 (1976).
- [Sou94] C. Soutar y K. Lu, “Determination of the physical properties of an arbitrary twisted-nematic liquid crystal cell”, Opt. Eng. **33**, 2704-2712 (1994).
- [Sto91] T. W. Stone y B. J. Thompson, editors, Selected papers on holographic and diffractive lenses and mirrors, SPIE Milestone Series Vol. MS 34 (1991).
- [Str35] R. Straubel, P. Zeeman Verhandelingen, The Hague, M. Nijhoff, **302** (1935).
- [Tor52] G. Toraldo di Francia, “Super-gain antennas and optical resolving power”, Nuovo Cimento **9**, 426-438 (1952).
- [Tud02] R. Tudela, I. Labastida, E. Martín-Badosa, S. Vallmitjana, I. Juvells y A. Carnicer, “A simple method for displaying Fresnel holograms on liquid crystal panels”, Opt. Comm. **214** (2002).
- [Tud03] R. Tudela, E. Martín-Badosa, I. Labastida, S. Vallmitjana, I. Juvells, A. Carnicer. “Full complex Fresnel holograms displayed on liquid crystal devices”, Journal of Optics A. **5** (5), (2003).
- [Tur97] J. Turunen y F. Wyrowski, Diffractive optics for industrial and commercial applications, Akademie Verlag, Berlin (1997).
- [Van64] A. Vander Lugt, “Signal detection by complex spatial filtering”, IEEE Trans. Infor. Theory IT-10, **139** (1964).
- [Wan01] H. Wang y F. Gan, “High focal depth with a pure-phase apodizer”, Appl. Optics. **40**, 5658-5662 (2001).
- [Wel60] W. T. Welford, “Use of annular aperture to increase focal depth”, J. Opt. Soc. Am. A **50**, 749-753 (1960)

[Yam95] M. Yamauchi y T. Eiju, “Phase modulation capability of thin twisted nematic liquid crystal panels at double-pass configurations”, Opt.Rev. **2**, 24-27 (1995).

[Yam00] M. Yamauchi, A. Márquez, J. D. Davis y D. J. Franich, “Interferometric phase measurements for polarization eigenvectors in twisted nematic liquid crystal spatial light modulators”, Opt. Commun. **181**, 1-6 (2000).

[Yan99] G. G. Yang, “An optical pickup using a diffractive optical element for a high-density optical disc” Opt. Comm. **159**, 19-22 (1999).

[Yar80] L. P. Yaroslavsky y N.S.Merzlyakov. Methods of Digital Holography, Plenum Publishing Corporation (1980).

[Yar86] L. P. Yaroslavsky. Applied Problems of Digital Optics, Advances on Electronics and Electron Physics **66**, Ed. P.W.Hawkes, Academic Press (1986).

[Yar97] L. P. Yaroslavsky, O. López-Coronado y J. Campos, “Imput-image homogeneization as a method to improve a correlator’s discrimination capability”, Opt. Lett. **23** (14), 1129-1131 (1998).

[You82] D. C. Youla y H. Webb, “Image restoration by the method of convex projections: Part 1-Theory,” IEEE Trans. Med. Imaging MI-1, 81-94 (1982).

[Yzu80] M. J. Yzuel y F. J. Arlegui, “A study on the computation accuracy of the aberrational diffraction images”, Optica Acta **27**, 549-562 (1980).

[Yzu83] M. J. Yzuel y F. Calvo, “Point-spread function calculation for optical systems with residual aberrations and a non-uniform transmission pupil”, Optica Acta **30**, 233-242 (1983).

[Yzu88] M. J. Yzuel, J. C. Escalera, G. Cansado y J. Campos, “Illuminance and chromaticity of the image of optical systems with non-uniform transmission filters”, Proc. SPIE 1013, 120-127 (1988).

[Yzu90] M. J. Yzuel, J. C. Escalera y J. Campos, “Polychromatic axial behavior of axial apodizing and hyperresolving filters”, Appl. Opt. **29**, 1631- 1641 (1990).

[Zha94] Z. Zhang, G. Lu y F. T. S. Yu, “Simple method for measuring phase only modulation of a liquid crystal spatial light modulator”, Opt. Eng. **33** (9), 3018-3022 (1994).



## **Anexo**

### **Artículos publicados**

## Full *in-situ* characterization of spatial light modulators in an optical correlator. Filter adaptation to operating curves

OCTAVIO LÓPEZ-CORONADO<sup>†</sup>, IGNACIO MORENO<sup>†</sup>,  
JUAN CAMPOS<sup>†</sup> and MARÍA J. YZUEL<sup>†</sup>

<sup>†</sup> Departamento de Física, Universidad Autónoma de Barcelona,  
08193 Bellaterra, Spain

<sup>‡</sup> Departamento Interuniversitario de Óptica, Universidad de Valencia,  
46100 Burjassot, Spain

(Received 30 January 1998)

**Abstract.** In this paper we present one method for the characterization of the spatial light modulators (SLMs) of a real-time Vander Lugt type of correlator. This correlator uses two SLMs: one to introduce the scene and a second to introduce the frequency-matched filter. The SLM characterization methods are *in situ*, that is in the correlator set-up. Illumination conditions are different for each SLM, and consequently different characterization techniques must be used in each case. For the characterization of the scene SLM a diffraction method is used, while for the characterization of the filter SLM an interferometric technique is more convenient. Finally, we take into account the operating curves of scene and filter SLMs in the design of the filter in order to optimize the correlation peak.

### 1. Introduction

Spatial light modulators (SLMs) are optoelectronic devices widely used in optical processors. They have been used to build optical correlators that work in real time [1]. Vander Lugt correlators have two key elements which must be implemented in the optimal system: the input scene and the frequency-matched filter. The use of SLMs to implement both elements offers the possibility to analyse different scenes and use different filters in real time.

There exists a wide set of different SLM technologies. Liquid-crystal televisions (LCTVs) have become one of the most popular SLM technologies for optical processors [2]. In our case we use twisted nematic LCTVs. These SLMs produce, in general, coupled amplitude and phase modulation as a function of applied voltage. Nevertheless, in certain ranges of voltage and in certain orientations of input and output polarizers, they can produce amplitude mostly or phase mostly modulation [3].

The phase modulation properties of SLMs can be used to implement phase-only filters [4] in optical correlators. These are optimal filters in terms of light efficiency. The phase modulation can also be used in the input scene. Kallman and Goldstein [5] proposed encoding the amplitude input scene as a phase signal, with phase range from 0 to  $\pi$ . This transformation improves the light efficiency of the correlator [6]. However, in general, it is difficult to obtain perfect phase-only modulation, and this may cause the correlator performance to deteriorate. Paul-

Hus and Sheng [1] proposed a phase-dominant filter for the Epson LCTVs in a real-time optical correlator. Cohn and Horner [7] presented a statistical model to evaluate the effects on the correlation peak amplitude derived from phase errors produced when a phase-only filter is displayed on a LCTV in a correlator. In [3] a different model based on the Fourier transform is proposed to evaluate the impulse response of a phase-only filter implemented in a LCTV with amplitude and phase-mismatching errors. From the impulse response, the amplitude of the correlation peak is evaluated. In [8] and [9] the optimal implementation of a given filter in a restricted coding domain is studied. The influence of the coding domain has also been studied for the implementation of the input scene [10]. All these studies show the importance of having accurate measurements of the modulation produced by the SLMs in an optical correlator.

Several methods have been proposed in the literature to measure the amplitude and phase modulation. Amplitude modulation is obtained through measurements of intensity transmission. Phase modulation measurements require more sophisticated methods. One method consists in placing the SLM in one arm of an interferometer. The value of the phase modulation is obtained directly from the displacement of the interference fringes when two zones with different voltage are implemented in the SLM. Mach-Zehnder [3, 11, 12] and Michelson [13] interferometers have been used. Another interferometric method is based on producing two point sources on the SLM and to observe the interference pattern obtained from them [14, 15]. A difference of phase between the two sources produces a shift on the interference pattern. Diffractive methods can also be used to measure phase modulation. Zhang *et al.* [16] proposed implementing a Ronchi grating on the SLM and measuring the intensity of the zero and first diffraction orders. The phase modulation can be obtained from the relative intensities of these two diffraction orders. Other diffraction techniques have been proposed to measure the phase modulation [17, 18].

Amplitude and phase modulation are very sensitive to external parameters such as the input and output polarizer angles, ranges of voltage, and even ambience factors such as temperature [19]. Consequently these parameters must be controlled very accurately in order to be the same when the characterization is done and when the SLM is used in a given set-up. In order to obtain modulation curves that correspond exactly to the same external parameters that the SLM will have during the optical experiment, it can be very useful to use *in-situ* characterization methods, that is techniques where the characterization is performed in the same set-up where the SLM is used. In this sense, Gonçalves-Neto *et al.* [20] proposed the use of a wedge shear plate interferometer to measure *in situ* the operating modulation curve produced by the SLM used in an optical system for the generation of holograms by iterative techniques.

The aim of this work is to perform a full *in-situ* characterization of the SLMs inside an optical correlator. Different *in-situ* methods must be used for the SLM that implements the input scene and the SLM that implements the matched filter. In this work we use a diffractive method for the scene SLM characterization based on the diffraction pattern obtained from a Ronchi grating. The phase modulation value is obtained from the intensity of the zero and first diffraction orders. These diffraction orders generated by the grating are also used as point sources on the filter SLM plane. In the case of the filter SLM characterization an interferometric method is used. The phase modulation is obtained from the shift of the inter-

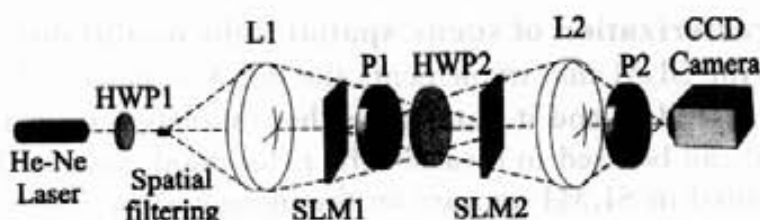


Figure 1. Real-time optical correlator. SLM1 implements the input scene and SLM2 implements a matched filter. P1 and P2 are polarizers; HWP1 and HWP2 are half-wave plates; L1 and L2 are convergent lenses.

ference fringes generated by the point sources when different grey levels are simultaneously addressed to different zones of the SLM. Also, the amplitude modulation of each SLM is obtained by measuring its intensity transmission. Finally, operating curves of both SLMs are taken into account to improve the correlator performance for pattern recognition. In order to consider the scene coding domain, the filter is matched to the target function modified by the restricted modulation curve of the input SLM. Then, to implement optimally the phase-only filter on the second SLM, the minimum Euclidean distance principle [8] is applied.

## 2. Real-time optical convergent correlator

A convergent correlator has been used in the experiments. This is a variant of the classical Vander Lugt correlator where the size of the Fourier transform (FT) of the scene can be adjusted to the size of the filter without changing the focal length of the lenses [21]. Figure 1 shows the scheme of a real-time convergent correlator. The system is illuminated with a polarized He-Ne laser with wavelength  $\lambda = 632.8\text{ nm}$ . Two SLMs, namely SLM1 and SLM2, are used to implement input scene and frequency-matched filter respectively. Adjusting the input polarization and output polarizer angle, these SLMs can produce amplitude-mostly or phase-mostly modulation. Nevertheless there is always certain coupling between amplitude and phase modulations. Two half-wave plates are placed in front of each SLM in order to control the orientation of the polarization of the incident beam and to select the desired modulation configuration. A linear polarizer is placed behind each SLM to select the desired polarization component, and to assure that the beam is linearly polarized.

The SLMs used in this work are two twisted nematic LCTVs extracted from an Epson video projector, model VP-100PS. These projectors have three LCTV panels corresponding to red, green and blue illumination. The applied voltage is controlled by three potentiometers called brightness, contrast and colour, and by the grey-level signal addressed from a frame grabber. The SLMs used in the correlator are controlled by a different video projector in order to permit an independent control of the voltages applied to each one. The SLM used for the implementation of the scene corresponds to blue illumination on the video projector, while the SLM used to implement the filter corresponds to green illumination.

### 3. In-situ characterization of scene spatial light modulator

In the case of the SLM that implements the input scene (SLM1 in figure 1), the light beam is extended, and it illuminates the complete screen. In this case, a diffractive method can be used to measure the phase modulation. The FT of the function implemented in SLM1 appears on the plane corresponding to the SLM that implements the filter (SLM2 in figure 1). In order to make the measurements of the FT pattern without changing the correlation set-up, a mirror or a beam splitter is introduced between the first polarizer P1 and the second half-wave plate HWP2 to deviate the beam. In the FT plane obtained outside the correlator, a radiometer is placed to measure light intensity values.

Amplitude modulation is measured by addressing a uniform screen on the SLM. All the energy is concentrated on the centre in the FT plane and it is a direct measure of the intensity transmission. Amplitude modulation is obtained by square root of the intensity transmission. In order to measure the phase modulation we use a diffraction technique proposed by Zhang *et al.* [16]. If a Ronchi grating is implemented on SLM1, characteristic diffraction orders are obtained on the FT plane. If two grey levels  $g_1$  and  $g_2$  are addressed to the SLM, the Ronchi grating will have two amplitude transmission levels  $t_1$  and  $t_2$ , and a relative phase shift  $\varphi$  between them. Except for a constant factor, the amplitude of the zero and first diffraction orders, namely  $A_0^s$ ,  $A_1^s$  and  $A_{-1}^s$ , can be expressed as a function of these parameters. The superscript s refers to the scene SLM (SLM1 in figure 1). They are given by the following expressions:

$$A_0^s = t_1 + t_2 \exp(i\varphi), \quad (1a)$$

$$A_1^s = \frac{2i}{\pi} [t_1 - t_2 \exp(i\varphi)], \quad (1b)$$

$$A_{-1}^s = -\frac{2i}{\pi} [t_1 - t_2 \exp(i\varphi)]. \quad (1c)$$

The intensities  $I_0^s$ ,  $I_1^s$  and  $I_{-1}^s$  of each diffraction order are given by

$$I_0^s = t_1^2 + t_2^2 + 2t_1t_2 \cos(\varphi), \quad (2a)$$

$$I_1^s = I_{-1}^s = \frac{4}{\pi^2} [t_1^2 + t_2^2 - 2t_1t_2 \cos(\varphi)]. \quad (2b)$$

The relative phase modulation can be expressed as a function of the grey levels  $g_1$  and  $g_2$  by the relation

$$\cos(\varphi) = \frac{R(g_1, g_2) - c}{T(g_1, g_2) - cR(g_1, g_2)}, \quad (3)$$

where  $R(g_1, g_2) = (I_0^s - I_1^s)/(I_0^s + I_1^s)$  is a relative measure of the intensities of the zero and first diffraction orders,  $T(g_1, g_2) = 2t_1t_2/(t_1^2 + t_2^2)$  is a factor that depends on the amplitude modulation, and  $c = (\pi^2 - 4)/(\pi^2 + 4) = 0.4232$  is a constant. Usually, grey level 0 is taken as a reference and the Ronchi grating has two grey levels: zero and a variable  $g$ . The phase modulation curve  $\varphi(g)$  is then obtained from the values of  $\cos(\varphi)$  with  $g_1 = 0$  and  $g_2 = g$ . Because of the multiple possible values of  $\varphi$  for each value of the  $\cos(\varphi)$  function, phase modulation  $\varphi$  is obtained from  $\cos(\varphi)$  by requiring that  $\varphi(0) = 0$  and by requiring the continuity of the phase modulation function with  $g$ .

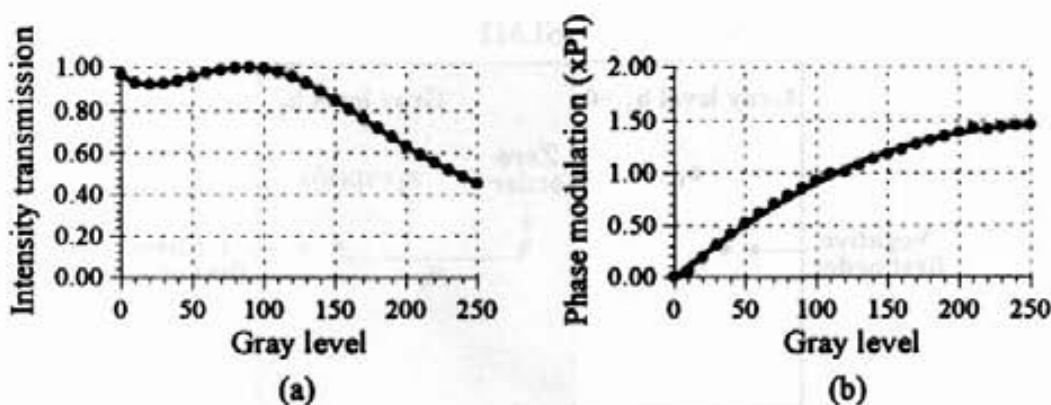


Figure 2. Modulation of SLM1 against grey level: (a) intensity transmission; (b) phase modulation.

Figure 2 shows the modulation results obtained with this technique. Control potentiometers of the Epson videoprojector are set to positions brightness 0, contrast 10 and colour 5. The incident beam is selected to be linearly polarized parallel to the liquid-crystal director at the input surface of the SLM. The output polarizer is placed with its transmission axis parallel to the director at the exit surface of the SLM. Figure 2(a) shows the intensity transmission against the grey level  $g$ , while figure 2(b) shows the phase modulation. Phase is an increasing function with grey level and in this case it has a maximum phase depth equal to  $1.5\pi$ . This configuration could be used in the scene of the correlator to implement phase encoded scenes, but with a coupled amplitude modulation.

#### 4. In-situ characterization of the filter spatial light modulator

Amplitude modulation of the SLM that implements the filter (SLM2 in figure 1) is obtained by measuring its intensity transmission, in the same way as for SLM1. However, the light beam converges towards the SLM2 plane and, consequently, the previous method used for measuring phase modulation of the scene SLM cannot be applied. In this case, for SLM2 phase modulation measurement, an interferometric technique can be used. If a Ronchi grating is implemented on the SLM1 with two grey levels  $g_1$  and  $g_2$  which correspond to amplitude transmissions  $t_1$  and  $t_2$  and a relative phase shift  $\varphi$ , then the diffraction orders are obtained in the SLM2. The frequency of the Ronchi grating is chosen in such a way that only the zero and the  $\pm 1$  orders fall inside the SLM2. These three diffraction orders act as point sources that produce an interference pattern over the charge-coupled device (CCD) camera. By changing the different voltages applied to the zones of SLM2 where these points are located the fringe pattern changes. We propose a method to measure the phase of the SLM2 by adding two interference patterns. Note that, as the incident beam in SLM2 comes from the first part of the correlator, it has exactly the same polarization orientation as it has in the correlation experiment.

The complex amplitude distribution in the plane just before SLM2 can be written as

$$E(u, v) = A_{-1}^s \delta(u - u_0, v) + A_0^s \delta(u, v) + A_1^s \delta(u + u_0, v), \quad (4)$$

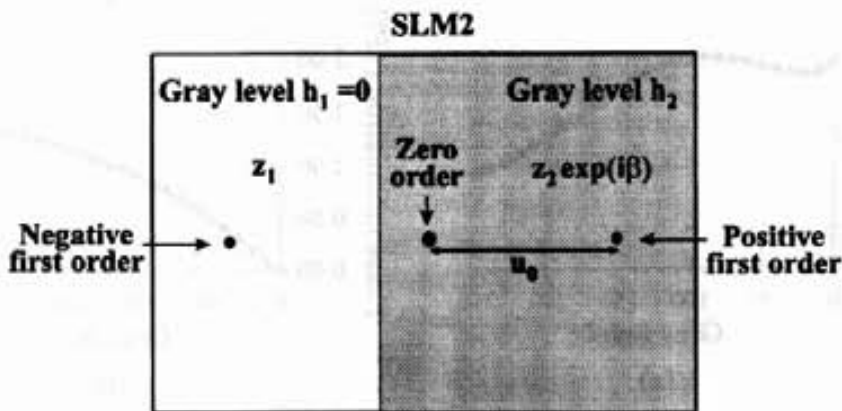


Figure 3. Distribution of the diffraction orders on the SLM2. Diffraction order  $-1$  is over a zone with grey level  $h_1 = 0$ , while  $0$  and  $+1$  orders are located over a zone with grey level  $h_2$ .

where  $A_{-1}^s$ ,  $A_0^s$  and  $A_1^s$  are the complex amplitudes given by equations (1 a), (1 b) and (1 c) respectively, and  $u_0$  is the distance between the central and the lateral point sources, which depends on the Ronchi grating frequency, the wavelength of the light and the distance between SLM1 and SLM2. Note that the superscript s still refers to scene SLM because these diffraction orders correspond to the Ronchi grating addressed to SLM1.

If the amplitude transmissions  $t_1$  and  $t_2$  are equal and the phase difference is  $\varphi = \pi$ , the term  $A_0^s$  in equation (1 a) is zero, and in consequence only two point sources are projected in the SLM2. In this case the method is similar to the methods proposed in [14] and [15] to characterize a SLM. However, it may happen that these conditions could not be obtained with the SLM used to display the image in the correlator.

The SLM2 screen is divided into two zones (figure 3), in such a way that the negative first order is placed over the first zone addressed with grey level  $h_1$ , while the zero and positive first orders are placed over a zone addressed with a grey level  $h_2$ . The amplitude transmissions of each zone are denoted by  $z_1$  and  $z_2$ , while the phase modulation difference between them is denoted by  $\beta$ . The complex amplitude distribution in the plane just behind SLM2 is then given by

$$E(u, v) = A_{-1}^s z_1 \delta(u - u_0, v) + A_0^s z_2 \exp(i\beta) \delta(u, v) + A_1^s z_2 \exp(-i\beta) \delta(u + u_0, v). \quad (5a)$$

Henceforth, the amplitudes of the diffraction orders will be written in polar form, that is  $A_0^s = a_0 \exp(i\alpha_0)$ ,  $A_1^s = a_1 \exp(i\alpha_1)$  and  $A_{-1}^s = -a_1 \exp(i\alpha_1)$ . Then, equation (5 a) becomes

$$E(u, v) = -a_1 z_1 \exp(i\alpha_1) \delta(u - u_0, v) + a_0 z_2 \exp(i\alpha_0 + i\beta) \delta(u, v) + a_1 z_2 \exp(i\alpha_1 + i\beta) \delta(u + u_0, v). \quad (5b)$$

The intensity of the FT of this distribution can be captured by the CCD camera of the correlator. It will be a pattern given by the interference of the beams coming from each point source, and it is given by

$$I_1^f = (a_0 z_2)^2 + (a_1 z_2)^2 + (a_1 z_1)^2 + 2a_0 a_1 z_2^2 \cos(\alpha_0 - \alpha_1 + 2\pi u_0 x) - 2a_0 a_1 z_1 z_2 \cos(\beta + \alpha_0 - \alpha_1 - 2\pi u_0 x) - 2a_1^2 z_1 z_2 \cos(\beta - 4\pi u_0 x), \quad (6)$$

where the superscript f refers to filter SLM characterization. This distribution consists of a constant term plus three interference patterns. Two patterns have a period equal to  $1/u_0$  and they are shifted proportionally to the value  $\beta$ . The third pattern has a period equal to  $1/2u_0$ .

If the two grey levels used in SLM1 to produce the Ronchi grating are interchanged, the amplitude  $A_0^s$  does not change, but  $A_1^s$  and  $A_{-1}^s$  change their signs. Consequently, if  $g_1$  and  $g_2$  are interchanged in SLM1, the interference pattern captured by the CCD camera will change to

$$\begin{aligned} I_2^f = & (a_0 z_2)^2 + (a_1 z_2)^2 + (a_1 z_1)^2 - 2a_0 a_1 z_2^2 \cos(\alpha_0 - \alpha_1 + 2\pi u_0 x) \\ & + 2a_0 a_1 z_1 z_2 \cos(\beta + \alpha_0 - \alpha_1 + 2\pi u_0 x) - 2a_1^2 z_1 z_2 \cos(\beta - 4\pi u_0 x). \end{aligned} \quad (7)$$

By adding these two interference patterns (equations (6) and (7)), a new distribution is obtained, given by

$$I^f = I_1^f + I_2^f = 2(a_0 z_2)^2 + 2(a_1 z_2)^2 + 2(a_1 z_1)^2 - 4a_1^2 z_1 z_2 \cos(\beta - 2\pi u_0 x). \quad (8)$$

This is a single interference pattern with a period equal to  $1/2u_0$ . The fringes are shifted proportionally to  $\beta$ , the phase modulation of SLM2. The coupled amplitude modulations  $z_1$  and  $z_2$  corresponding to the grey levels  $h_1$  and  $h_2$  addressed to SLM2 affect the contrast of the fringes but does not affect their position. Consequently it is possible to measure the phase modulation of SLM2 by measuring the shift in the fringes observed after the addition of the two interference patterns  $I_1^f$  and  $I_2^f$ . Again, the grey level  $h_1 = 0$  is taken as the reference, and the grey level  $h_2$  is varied from 0 to 255.

Figure 4 shows experimental interference patterns obtained with this technique. Figure 4(a) is the pattern  $I_1^f$  obtained when SLM2 has a uniform screen with grey level 0, that is  $h_1 = h_2 = 0$ . Different fringe patterns are produced by the interference of the beams coming from each point source. Figure 4(b) corresponds to the interference pattern  $I_2^f$  obtained when grey levels  $g_1$  and  $g_2$  are interchanged in SLM1. Figure 4(c) is the result of the addition of the two previous patterns and it is observed that the interference pattern has the slope of a cosinus function, as in equation (8). If the procedure is repeated with the same grey levels  $g_1$  and  $g_2$  on SLM1, but with grey levels  $h_1 = 0$  and  $h_2 = 80$  on SLM2, we obtain two interference patterns the addition of which is shown in figure 4(d). A shift of about half a fringe is observed in the interference pattern with respect to figure 4(c), which corresponds approximately to a phase modulation  $\beta = \pi$ .

Figures 5(a) and (b) show a profile of the interference of figures 4(c) and (d) respectively. As can be observed, experimental fringe patterns are noisy. The determination of fringe displacements becomes inaccurate because of the difficulty in determining the position of the maxima. In order to evaluate more precisely the shift between the experimental fringe patterns, say  $I^f(0)$  and  $I^f(h)$  (figures 5(a) and (b)) we calculate the autocorrelation of  $I^f(0)$  (figure 5(c)) and we compare it with the correlation between  $I^f(0)$  and  $I^f(h)$  (figure 5(d)). Figure 5(d) has the same shape as figure 5(c), but shifted the same value (in periods) as the original fringe displacement (figure 5(b) with respect to figure 5(a)). Because of noise reduction, this method provides a more precise way to obtain the fringe shift than to measure it directly from the interference pattern.

Figure 6 shows experimental modulation results obtained with this technique for the filter SLM. Figure 6(a) corresponds to the intensity transmission while

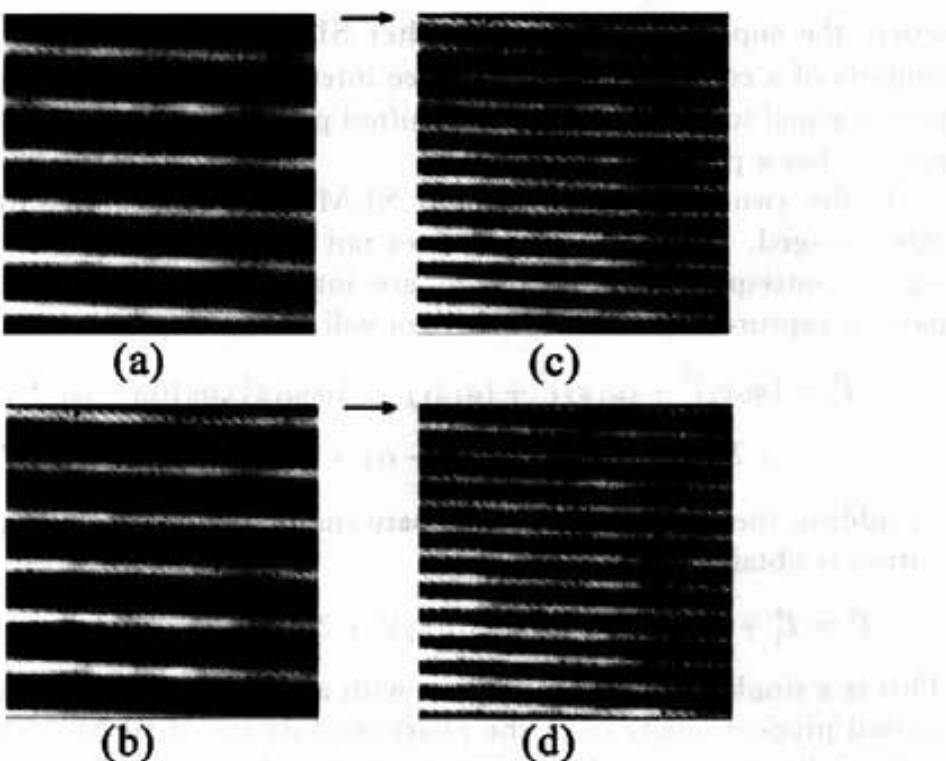


Figure 4. (a) Interference pattern  $I_1^f$  obtained when a Ronchi grating with grey levels  $g_1$  and  $g_2$  is implemented on SLM1 and a uniform screen of grey level 0 is addressed to SLM2; (b) interference pattern  $I_2^f$  obtained when the levels  $g_1$  and  $g_2$  of the grating implemented on SLM1 are interchanged; (c) addition  $I_1^f + I_2^f$ ; (d) addition  $I_1^f + I_2^f$  obtained when SLM2 has two zones with grey levels 0 and 80. A shift of half a fringe is observed with respect to (c). The arrows indicate the same pixel on the CCD camera.

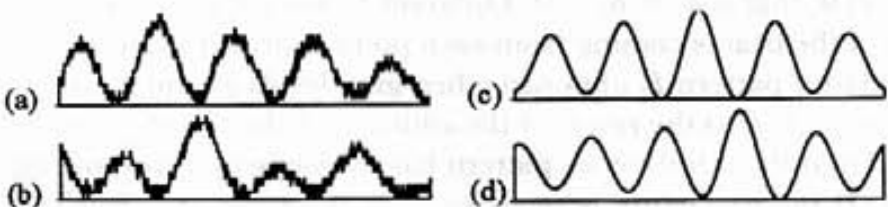


Figure 5. Profiles of two experimental interference fringe patterns for two different configurations of SLM2: (a) grey levels  $h_1 = 0$  and  $h_2 = 0$ ; (b) grey levels  $h_1 = 0$  and  $h_2 = 100$ ; (c) autocorrelation of the fringe pattern (a); (d) correlation between fringe patterns (a) and (b).

figure 6 (b) corresponds to the phase modulation. The control potentiometers have been placed at positions brightness 0, contrast 10 and colour 10. The phase modulation depth of this SLM reaches a maximum value of  $1.7\pi$ . The coupled amplitude modulation is very strong, mainly for high grey levels. This kind of modulation can be used to implement a phase-only filter, but the restriction in the phase modulation ( $1.7\pi$  maximum phase modulation) and the coupled amplitude modulation will cause its response to deteriorate.

## 5. Full adaptation to operating curves

Once the complete characterization of the two SLMs of the correlator has been performed, it is possible to adapt the system in order to improve the correlation.

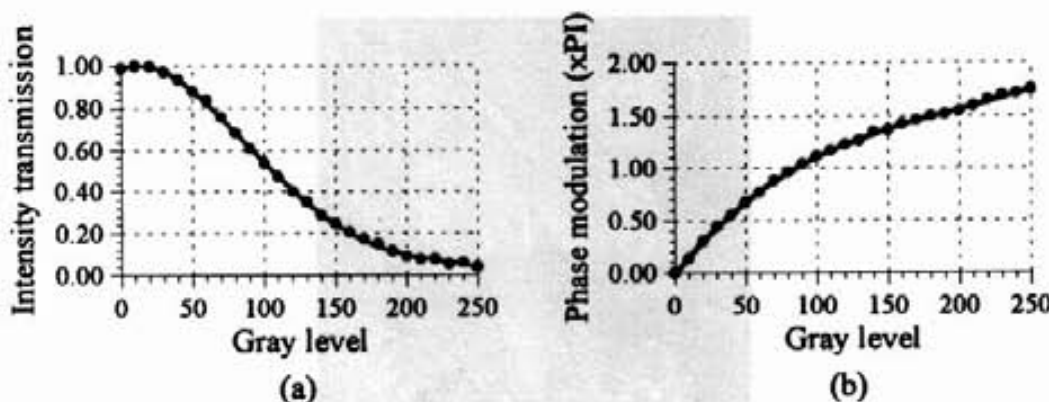


Figure 6. Modulation of SLM2 against grey level: (a) intensity transmission; (b) phase modulation.

The first step considered is to match the filter to the target object modified by the modulation curve of the SLM1. As shown in section 2, SLM1 produces good phase modulation, allowing phase encoding of the input scene [5]. Let  $s(x, y)$  represent the input amplitude scene, that is it is a function in the range  $[0, 1]$ . Let  $h(x, y)$  represent the target object to be recognized on the scene. The phase-encoding algorithm consists in transforming the input signal  $s(x, y)$  into a phase-only signal  $s'(x, y)$  given by

$$s'(x, y) = \exp[ik\pi s(x, y)], \quad (9)$$

where the constant  $k$  is usually taken to be equal to one in order to keep the monotonicity of the input signal in the phase signal. The reference object  $h(x, y)$  is transformed in the same way giving the phase-only signal  $h'(x, y)$  to which the filter is matched. In our case, the filter used is the phase-only filter [4]. This filter is obtained by calculating the FT of the target object to be recognized (in our case the function  $h'(x, y)$ ) and by using the complex conjugated phase distribution. This phase-only distribution may be implemented by a SLM that produces phase-only modulation between 0 and  $2\pi$ . When the phase-encoded scene and the phase-only filter are used, the correlator is optimal in terms of light efficiency.

When using real SLMs it is difficult to obtain perfect phase-only modulation. In this section we shall show firstly a numerical simulation of the experimental correlation process obtained with real SLMs. When the signal  $s(x, y)$  is addressed to the SLM1 it is converted into a signal  $s'_{\text{SLM}1}(x, y)$  different from the phase-only signal  $s'(x, y)$ . If the operating curve of SLM1 is taken into account in the filter generation, the phase-only filter can be matched to the simulation  $h'_{\text{SLM}1}(x, y)$  instead of being matched to the signal  $h'(x, y)$ . To illustrate the effect of the coding of the scene in the correlation results, the image shown in figure 7 has been used. The target object is the butterfly at the top of the figure. Figure 8 shows computer simulations obtained using as the input scene the function  $s'_{\text{SLM}1}(x, y)$  implemented by SLM1. Figure 8(a) corresponds to the case where a phase-only filter is matched to the function  $h'(x, y)$ , that is the reference object encoded as a perfect phase function. Figure 8(b) corresponds to the case where a phase-only filter is matched to the function  $h'_{\text{SLM}1}(x, y)$ . As expected, the perfect match of the phase-only filter gives a higher correlation peak, resulting in easier detection. The value of the maximum of the correlation peak is indicated on each figure.

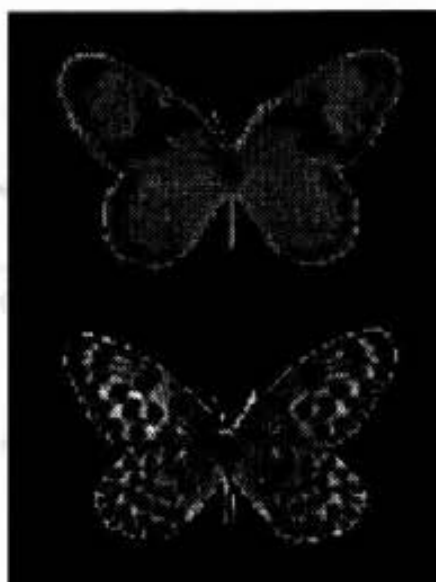


Figure 7. Input scene. The target object is the butterfly at the top of the figure.

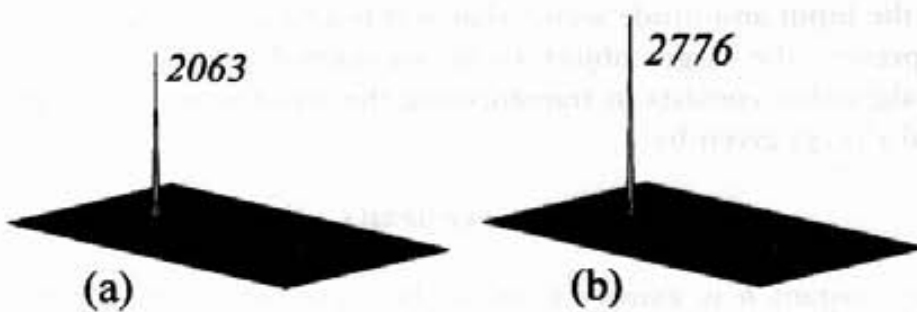


Figure 8. Computer simulation results using the scene  $s'_{\text{SLM}1}(x, y)$  and a phase-only filter matched to (a) a phase-encoded function  $h'(x, y)$  and (b) a function  $h'_{\text{SLM}1}(x, y)$ .

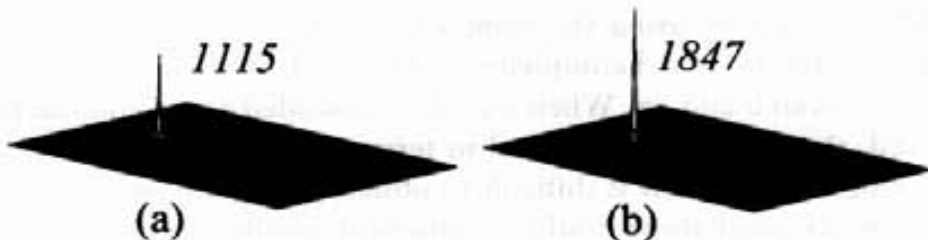


Figure 9. Computer simulation results using the scene  $s'_{\text{SLM}1}(x, y)$  and (a) a phase-only filter matched to the phase-encoded function  $h'(x, y)$  and directly implemented on SLM2, and (b) a phase-only filter matched to the function  $h'_{\text{SLM}1}(x, y)$  and implemented on SLM2 following the minimum-Euclidean-distance algorithm.

In the previous results, we have simulated a perfect phase-only filter. However, as pointed out in section 4, the phase modulation of SLM2 is restricted to a maximum depth of  $1.7\pi$  and has an important coupled amplitude modulation. These restrictions will cause the correlation distribution to deteriorate. The optimal implementation of a given filter in a restricted coding domain is given by the Euclidean projection of every complex point to its closest point belonging to the coding domain [8, 9]. Figure 9 shows computer simulation results obtained when the operating curves of SLM1 and SLM2 are considered. The input scene is

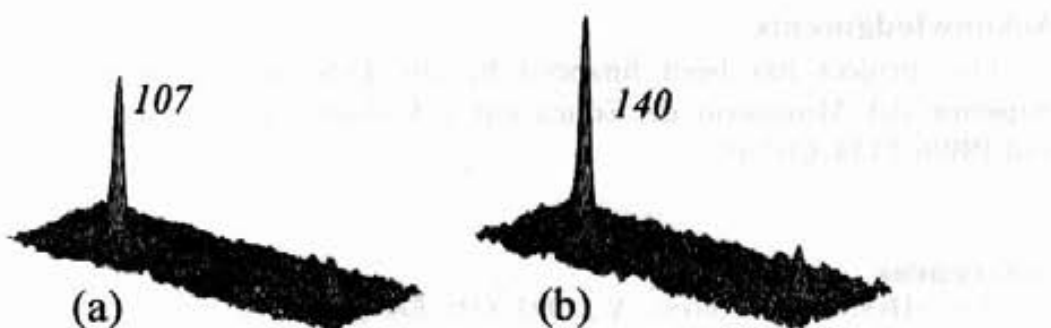


Figure 10. Optical correlation results: (a) filter matched to the phase-encoded function  $h'(x,y)$ ; (b) filter matched to the function  $h'_{SLM1}(x,y)$  and implemented on SLM2 following the minimum-Euclidean-distance algorithm.

the function  $s'_{SLM1}(x,y)$  implemented by SLM1. Figure 9(a) corresponds to the case in which the phase-only filter is matched to the function  $h'(x,y)$ , and it is addressed directly to SLM2. Because the operating curve of SLM2 is not a phase-only curve, the correlation peak is reduced with respect to the value in figure 8(a). Figure 9(b) corresponds to the case where the phase-only filter has been matched to the function  $h'_{SLM1}(x,y)$  and it has been adapted to the SLM2 operating curve following the minimum Euclidean distance algorithm. A higher correlation peak is obtained, although it does not reach the value obtained with a perfect phase-only filter (figure 8(b)).

Finally, the correlator has been used for optical correlation experiments. Figure 10(a) shows the experimental correlation obtained when the filter is matched to the phase-encoded function  $h'(x,y)$ . Although SLM1 does not produce a phase-only modulation, a good correlation peak is obtained. Figure 10(b) corresponds to the case in which the phase-only filter is matched to the function  $h'_{SLM1}(x,y)$  and it is implemented on SLM2 with the minimum Euclidean distance algorithm. An improvement in the correlation is observed and the value of the autocorrelation peak increases about 30%. These experimental results confirm the numerical results shown in figure 9.

## 6. Conclusions

Methods for performing *in-situ* characterization of the two SLMs of a Vander Lugt correlator are presented. The scene and filter SLMs require different methods because the conditions of illumination are different in each case. In the case of the scene SLM the whole screen is illuminated and a diffractive method can be used. The measured modulation is the mean response of all pixels of the SLM. On the other hand, the filter SLM is illuminated by a converging beam. An interferometric method is more convenient. We proposed and demonstrated a technique to measure the phase modulation of the filter SLM that uses three point sources generated by a grating implemented on the scene SLM. Finally, it has been demonstrated both numerically and experimentally that an adaptation of the correlation process to the operating curves of both SLMs produces higher correlation peaks.

## Acknowledgments

This project has been financed by the Dirección General de Enseñanza Superior del Ministerio de Educación y Cultura, projects PB96-1134-C02-01 and PB96-1134-C02-02.

## References

- [1] PAUL-HUS, G., and SHENG, Y., 1993, *Opt. Engng.*, **32**, 2165.
- [2] EFRON, U., 1995, *Spatial Light Modulator Technology: Materials, Devices and Applications* (New York: Marcel Dekker).
- [3] MORENO, I., CAMPOS, J., GORECKI, C., and YZUEL, M. J., 1995, *Jap. J. appl. Phys.*, **34**, 6423.
- [4] HORNER, J. L., and GIANINO, P. D., 1982, *Appl. Optics*, **23**, 812.
- [5] KALLMAN, R. R., and GOLDSTEIN, D. H., 1994, *Opt. Engng.*, **33**, 1806.
- [6] STYCZYNSKI, K., CAMPOS, J., YZUEL, M. J., and CHALASINSKA-MACUKOW, K., 1995, *Optics Commun.*, **118**, 193.
- [7] COHN, R. W., and HORNER, J. L., 1994, *Appl. Optics*, **33**, 5432.
- [8] JUDAY, R. D., 1994, *Appl. Optics*, **32**, 5100.
- [9] LAUDE, V., and RÉFRÉGIER, PH., 1994, *Appl. Optics*, **33**, 4465.
- [10] MAZÉ, S., and RÉFRÉGIER, PH., 1994, *Appl. Optics*, **33**, 6788.
- [11] KIRSCH, J. C., GREGORY, D. A., THIE, M. W., and JONES, B. K., 1992, *Opt. Engng.*, **31**, 963.
- [12] LAUDE, V., MAZÉ, S., CHAVEL, P., and RÉFRÉGIER, PH., 1992, *Optics Commun.*, **103**, 33.
- [13] YAMAUCHI, M., and EIJI, T., 1992, *Opt. Rev.*, **2**, 24.
- [14] SOUTAR, C., MONROE, S. E., JR, and KNOPP, J., 1994, *Opt. Engng.*, **33**, 1061.
- [15] BERGERON, A., GAUVIN, J., GAGNON, F., GINGRAS, D., ARSENAULT, H. H., and DOUCET, M., 1995, *Appl. Optics*, **34**, 5133.
- [16] ZHANG, Z., LU, G., and YU, F. T. S., 1994, *Opt. Engng.*, **33**, 3018.
- [17] McLAIN, J. L., JR., ERBACH, P. S., GREGORY, D. A., and YU, F. T. S., 1996, *Opt. Engng.*, **35**, 951.
- [18] SERRANO-HEREDIA, A., LU, G., PURWOSUMARTO, P., and YU, F. T. S., 1996, *Opt. Engng.*, **35**, 2680.
- [19] LU, K., and SALEH, B. E. A., 1990, *Opt. Engng.*, **29**, 6423.
- [20] GONÇALVES-NETO, L., ROBERGE, D., and SHENG, Y., 1995, *Appl. Optics*, **34**, 1944.
- [21] VANDER LUGT, A., 1992, *Optical Signal Processing* (New York: Wiley).

## Full *in-situ* characterization of spatial light modulators in an optical correlator. Filter adaptation to operating curves

OCTAVIO LÓPEZ-CORONADO<sup>†</sup>, IGNACIO MORENO<sup>†</sup>,  
JUAN CAMPOS<sup>†</sup> and MARÍA J. YZUEL<sup>†</sup>

<sup>†</sup> Departamento de Física, Universidad Autónoma de Barcelona,  
08193 Bellaterra, Spain

<sup>‡</sup> Departamento Interuniversitario de Óptica, Universidad de Valencia,  
46100 Burjassot, Spain

(Received 30 January 1998)

**Abstract.** In this paper we present one method for the characterization of the spatial light modulators (SLMs) of a real-time Vander Lugt type of correlator. This correlator uses two SLMs: one to introduce the scene and a second to introduce the frequency-matched filter. The SLM characterization methods are *in situ*, that is in the correlator set-up. Illumination conditions are different for each SLM, and consequently different characterization techniques must be used in each case. For the characterization of the scene SLM a diffraction method is used, while for the characterization of the filter SLM an interferometric technique is more convenient. Finally, we take into account the operating curves of scene and filter SLMs in the design of the filter in order to optimize the correlation peak.

### 1. Introduction

Spatial light modulators (SLMs) are optoelectronic devices widely used in optical processors. They have been used to build optical correlators that work in real time [1]. Vander Lugt correlators have two key elements which must be implemented in the optimal system: the input scene and the frequency-matched filter. The use of SLMs to implement both elements offers the possibility to analyse different scenes and use different filters in real time.

There exists a wide set of different SLM technologies. Liquid-crystal televisions (LCTVs) have become one of the most popular SLM technologies for optical processors [2]. In our case we use twisted nematic LCTVs. These SLMs produce, in general, coupled amplitude and phase modulation as a function of applied voltage. Nevertheless, in certain ranges of voltage and in certain orientations of input and output polarizers, they can produce amplitude mostly or phase mostly modulation [3].

The phase modulation properties of SLMs can be used to implement phase-only filters [4] in optical correlators. These are optimal filters in terms of light efficiency. The phase modulation can also be used in the input scene. Kallman and Goldstein [5] proposed encoding the amplitude input scene as a phase signal, with phase range from 0 to  $\pi$ . This transformation improves the light efficiency of the correlator [6]. However, in general, it is difficult to obtain perfect phase-only modulation, and this may cause the correlator performance to deteriorate. Paul-

Hus and Sheng [1] proposed a phase-dominant filter for the Epson LCTVs in a real-time optical correlator. Cohn and Horner [7] presented a statistical model to evaluate the effects on the correlation peak amplitude derived from phase errors produced when a phase-only filter is displayed on a LCTV in a correlator. In [3] a different model based on the Fourier transform is proposed to evaluate the impulse response of a phase-only filter implemented in a LCTV with amplitude and phase-mismatching errors. From the impulse response, the amplitude of the correlation peak is evaluated. In [8] and [9] the optimal implementation of a given filter in a restricted coding domain is studied. The influence of the coding domain has also been studied for the implementation of the input scene [10]. All these studies show the importance of having accurate measurements of the modulation produced by the SLMs in an optical correlator.

Several methods have been proposed in the literature to measure the amplitude and phase modulation. Amplitude modulation is obtained through measurements of intensity transmission. Phase modulation measurements require more sophisticated methods. One method consists in placing the SLM in one arm of an interferometer. The value of the phase modulation is obtained directly from the displacement of the interference fringes when two zones with different voltage are implemented in the SLM. Mach-Zehnder [3, 11, 12] and Michelson [13] interferometers have been used. Another interferometric method is based on producing two point sources on the SLM and to observe the interference pattern obtained from them [14, 15]. A difference of phase between the two sources produces a shift on the interference pattern. Diffractive methods can also be used to measure phase modulation. Zhang *et al.* [16] proposed implementing a Ronchi grating on the SLM and measuring the intensity of the zero and first diffraction orders. The phase modulation can be obtained from the relative intensities of these two diffraction orders. Other diffraction techniques have been proposed to measure the phase modulation [17, 18].

Amplitude and phase modulation are very sensitive to external parameters such as the input and output polarizer angles, ranges of voltage, and even ambience factors such as temperature [19]. Consequently these parameters must be controlled very accurately in order to be the same when the characterization is done and when the SLM is used in a given set-up. In order to obtain modulation curves that correspond exactly to the same external parameters that the SLM will have during the optical experiment, it can be very useful to use *in-situ* characterization methods, that is techniques where the characterization is performed in the same set-up where the SLM is used. In this sense, Gonçalves-Neto *et al.* [20] proposed the use of a wedge shear plate interferometer to measure *in situ* the operating modulation curve produced by the SLM used in an optical system for the generation of holograms by iterative techniques.

The aim of this work is to perform a full *in-situ* characterization of the SLMs inside an optical correlator. Different *in-situ* methods must be used for the SLM that implements the input scene and the SLM that implements the matched filter. In this work we use a diffractive method for the scene SLM characterization based on the diffraction pattern obtained from a Ronchi grating. The phase modulation value is obtained from the intensity of the zero and first diffraction orders. These diffraction orders generated by the grating are also used as point sources on the filter SLM plane. In the case of the filter SLM characterization an interferometric method is used. The phase modulation is obtained from the shift of the inter-

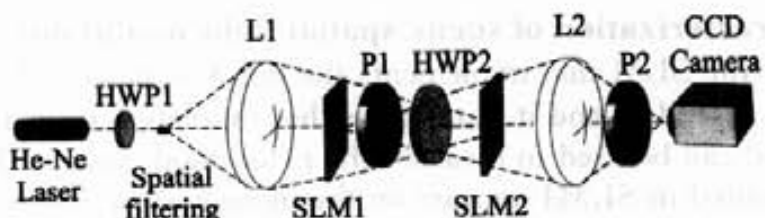


Figure 1. Real-time optical correlator. SLM1 implements the input scene and SLM2 implements a matched filter. P1 and P2 are polarizers; HWP1 and HWP2 are half-wave plates; L1 and L2 are convergent lenses.

ference fringes generated by the point sources when different grey levels are simultaneously addressed to different zones of the SLM. Also, the amplitude modulation of each SLM is obtained by measuring its intensity transmission. Finally, operating curves of both SLMs are taken into account to improve the correlator performance for pattern recognition. In order to consider the scene coding domain, the filter is matched to the target function modified by the restricted modulation curve of the input SLM. Then, to implement optimally the phase-only filter on the second SLM, the minimum Euclidean distance principle [8] is applied.

## 2. Real-time optical convergent correlator

A convergent correlator has been used in the experiments. This is a variant of the classical Vander Lugt correlator where the size of the Fourier transform (FT) of the scene can be adjusted to the size of the filter without changing the focal length of the lenses [21]. Figure 1 shows the scheme of a real-time convergent correlator. The system is illuminated with a polarized He-Ne laser with wavelength  $\lambda = 632.8\text{ nm}$ . Two SLMs, namely SLM1 and SLM2, are used to implement input scene and frequency-matched filter respectively. Adjusting the input polarization and output polarizer angle, these SLMs can produce amplitude-mostly or phase-mostly modulation. Nevertheless there is always certain coupling between amplitude and phase modulations. Two half-wave plates are placed in front of each SLM in order to control the orientation of the polarization of the incident beam and to select the desired modulation configuration. A linear polarizer is placed behind each SLM to select the desired polarization component, and to assure that the beam is linearly polarized.

The SLMs used in this work are two twisted nematic LCTVs extracted from an Epson video projector, model VP-100PS. These projectors have three LCTV panels corresponding to red, green and blue illumination. The applied voltage is controlled by three potentiometers called brightness, contrast and colour, and by the grey-level signal addressed from a frame grabber. The SLMs used in the correlator are controlled by a different video projector in order to permit an independent control of the voltages applied to each one. The SLM used for the implementation of the scene corresponds to blue illumination on the video projector, while the SLM used to implement the filter corresponds to green illumination.

### 3. In-situ characterization of scene spatial light modulator

In the case of the SLM that implements the input scene (SLM1 in figure 1), the light beam is extended, and it illuminates the complete screen. In this case, a diffractive method can be used to measure the phase modulation. The FT of the function implemented in SLM1 appears on the plane corresponding to the SLM that implements the filter (SLM2 in figure 1). In order to make the measurements of the FT pattern without changing the correlation set-up, a mirror or a beam splitter is introduced between the first polarizer P1 and the second half-wave plate HWP2 to deviate the beam. In the FT plane obtained outside the correlator, a radiometer is placed to measure light intensity values.

Amplitude modulation is measured by addressing a uniform screen on the SLM. All the energy is concentrated on the centre in the FT plane and it is a direct measure of the intensity transmission. Amplitude modulation is obtained by square root of the intensity transmission. In order to measure the phase modulation we use a diffraction technique proposed by Zhang *et al.* [16]. If a Ronchi grating is implemented on SLM1, characteristic diffraction orders are obtained on the FT plane. If two grey levels  $g_1$  and  $g_2$  are addressed to the SLM, the Ronchi grating will have two amplitude transmission levels  $t_1$  and  $t_2$ , and a relative phase shift  $\varphi$  between them. Except for a constant factor, the amplitude of the zero and first diffraction orders, namely  $A_0^s$ ,  $A_1^s$  and  $A_{-1}^s$ , can be expressed as a function of these parameters. The superscript s refers to the scene SLM (SLM1 in figure 1). They are given by the following expressions:

$$A_0^s = t_1 + t_2 \exp(i\varphi), \quad (1a)$$

$$A_1^s = \frac{2i}{\pi} [t_1 - t_2 \exp(i\varphi)], \quad (1b)$$

$$A_{-1}^s = -\frac{2i}{\pi} [t_1 - t_2 \exp(i\varphi)]. \quad (1c)$$

The intensities  $I_0^s$ ,  $I_1^s$  and  $I_{-1}^s$  of each diffraction order are given by

$$I_0^s = t_1^2 + t_2^2 + 2t_1t_2 \cos(\varphi), \quad (2a)$$

$$I_1^s = I_{-1}^s = \frac{4}{\pi^2} [t_1^2 + t_2^2 - 2t_1t_2 \cos(\varphi)]. \quad (2b)$$

The relative phase modulation can be expressed as a function of the grey levels  $g_1$  and  $g_2$  by the relation

$$\cos(\varphi) = \frac{R(g_1, g_2) - c}{T(g_1, g_2) - cR(g_1, g_2)}, \quad (3)$$

where  $R(g_1, g_2) = (I_0^s - I_1^s)/(I_0^s + I_1^s)$  is a relative measure of the intensities of the zero and first diffraction orders,  $T(g_1, g_2) = 2t_1t_2/(t_1^2 + t_2^2)$  is a factor that depends on the amplitude modulation, and  $c = (\pi^2 - 4)/(\pi^2 + 4) = 0.4232$  is a constant. Usually, grey level 0 is taken as a reference and the Ronchi grating has two grey levels: zero and a variable  $g$ . The phase modulation curve  $\varphi(g)$  is then obtained from the values of  $\cos(\varphi)$  with  $g_1 = 0$  and  $g_2 = g$ . Because of the multiple possible values of  $\varphi$  for each value of the  $\cos(\varphi)$  function, phase modulation  $\varphi$  is obtained from  $\cos(\varphi)$  by requiring that  $\varphi(0) = 0$  and by requiring the continuity of the phase modulation function with  $g$ .

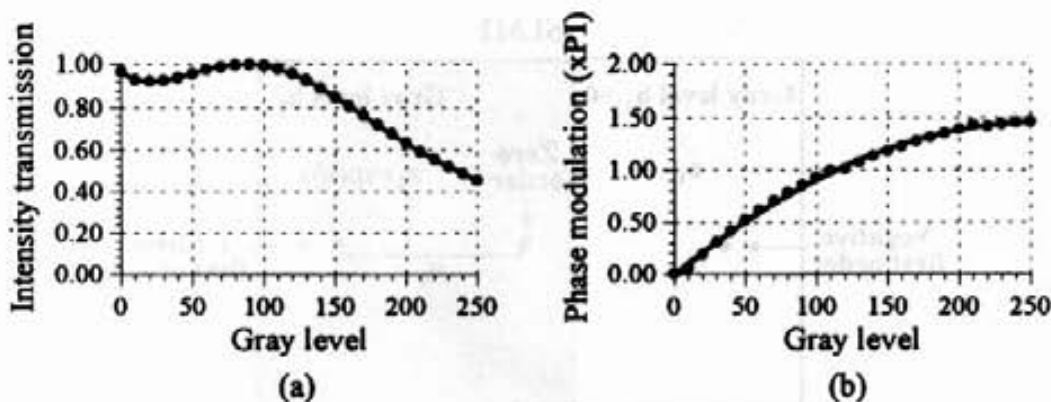


Figure 2. Modulation of SLM1 against grey level: (a) intensity transmission; (b) phase modulation.

Figure 2 shows the modulation results obtained with this technique. Control potentiometers of the Epson videoprojector are set to positions brightness 0, contrast 10 and colour 5. The incident beam is selected to be linearly polarized parallel to the liquid-crystal director at the input surface of the SLM. The output polarizer is placed with its transmission axis parallel to the director at the exit surface of the SLM. Figure 2(a) shows the intensity transmission against the grey level  $g$ , while figure 2(b) shows the phase modulation. Phase is an increasing function with grey level and in this case it has a maximum phase depth equal to  $1.5\pi$ . This configuration could be used in the scene of the correlator to implement phase encoded scenes, but with a coupled amplitude modulation.

#### 4. In-situ characterization of the filter spatial light modulator

Amplitude modulation of the SLM that implements the filter (SLM2 in figure 1) is obtained by measuring its intensity transmission, in the same way as for SLM1. However, the light beam converges towards the SLM2 plane and, consequently, the previous method used for measuring phase modulation of the scene SLM cannot be applied. In this case, for SLM2 phase modulation measurement, an interferometric technique can be used. If a Ronchi grating is implemented on the SLM1 with two grey levels  $g_1$  and  $g_2$  which correspond to amplitude transmissions  $t_1$  and  $t_2$  and a relative phase shift  $\varphi$ , then the diffraction orders are obtained in the SLM2. The frequency of the Ronchi grating is chosen in such a way that only the zero and the  $\pm 1$  orders fall inside the SLM2. These three diffraction orders act as point sources that produce an interference pattern over the charge-coupled device (CCD) camera. By changing the different voltages applied to the zones of SLM2 where these points are located the fringe pattern changes. We propose a method to measure the phase of the SLM2 by adding two interference patterns. Note that, as the incident beam in SLM2 comes from the first part of the correlator, it has exactly the same polarization orientation as it has in the correlation experiment.

The complex amplitude distribution in the plane just before SLM2 can be written as

$$E(u, v) = A_{-1}^s \delta(u - u_0, v) + A_0^s \delta(u, v) + A_1^s \delta(u + u_0, v), \quad (4)$$

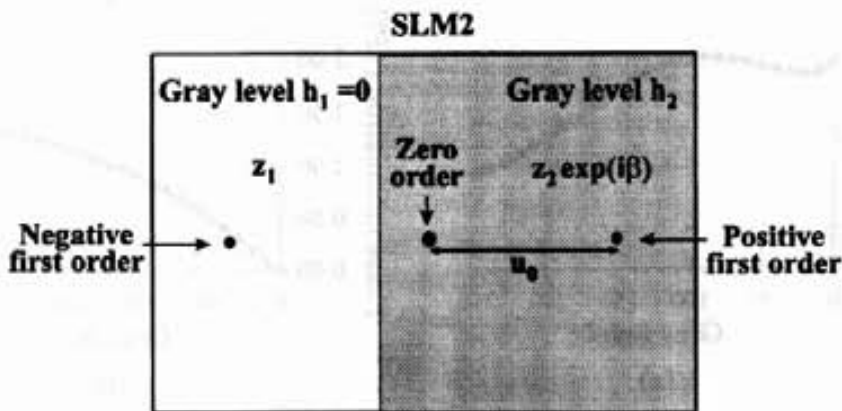


Figure 3. Distribution of the diffraction orders on the SLM2. Diffraction order  $-1$  is over a zone with grey level  $h_1 = 0$ , while  $0$  and  $+1$  orders are located over a zone with grey level  $h_2$ .

where  $A_{-1}^s$ ,  $A_0^s$  and  $A_1^s$  are the complex amplitudes given by equations (1 a), (1 b) and (1 c) respectively, and  $u_0$  is the distance between the central and the lateral point sources, which depends on the Ronchi grating frequency, the wavelength of the light and the distance between SLM1 and SLM2. Note that the superscript s still refers to scene SLM because these diffraction orders correspond to the Ronchi grating addressed to SLM1.

If the amplitude transmissions  $t_1$  and  $t_2$  are equal and the phase difference is  $\varphi = \pi$ , the term  $A_0^s$  in equation (1 a) is zero, and in consequence only two point sources are projected in the SLM2. In this case the method is similar to the methods proposed in [14] and [15] to characterize a SLM. However, it may happen that these conditions could not be obtained with the SLM used to display the image in the correlator.

The SLM2 screen is divided into two zones (figure 3), in such a way that the negative first order is placed over the first zone addressed with grey level  $h_1$ , while the zero and positive first orders are placed over a zone addressed with a grey level  $h_2$ . The amplitude transmissions of each zone are denoted by  $z_1$  and  $z_2$ , while the phase modulation difference between them is denoted by  $\beta$ . The complex amplitude distribution in the plane just behind SLM2 is then given by

$$E(u, v) = A_{-1}^s z_1 \delta(u - u_0, v) + A_0^s z_2 \exp(i\beta) \delta(u, v) + A_1^s z_2 \exp(i\beta) \delta(u + u_0, v). \quad (5a)$$

Henceforth, the amplitudes of the diffraction orders will be written in polar form, that is  $A_0^s = a_0 \exp(i\alpha_0)$ ,  $A_1^s = a_1 \exp(i\alpha_1)$  and  $A_{-1}^s = -a_1 \exp(i\alpha_1)$ . Then, equation (5 a) becomes

$$E(u, v) = -a_1 z_1 \exp(i\alpha_1) \delta(u - u_0, v) + a_0 z_2 \exp(i\alpha_0 + i\beta) \delta(u, v) + a_1 z_2 \exp(i\alpha_1 + i\beta) \delta(u + u_0, v). \quad (5b)$$

The intensity of the FT of this distribution can be captured by the CCD camera of the correlator. It will be a pattern given by the interference of the beams coming from each point source, and it is given by

$$I_1^f = (a_0 z_2)^2 + (a_1 z_2)^2 + (a_1 z_1)^2 + 2a_0 a_1 z_2^2 \cos(\alpha_0 - \alpha_1 + 2\pi u_0 x) - 2a_0 a_1 z_1 z_2 \cos(\beta + \alpha_0 - \alpha_1 - 2\pi u_0 x) - 2a_1^2 z_1 z_2 \cos(\beta - 4\pi u_0 x), \quad (6)$$

where the superscript f refers to filter SLM characterization. This distribution consists of a constant term plus three interference patterns. Two patterns have a period equal to  $1/u_0$  and they are shifted proportionally to the value  $\beta$ . The third pattern has a period equal to  $1/2u_0$ .

If the two grey levels used in SLM1 to produce the Ronchi grating are interchanged, the amplitude  $A_0^s$  does not change, but  $A_1^s$  and  $A_{-1}^s$  change their signs. Consequently, if  $g_1$  and  $g_2$  are interchanged in SLM1, the interference pattern captured by the CCD camera will change to

$$\begin{aligned} I_2^f = & (a_0 z_2)^2 + (a_1 z_2)^2 + (a_1 z_1)^2 - 2a_0 a_1 z_2^2 \cos(\alpha_0 - \alpha_1 + 2\pi u_0 x) \\ & + 2a_0 a_1 z_1 z_2 \cos(\beta + \alpha_0 - \alpha_1 + 2\pi u_0 x) - 2a_1^2 z_1 z_2 \cos(\beta - 4\pi u_0 x). \end{aligned} \quad (7)$$

By adding these two interference patterns (equations (6) and (7)), a new distribution is obtained, given by

$$I^f = I_1^f + I_2^f = 2(a_0 z_2)^2 + 2(a_1 z_2)^2 + 2(a_1 z_1)^2 - 4a_1^2 z_1 z_2 \cos(\beta - 2\pi u_0 x). \quad (8)$$

This is a single interference pattern with a period equal to  $1/2u_0$ . The fringes are shifted proportionally to  $\beta$ , the phase modulation of SLM2. The coupled amplitude modulations  $z_1$  and  $z_2$  corresponding to the grey levels  $h_1$  and  $h_2$  addressed to SLM2 affect the contrast of the fringes but does not affect their position. Consequently it is possible to measure the phase modulation of SLM2 by measuring the shift in the fringes observed after the addition of the two interference patterns  $I_1^f$  and  $I_2^f$ . Again, the grey level  $h_1 = 0$  is taken as the reference, and the grey level  $h_2$  is varied from 0 to 255.

Figure 4 shows experimental interference patterns obtained with this technique. Figure 4(a) is the pattern  $I_1^f$  obtained when SLM2 has a uniform screen with grey level 0, that is  $h_1 = h_2 = 0$ . Different fringe patterns are produced by the interference of the beams coming from each point source. Figure 4(b) corresponds to the interference pattern  $I_2^f$  obtained when grey levels  $g_1$  and  $g_2$  are interchanged in SLM1. Figure 4(c) is the result of the addition of the two previous patterns and it is observed that the interference pattern has the slope of a cosinus function, as in equation (8). If the procedure is repeated with the same grey levels  $g_1$  and  $g_2$  on SLM1, but with grey levels  $h_1 = 0$  and  $h_2 = 80$  on SLM2, we obtain two interference patterns the addition of which is shown in figure 4(d). A shift of about half a fringe is observed in the interference pattern with respect to figure 4(c), which corresponds approximately to a phase modulation  $\beta = \pi$ .

Figures 5(a) and (b) show a profile of the interference of figures 4(c) and (d) respectively. As can be observed, experimental fringe patterns are noisy. The determination of fringe displacements becomes inaccurate because of the difficulty in determining the position of the maxima. In order to evaluate more precisely the shift between the experimental fringe patterns, say  $I^f(0)$  and  $I^f(h)$  (figures 5(a) and (b)) we calculate the autocorrelation of  $I^f(0)$  (figure 5(c)) and we compare it with the correlation between  $I^f(0)$  and  $I^f(h)$  (figure 5(d)). Figure 5(d) has the same shape as figure 5(c), but shifted the same value (in periods) as the original fringe displacement (figure 5(b) with respect to figure 5(a)). Because of noise reduction, this method provides a more precise way to obtain the fringe shift than to measure it directly from the interference pattern.

Figure 6 shows experimental modulation results obtained with this technique for the filter SLM. Figure 6(a) corresponds to the intensity transmission while

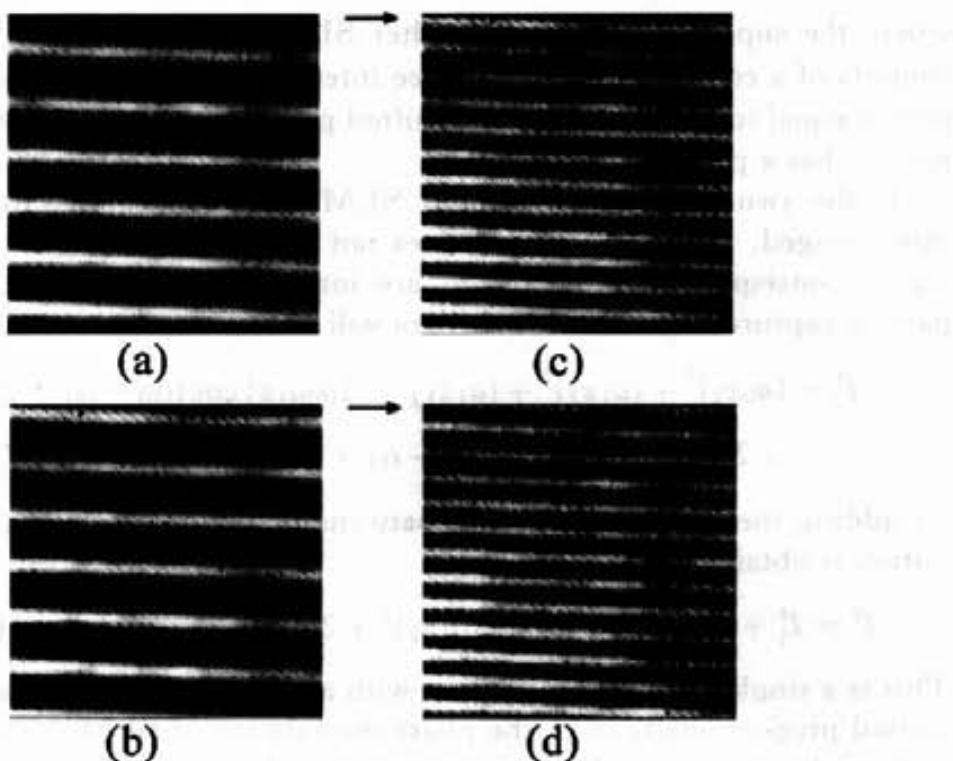


Figure 4. (a) Interference pattern  $I_1^f$  obtained when a Ronchi grating with grey levels  $g_1$  and  $g_2$  is implemented on SLM1 and a uniform screen of grey level 0 is addressed to SLM2; (b) interference pattern  $I_2^f$  obtained when the levels  $g_1$  and  $g_2$  of the grating implemented on SLM1 are interchanged; (c) addition  $I_1^f + I_2^f$ ; (d) addition  $I_1^f + I_2^f$  obtained when SLM2 has two zones with grey levels 0 and 80. A shift of half a fringe is observed with respect to (c). The arrows indicate the same pixel on the CCD camera.

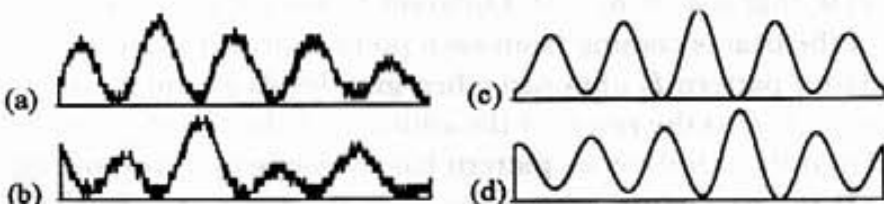


Figure 5. Profiles of two experimental interference fringe patterns for two different configurations of SLM2: (a) grey levels  $h_1 = 0$  and  $h_2 = 0$ ; (b) grey levels  $h_1 = 0$  and  $h_2 = 100$ ; (c) autocorrelation of the fringe pattern (a); (d) correlation between fringe patterns (a) and (b).

figure 6 (b) corresponds to the phase modulation. The control potentiometers have been placed at positions brightness 0, contrast 10 and colour 10. The phase modulation depth of this SLM reaches a maximum value of  $1.7\pi$ . The coupled amplitude modulation is very strong, mainly for high grey levels. This kind of modulation can be used to implement a phase-only filter, but the restriction in the phase modulation ( $1.7\pi$  maximum phase modulation) and the coupled amplitude modulation will cause its response to deteriorate.

## 5. Full adaptation to operating curves

Once the complete characterization of the two SLMs of the correlator has been performed, it is possible to adapt the system in order to improve the correlation.

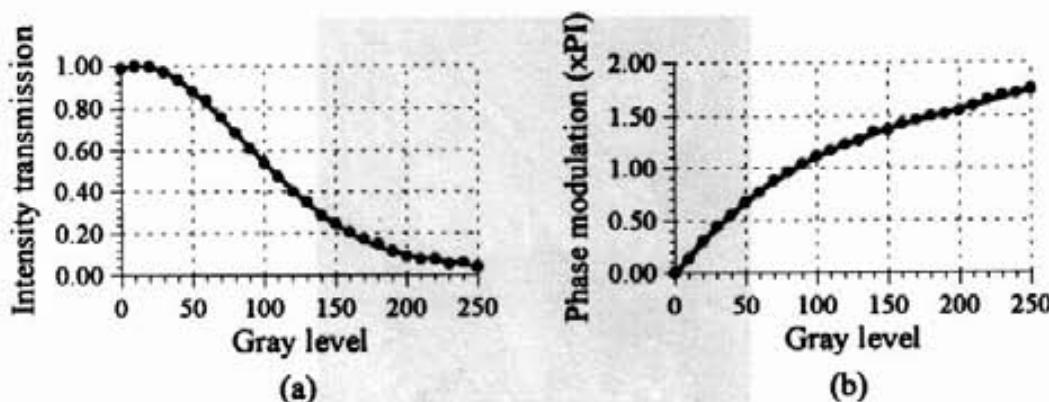


Figure 6. Modulation of SLM2 against grey level: (a) intensity transmission; (b) phase modulation.

The first step considered is to match the filter to the target object modified by the modulation curve of the SLM1. As shown in section 2, SLM1 produces good phase modulation, allowing phase encoding of the input scene [5]. Let  $s(x, y)$  represent the input amplitude scene, that is it is a function in the range  $[0, 1]$ . Let  $h(x, y)$  represent the target object to be recognized on the scene. The phase-encoding algorithm consists in transforming the input signal  $s(x, y)$  into a phase-only signal  $s'(x, y)$  given by

$$s'(x, y) = \exp[ik\pi s(x, y)], \quad (9)$$

where the constant  $k$  is usually taken to be equal to one in order to keep the monotonicity of the input signal in the phase signal. The reference object  $h(x, y)$  is transformed in the same way giving the phase-only signal  $h'(x, y)$  to which the filter is matched. In our case, the filter used is the phase-only filter [4]. This filter is obtained by calculating the FT of the target object to be recognized (in our case the function  $h'(x, y)$ ) and by using the complex conjugated phase distribution. This phase-only distribution may be implemented by a SLM that produces phase-only modulation between 0 and  $2\pi$ . When the phase-encoded scene and the phase-only filter are used, the correlator is optimal in terms of light efficiency.

When using real SLMs it is difficult to obtain perfect phase-only modulation. In this section we shall show firstly a numerical simulation of the experimental correlation process obtained with real SLMs. When the signal  $s(x, y)$  is addressed to the SLM1 it is converted into a signal  $s'_{\text{SLM}1}(x, y)$  different from the phase-only signal  $s'(x, y)$ . If the operating curve of SLM1 is taken into account in the filter generation, the phase-only filter can be matched to the simulation  $h'_{\text{SLM}1}(x, y)$  instead of being matched to the signal  $h'(x, y)$ . To illustrate the effect of the coding of the scene in the correlation results, the image shown in figure 7 has been used. The target object is the butterfly at the top of the figure. Figure 8 shows computer simulations obtained using as the input scene the function  $s'_{\text{SLM}1}(x, y)$  implemented by SLM1. Figure 8(a) corresponds to the case where a phase-only filter is matched to the function  $h'(x, y)$ , that is the reference object encoded as a perfect phase function. Figure 8(b) corresponds to the case where a phase-only filter is matched to the function  $h'_{\text{SLM}1}(x, y)$ . As expected, the perfect match of the phase-only filter gives a higher correlation peak, resulting in easier detection. The value of the maximum of the correlation peak is indicated on each figure.

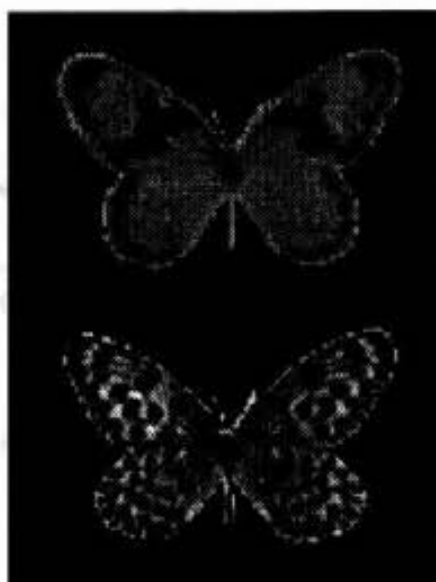


Figure 7. Input scene. The target object is the butterfly at the top of the figure.

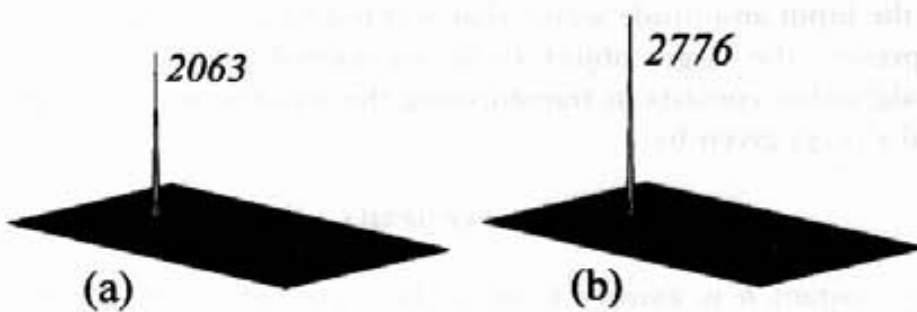


Figure 8. Computer simulation results using the scene  $s'_{\text{SLM}1}(x, y)$  and a phase-only filter matched to (a) a phase-encoded function  $h'(x, y)$  and (b) a function  $h'_{\text{SLM}1}(x, y)$ .

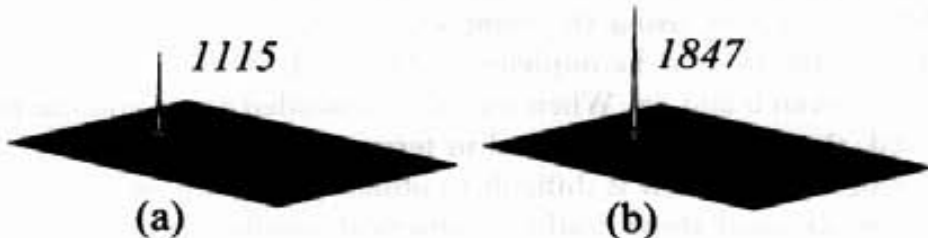


Figure 9. Computer simulation results using the scene  $s'_{\text{SLM}1}(x, y)$  and (a) a phase-only filter matched to the phase-encoded function  $h'(x, y)$  and directly implemented on SLM2, and (b) a phase-only filter matched to the function  $h'_{\text{SLM}1}(x, y)$  and implemented on SLM2 following the minimum-Euclidean-distance algorithm.

In the previous results, we have simulated a perfect phase-only filter. However, as pointed out in section 4, the phase modulation of SLM2 is restricted to a maximum depth of  $1.7\pi$  and has an important coupled amplitude modulation. These restrictions will cause the correlation distribution to deteriorate. The optimal implementation of a given filter in a restricted coding domain is given by the Euclidean projection of every complex point to its closest point belonging to the coding domain [8, 9]. Figure 9 shows computer simulation results obtained when the operating curves of SLM1 and SLM2 are considered. The input scene is

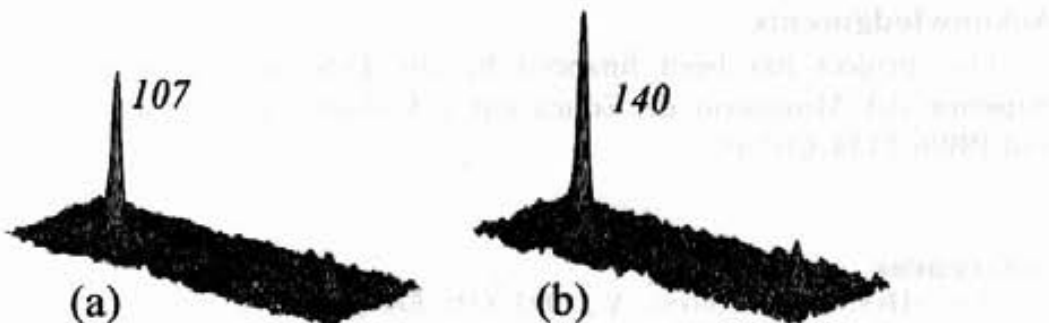


Figure 10. Optical correlation results: (a) filter matched to the phase-encoded function  $h'(x,y)$ ; (b) filter matched to the function  $h'_{SLM1}(x,y)$  and implemented on SLM2 following the minimum-Euclidean-distance algorithm.

the function  $s'_{SLM1}(x,y)$  implemented by SLM1. Figure 9(a) corresponds to the case in which the phase-only filter is matched to the function  $h'(x,y)$ , and it is addressed directly to SLM2. Because the operating curve of SLM2 is not a phase-only curve, the correlation peak is reduced with respect to the value in figure 8(a). Figure 9(b) corresponds to the case where the phase-only filter has been matched to the function  $h'_{SLM1}(x,y)$  and it has been adapted to the SLM2 operating curve following the minimum Euclidean distance algorithm. A higher correlation peak is obtained, although it does not reach the value obtained with a perfect phase-only filter (figure 8(b)).

Finally, the correlator has been used for optical correlation experiments. Figure 10(a) shows the experimental correlation obtained when the filter is matched to the phase-encoded function  $h'(x,y)$ . Although SLM1 does not produce a phase-only modulation, a good correlation peak is obtained. Figure 10(b) corresponds to the case in which the phase-only filter is matched to the function  $h'_{SLM1}(x,y)$  and it is implemented on SLM2 with the minimum Euclidean distance algorithm. An improvement in the correlation is observed and the value of the autocorrelation peak increases about 30%. These experimental results confirm the numerical results shown in figure 9.

## 6. Conclusions

Methods for performing *in-situ* characterization of the two SLMs of a Vander Lugt correlator are presented. The scene and filter SLMs require different methods because the conditions of illumination are different in each case. In the case of the scene SLM the whole screen is illuminated and a diffractive method can be used. The measured modulation is the mean response of all pixels of the SLM. On the other hand, the filter SLM is illuminated by a converging beam. An interferometric method is more convenient. We proposed and demonstrated a technique to measure the phase modulation of the filter SLM that uses three point sources generated by a grating implemented on the scene SLM. Finally, it has been demonstrated both numerically and experimentally that an adaptation of the correlation process to the operating curves of both SLMs produces higher correlation peaks.

## Acknowledgments

This project has been financed by the Dirección General de Enseñanza Superior del Ministerio de Educación y Cultura, projects PB96-1134-C02-01 and PB96-1134-C02-02.

## References

- [1] PAUL-HUS, G., and SHENG, Y., 1993, *Opt. Engng.*, **32**, 2165.
- [2] EFRON, U., 1995, *Spatial Light Modulator Technology: Materials, Devices and Applications* (New York: Marcel Dekker).
- [3] MORENO, I., CAMPOS, J., GORECKI, C., and YZUEL, M. J., 1995, *Jap. J. appl. Phys.*, **34**, 6423.
- [4] HORNER, J. L., and GIANINO, P. D., 1982, *Appl. Optics*, **23**, 812.
- [5] KALLMAN, R. R., and GOLDSTEIN, D. H., 1994, *Opt. Engng.*, **33**, 1806.
- [6] STYCZYNSKI, K., CAMPOS, J., YZUEL, M. J., and CHALASINSKA-MACUKOW, K., 1995, *Optics Commun.*, **118**, 193.
- [7] COHN, R. W., and HORNER, J. L., 1994, *Appl. Optics*, **33**, 5432.
- [8] JUDAY, R. D., 1994, *Appl. Optics*, **32**, 5100.
- [9] LAUDE, V., and RÉFRÉGIER, PH., 1994, *Appl. Optics*, **33**, 4465.
- [10] MAZÉ, S., and RÉFRÉGIER, PH., 1994, *Appl. Optics*, **33**, 6788.
- [11] KIRSCH, J. C., GREGORY, D. A., THIE, M. W., and JONES, B. K., 1992, *Opt. Engng.*, **31**, 963.
- [12] LAUDE, V., MAZÉ, S., CHAVEL, P., and RÉFRÉGIER, PH., 1992, *Optics Commun.*, **103**, 33.
- [13] YAMAUCHI, M., and EIJI, T., 1992, *Opt. Rev.*, **2**, 24.
- [14] SOUTAR, C., MONROE, S. E., JR, and KNOPP, J., 1994, *Opt. Engng.*, **33**, 1061.
- [15] BERGERON, A., GAUVIN, J., GAGNON, F., GINGRAS, D., ARSENAULT, H. H., and DOUCET, M., 1995, *Appl. Optics*, **34**, 5133.
- [16] ZHANG, Z., LU, G., and YU, F. T. S., 1994, *Opt. Engng.*, **33**, 3018.
- [17] McLAIN, J. L., JR., ERBACH, P. S., GREGORY, D. A., and YU, F. T. S., 1996, *Opt. Engng.*, **35**, 951.
- [18] SERRANO-HEREDIA, A., LU, G., PURWOSUMARTO, P., and YU, F. T. S., 1996, *Opt. Engng.*, **35**, 2680.
- [19] LU, K., and SALEH, B. E. A., 1990, *Opt. Engng.*, **29**, 6423.
- [20] GONÇALVES-NETO, L., ROBERGE, D., and SHENG, Y., 1995, *Appl. Optics*, **34**, 1944.
- [21] VANDER LUGT, A., 1992, *Optical Signal Processing* (New York: Wiley).

# Depth of focus increase by multiplexing programmable diffractive lenses

C. Iemmi

Departamento de Física, Facultad de Ciencias Exactas y Naturales, Universidad de Buenos Aires, 1428 Buenos Aires, Argentina.  
[iemmi@df.uba.ar](mailto:iemmi@df.uba.ar)

J. Campos, J. C. Escalera, O. López-Coronado, R. Gimeno and M. J. Yzuel

Departamento de Física, Universidad Autónoma de Barcelona, 08193 Bellaterra, Spain.  
[Juan.Campos@ub.edu](mailto:Juan.Campos@ub.edu)

**Abstract:** A combination of several diffractive lenses written onto a single programmable liquid crystal display (LCD) is proposed for increasing the Depth of Focus (DOF) of the imaging system as a whole. The lenses are spatially multiplexed in a random scheme onto the LCD. The axial irradiance distribution produced by each lens overlaps with the next one producing an extended focal depth. To compare the image quality of the multiplexed lenses, the Modulation Transfer Function (MTF) is calculated. Finally we obtain the experimental Point Spread Functions (PSF) for these multiplexed lenses and experimental results in which an extended object is illuminated under spatially incoherent monochromatic light. We compare the images obtained in the focal plane and in some defocused planes with the single lens and with three multiplexed lenses. The experimental results confirm that the multiplexed lenses produce a high increase in the depth of focus.

©2006 Optical Society of America

**OCIS codes:** (50.1970) Diffractive optics; (230.3720) Liquid-crystal devices; (230.6120) Spatial Light Modulators; (220.3620) Lens design.

---

## References and links

1. H. Fukuda, "A new pupil filter for annular illumination in optical lithography," *Jpn. J. Appl. Phys.* **31**, 4126-4130 (1992).
2. R. Hild, M. J. Yzuel and J. C. Escalera, "High focal depth imaging of small structures," *Microelectron. Eng.* **34**, 195-214 (1997).
3. G. G. Yang, "An optical pickup using a diffractive optical element for a high-density optical disc," *Opt. Commun.* **159**, 19-22 (1999).
4. H. Wang and F. Gan, "High focal depth with a pure-phase apodizer," *Appl. Opt.* **40**, 5658-5662 (2001).
5. W. T Welford, "Use of annular aperture to increase focal depth," *J. Opt. Soc. Am. A* **50**, 749-753 (1960).
6. Z. S Hegedus, "Annular pupil arrays. Application to confocal scanning," *Opt. Acta* **32**, 815-826 (1985).
7. J. C. Escalera, M. J. Yzuel and J. Campos, "Control of the polychromatic response of an optical system through the use of annular color filters," *Appl. Opt.* **34**, 1655-1663 (1995).
8. C. J. R. Sheppard and Z. S. Hegedus, "Axial behaviour of pupil-plane filters," *J. Opt. Soc. Am. A* **5**, 643-647 (1988).
9. C. S. Chung and H. H. Hopkins, "Influence of non-uniform amplitude on PSF," *J. Mod. Opt.* **35**, 1485-1511 (1988).
10. J. Ojeda-Castañeda, E. Tepichin and A. Díaz, "Arbitrarily high focal depth with quasióptimum real and positive transmittance apodizer," *Appl. Opt.* **28**, 2666-2670 (1989).
11. J. Ojeda-Castañeda, L. R. Berriel Valdos and E. Montes, "Spatial filter for increasing the depth of focus" *Opt. Lett.* **10**, 520-522 (1985).
12. M. J. Yzuel, J. C. Escalera and J. Campos, "Polychromatic axial behavior of axial apodizing and hyperresolving filters," *Appl. Opt.* **29**, 1631-1641 (1990).

13. J. Ojeda-Castañeda and L. R. Berriel-Valdos, "Zone plate for arbitrarily high focal depth," *Appl. Opt.* **29**, 994-996 (1990).
  14. G. Indebetow and H. Bai, "Imaging with Fresnel zone pupil masks: extended depth of field," *Appl. Opt.* **23**, 4299-4302 (1984).
  15. J. Davis, J. C. Escalera, J. Campos, A. Márquez, M. J. Yzuel and C. Iemmi, "Programmable axial apodizing and hypersolving amplitude filters with a liquid-crystal spatial light modulator" *Opt. Lett.* **24**, 628-630 (1999).
  16. A. Márquez, C. Iemmi, J. Campos, J. C. Escalera, and M. J. Yzuel, "Programmable apodizer to compensate chromatic aberration effects using a liquid crystal spatial light modulator," *Opt. Express* **13**, 716-730 (2005).
  17. A. Márquez, C. Iemmi, J. C. Escalera, J. Campos, S. Ledesma, J. Davis and M. J. Yzuel, "Amplitude apodizers encoded onto Fresnel lenses implemented on a phase-only spatial light modulator" *Appl. Opt.* **40**, 2316-2322 (2001).
  18. T. R. M Sales and G. M. Morris, "Diffractive superresolution elements," *J. Opt. Soc. Am. A* **14**, 1637-1646 (1997).
  19. S. Ledesma, J. C. Escalera, J. Campos, and M. J. Yzuel, "Evolution of the transverse response of an optical system with complex filters," *Opt. Commun.* **249**, 183-192 (2005).
  20. W. T Cathey, E. R. Dowski, "New paradigm for imaging systems," *Appl. Opt.* **41**, 5658-5662 (2001).
  21. E. Ben-Eliezer, Z. Zalevsky, E. Marom and N. Konforti, "All-optical extended depth of field imaging system," *J. Opt. A: Pure Appl. Opt.* **5**, S164-S169 (2003).
  22. A. Márquez, C. Iemmi, J. Campos, and M. J. Yzuel, "Achromatic diffractive lens written onto a liquid crystal display," *Opt. Lett.* **31**, 392-394 (2006).
  23. A. Márquez, C. Iemmi, I. Moreno, J. A. Davis, J. Campos and M. J. Yzuel, "Quantitative prediction of the modulation behavior of twisted nematic liquid crystal displays based on a simple physical model," *Opt. Eng.* **40**, 2558-2564 (2001).
- 

## 1. Introduction

Many optical systems need a long Depth of Focus (DOF). For instance, in optical microlithography high DOF is needed to obtain a stable image in the photoresist [1, 2]. High density optical data storage requires high-numerical aperture (NA) lenses and short wavelengths. But increasing NA and decreasing wavelength, the DOF decreases rapidly. So, different techniques are used to improve the axial response [3-4].

Different optical methods have been used to increase the depth of focus. Annular pupils produce an increase both of the DOF and the resolution [5-7] at the expense of an increase in sidelobes and loss of light. Non-uniform transmission filters have been also proposed to increase DOF [8-11], also with polychromatic illumination [12]. In that line, a zone plate with a prespecified number of foci [13], which are separated axially by Rayleigh's limit of resolution was proposed to create arbitrarily high DOF. Fresnel zone pupil masks have been also used [14]. It was demonstrated that amplitude-transmitting filters for apodizing and hyperresolving applications can be implemented with a two-dimensional programmable liquid-crystal spatial light modulator (LCSLM) operating in an amplitude-only mode [15,16] or they can be encoded onto Fresnel lenses on a phase-only SLM [17]. In all these cases, the loss of light is the main drawback.

In an effort to improve light throughput efficiency, different works have studied phase only filters. In some cases, the main goal is to obtain transverse superresolution [18]. The possibility of improving DOF using phase only filters has also been investigated [4]. The transverse response at defocused planes produced by complex filters with high focal depth was studied in [19]. Cathey et al [20] proposed a two step procedure: first a phase element apparently degrades the image, but a digital post-processing treatment improves the DOF. In methods like this, it is important that there is no loss of spatial frequencies in the first step in order to recover later all the image information. The increase of the DOF was obtained in [21] in a one step all-optical system, consisting of a lens plus a non-absorptive composite phase mask (CPM), consisting of several spatially multiplexed Fresnel lenses. In this paper only simulated results were presented. In other cases the phase element is produced in a liquid crystal spatial light modulator. For instance, in [22] it was proposed a programmable diffractive lens written onto a liquid crystal display that is able to provide equal focal lengths

for several wavelengths simultaneously. An appropriate lens for each wavelength was designed, and these lenses were spatially multiplexed onto the LCD.

In this paper we propose a combination of several diffractive lenses written onto a single programmable LCD. The lenses are spatially multiplexed in a random scheme onto the LCD. The axial irradiance distribution produced by each lens overlaps with the next one producing an extended focal depth. The global effect is an increase in the DOF. In section 2 we describe the technique used to multiplex the lenses. We also study the Modulation Transfer Function (MTF) produced by the single lens and the different multiplexed lenses, in order to compare the image quality. In section 3 we show experimental results of the Point Spread Function (PSF) and also of different tests with extended objects for the single lens and the multiplexed lenses. These results confirm the feasibility of multiplexing lenses to increase the DOF.

## 2. Multiplexed lenses

### 2.1 Lenses design

As we previously mentioned the aim of this work is to propose a method to increase the depth of focus of a diffractive lens. It is well known that by means of programmable spatial light modulators it is possible to control pixel by pixel the phase distribution of a wave front [23]. Taking profit of this feature we propose a combination of several diffractive lenses written onto a single programmable liquid crystal display (LCD). Each lens is designed in such a way that lenses with consecutive focal lengths provide amplitude distributions along the axis that overlap. These lenses are spatially multiplexed. In a previous paper [22] we have shown that among the different multiplexing possibilities, random multiplexing give place to a system whose point spread function has reduced transversal sidelobes so, it is adequate to image extended objects.

Our LCD has VGA resolution (640 X 480 pixels) with a pixel width of 34  $\mu\text{m}$  and a pixel distance (from the center of one pixel to the center of the next one) of 41  $\mu\text{m}$ , then the generated lenses have a 480 pixels diameter which is equivalent to 19.68 mm. The sampling of a Fresnel lens causes the appearance of multiple lenses when the sampling frequency is lower than the Nyquist frequency. To avoid this effect we design lenses with a focal length of about 100 cm for the blue line of an Ar laser ( $\lambda = 458 \text{ nm}$ ).

In the random multiplexing technique the aperture is divided in sub apertures of  $P \times P$  pixels, each sub aperture will be randomly assigned to a different lens, and then the transmission of the pixels of this sub aperture is taken from the corresponding lens.

The random assignment is performed as follows. For each sub aperture of the pupil a random number  $k$  in the range  $(0, N]$  is generated. Let the number  $k$  fall in the range  $j - 1 < k \leq j$  with  $j$  an integer number. Then the phase values of the sub aperture pixels are taken from the lens  $j$ . In Fig. 1 we show a diagram of this technique for building a multiplexed lens with  $3 \times 3$  pixels sub apertures.

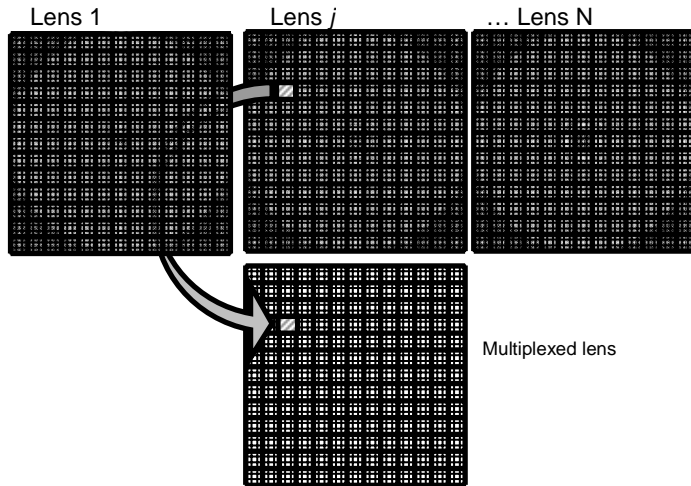


Fig. 1. Random multiplexing scheme. For each sub aperture a lens is chosen randomly and the transmission of its pixels assigned to the multiplexed lens.

In this work we have chosen sub apertures of  $1 \times 1$  pixel size to build three multiplexed lenses that cover a focal range from 92 cm to 108 cm, the first one (see Fig 2-b) resultant of multiplexing 9 lenses, the interval between consecutive focal lengths being 2 cm; a lens resultant of multiplexing 17 lenses, with 1 cm between consecutive focal lengths; and a lens resultant of multiplexing 33 lenses [see Fig. 2(c)] with a spacing of 0.5 cm between consecutive focal lengths.

In Figs. 2 (a)-2(c) we show a single lens (hereafter SL) with a focal length of 100 cm, a lens resultant of multiplexing 9 lenses (hereafter M9) with focal lengths ranging from 92 cm to 108 cm, i.e. the interval between consecutive focal lengths is 2 cm, and a lens resultant of multiplexing 33 lenses (hereafter M33) with focal lengths ranging from 92 cm to 108 cm, i.e. now the interval between consecutive focal lengths is 0.5 cm. This focal depth range has been chosen arbitrarily. Once we have chosen this focal range, we search for multiplexed lenses that produce an axial response as good as possible. We will show that we can implement a multiplexed lens with a number of lenses enough to produce a smooth (almost constant) axial response.

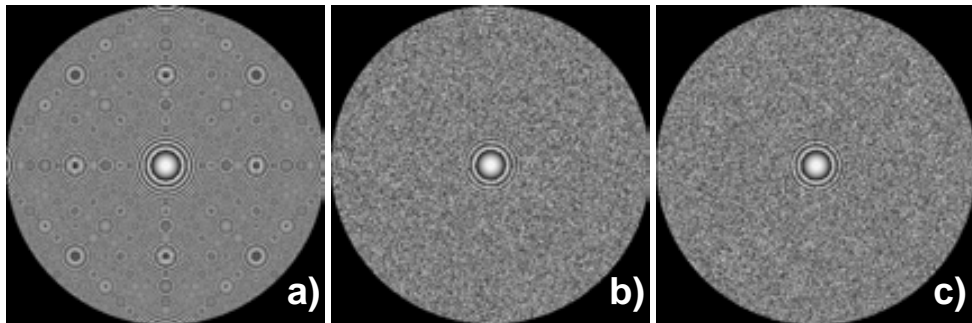


Fig. 2. (a) a single diffractive lens, (b) 9 lenses multiplexed and (c) 33 lenses multiplexed.

In principle the multiplexed lenses must produce focalizations at different planes since each of the constitutive lenses will focus in a different location. In order to study the effect of the random pupil and the defocused light on the final image, in the next subsection we will analyze the transfer function of these three diffractive elements.

## 2.2 Modulation Transfer Function of the multiplexed lenses

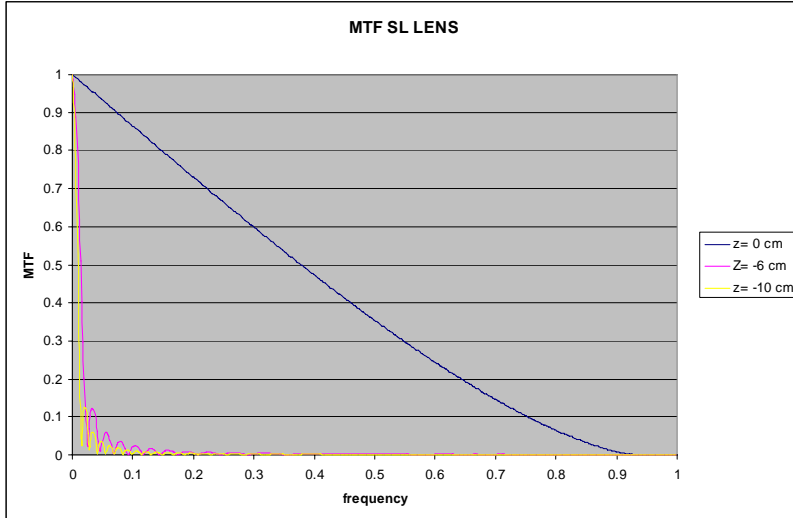


Fig. 3. MTF of the single lens in three planes

In order to compare the image quality of the SL lens with the M9 and M33 multiplexed lenses, we have calculated the Modulation Transfer Function (MTF) in the three cases. We have calculated the MTF in three planes, in the Best Image Plane (BIP, Z=0 cm) and in two arbitrary chosen defocused planes: Z= -6 cm and Z= -10 cm, (6 cm and 10 cm closer to the LCD respectively).

The MTF for a given multiplexed lens and for a focusing plane at a distance d from the lens is evaluated as follows. Let  $L(x,y) = \exp[i\phi(x,y)]$  be the phase transmission of the multiplexed lens. This matrix with an original size of 480x480 pixels is zero padded to a size of 1024x1024 pixels (it should have at least double size than the original and take a power of 2). This transmission is multiplied by the phase corresponding to the Fresnel propagation a distance d:  $F(x,y) = \exp[-(i\pi/\lambda d)(x^2 + y^2)]$ . The result is Fourier transformed. The modulus square of the result is the Point Spread Function (PSF) at a distance d from the lens. With a second Fourier transform the Optical Transfer Function (OTF) is obtained. In Figs. 3-6 section of the modulus of the OTF (MTF) are plotted. For the random multiplexed lenses only one realization (the one used in the experiments) is evaluated and for this reason, there are random fluctuations in the MTF (see Figs. 5 and 6).

Figure 3 shows the MTF produced by the SL lens. We can see a very good response in the Z=0 cm plane that is deteriorated strongly in the defocused planes.

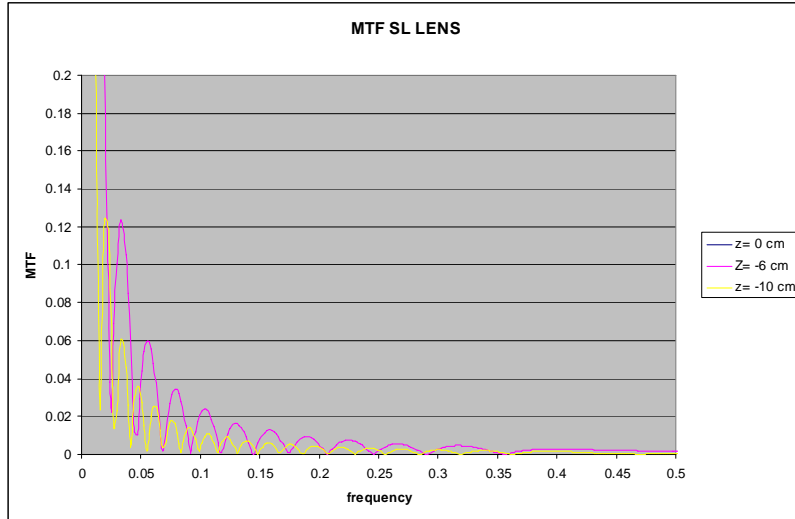


Fig. 4. MTF of the single lens in three planes (zoom of the region of interest)

Figure 4 shows a zoom of a region of interest in Fig. 3. We can see that in these range of spatial frequency there are a lot of contrast inversions. Each time that the MTF value is equal to 0, then a contrast inversion is produced. The image information that corresponds to those frequencies is lost, even if a post-processing is done. So, we expect a bad image quality in these defocused planes.

Figures 5 and 6 show the MTF produced by the M9 and M33 lenses respectively in the BIP ( $Z=0$ ) and in two defocused planes. If we compare Figs. 5 and 6 with Fig. 4 we see that the MTF in the BIP is obviously better for the SL. Both M9 and M33 lenses produce a strong descend in the MTF except for frequency 0. We expect a high background noise superposed to the object image. That can be appreciated in the experimental results shown in section 3. This background noise can be easily removed by subtracting a constant value to the whole image. This is the main drawback of the multiplexed lens, and a high dynamic range camera should be needed to capture correctly the image.

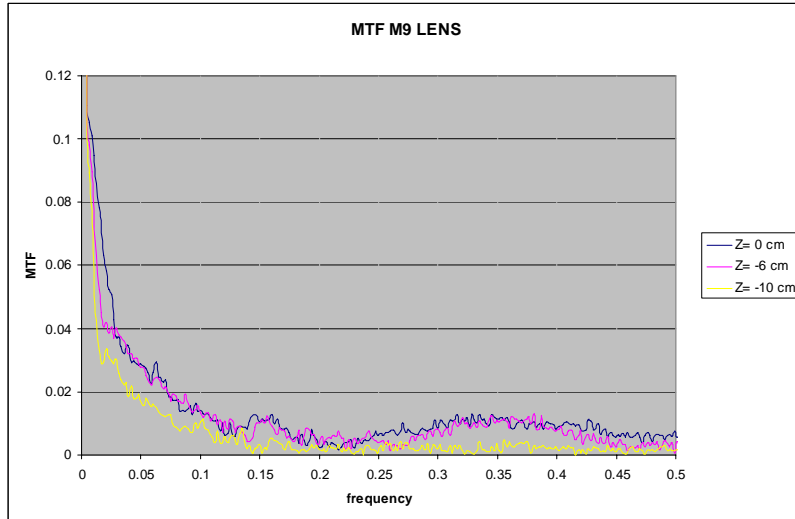


Fig. 5. MTF of the nine multiplexed lens in three planes

But an advantage is that both the M9 and M33 lenses produce a far better response in the defocused planes. The M9 (Fig. 5) lens does not produce contrast inversions in the [0-0.1] frequency region (the SL lens produces at least 4 contrast inversion in that region, see Fig. 4). Nevertheless, one contrast inversion is appreciated in the [0.1-0.2] frequency region and another in the [0.2-0.45] frequency regions for Z=0 cm and Z= -6 cm. The MTF of the M33 lens in the defocused planes is even better and there is a smooth decay with no trace of contrast inversions in the whole [0-0.5] frequency region. So, we expect an image improvement in the defocused planes, especially with the M33 lens with respect to the SL lens. This behaviour is experimentally studied in the next section.

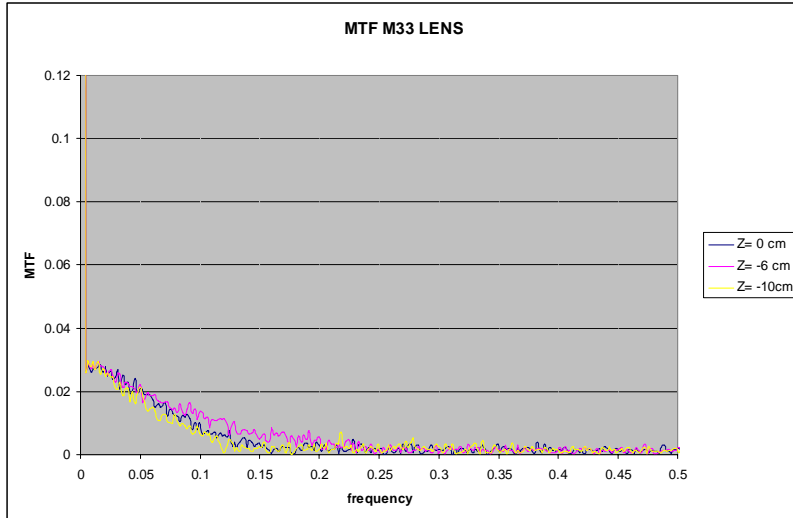


Fig. 6. MTF of the 33 multiplexed lens in three planes

### 3. Experimental results

#### 3.1 Optical set-up

A scheme of the experimental setup for imaging extended objects is shown in Fig. 7. The blue line of an Ar<sup>+</sup> laser ( $\lambda = 458$  nm) is used as light source. The laser beam impinges onto a ground glass rotating diffuser D and the object O is uniformly illuminated by means of the condenser C. The object is placed in the focus plane of lens L, in this way it is imaged in the focal plane of the diffractive lens shown in the liquid crystal display LCD. The system composed by polarizer P1 and wave plate WP1 constitutes a polarization state generator, analogously the system composed by WP2 and P2 constitutes a polarization state detector. These sets together with the LCD conform a spatial light modulator. By following the optimization procedure proposed in [23] it is possible to obtain a configuration of polarization states that provides phase only modulation. In this work we use a Sony liquid crystal panel, model LCX012BL, extracted from a Sony videoprojector model VPL-V500. The phase shift dynamic range is close to 360° at 458 nm and the amplitude modulation is almost flat. For capturing the Point Spread Function (PSF), a spatial filter is situated between the laser and lens L. The diffuser D and the condenser C are withdrawn. The spatial filter produces the point source that is placed in the focus of lens L.

The images of the extended object and the PSF are captured by a cooled digital 14 bit CCD camera, model PCO.2000 with 2048x2048 pixels, 7.4x7.4  $\mu\text{m}^2$  pixel size. As we will see later, a high dynamic range camera is needed because some of the images contain a high background. With an 8 bit CCD camera this background would fill all the dynamic range of the camera and images with very low quality would be obtained.

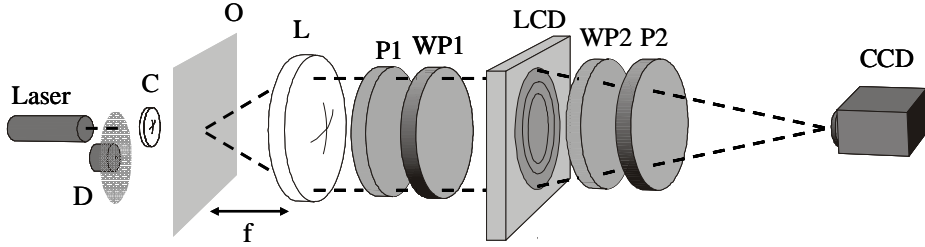


Fig. 7. Scheme of the imaging set-up for extended objects. D is a rotating diffuser, C a condenser, O is the object placed in the focal plane of lens L. P1 and P2 are polarizers, WP1 and WP2 are wave plates that together with the liquid crystal display LCD conform the pure phase modulator used to display the diffractive lenses. An image of O is captured by a CCD camera.

In order to compare experimentally the responses of the diffractive elements described in Section 2 we displayed the lenses onto the LCD and by shifting the CCD camera along the axis we registered the PSF of the system and the images of the extended object O at different planes in different experiments.

### 3.2 Point Spread Function of the multiplexed lenses

We have experimentally obtained the PSF of the SL, the M9 and the M33 multiplexed lenses, and of an additional intermediate multiplexed lens formed by 17 lenses (hereafter M17) with focal lengths ranging from 92 cm to 108 cm, with an interval of 1 cm between consecutive focal lengths, also designed as explained in section 2.1.

For each lens, we captured images of the point source along the optical axis and measured the intensity at the center of each image. It is shown in Fig. 8 the intensity profile along the axis for each lens. The axial intensity distributions produced by the SL lens and the M9, M17 and M33 lenses are shown in Fig. 8(a). In Fig. 8(b) we show in a different scale the intensity distributions produced by the M9, M17 and M33 lenses. It can be seen that M33 has the most smooth and constant profile through the axis, while maintaining a good DOF. On the contrary, in M17 and M9 the intensity shows more variations due to the increase on the distance between the different focuses. We can estimate the DOF looking for the Full Width at Half Maximum (FWHM) in Fig. 8(a). Figure 8(a) shows that the FWHM for the single lens is about 10 mm. Figure 8(b) shows that the FWHM for the M33 is about 200 mm. It is important to note that only the M33 lens produces a sufficient uniform axial response to consider that the DOF has been enhanced. This study suggests that the M33 is the best solution to obtain a high focal depth in the chosen axial region.

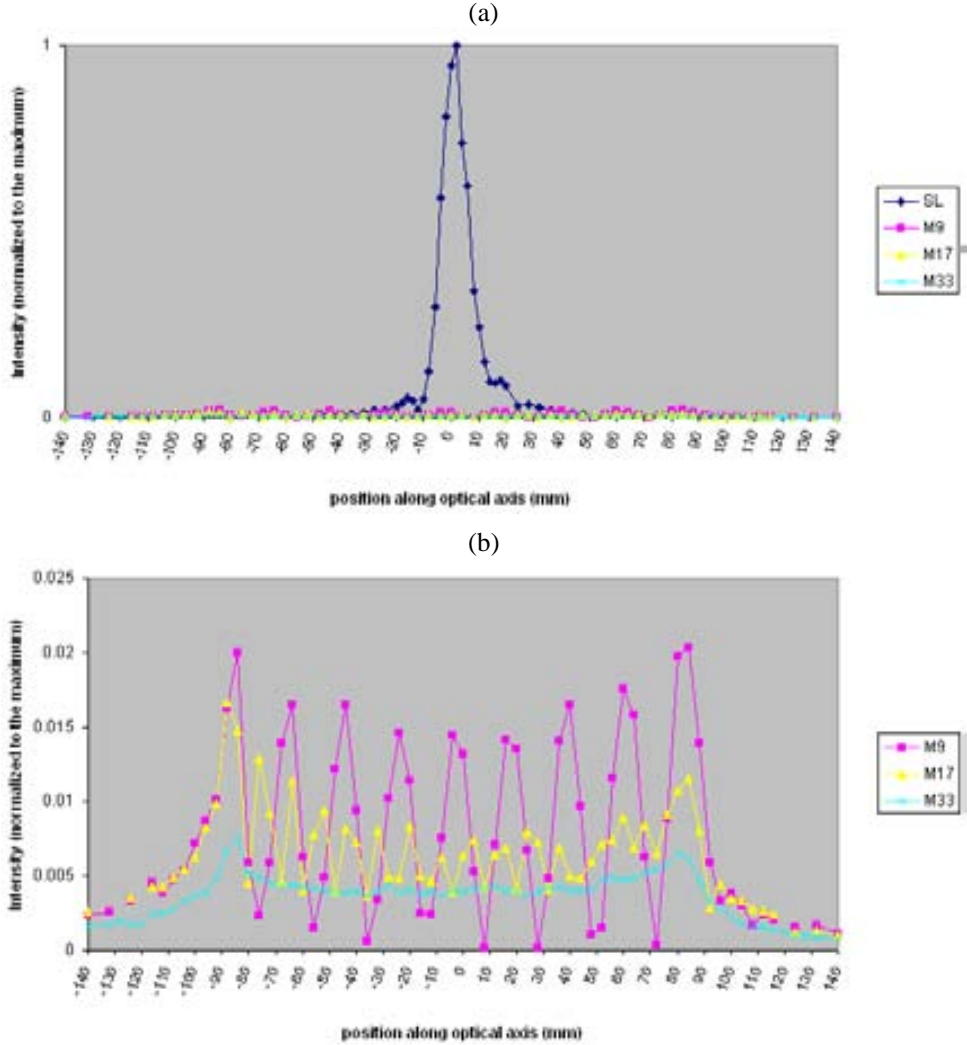


Fig. 8. Intensity profile of the PSF along the axis for SL, M9, M17 and M33 lenses (a); and for just M9, M17 and M33 lenses (b). Position  $Z=0$  corresponds to Best Image Plane (BIP)

Figure 9 shows experimental PSF at  $Z=0$  (BIP),  $Z=-6$  cm and  $Z=-10$  cm for each lens. The principal maximum of the PSF in the BIP for the M9, M17 and M33 lenses is wider than for the SL. This fact suggests that it will be a decrease of resolution in the BIP with the multiplexed lenses. The PSF in the planes  $Z=-6$  cm and  $Z=-10$  cm produced by the SL is almost null. On the contrary, the multiplexed lenses maintain a much better response in those planes.

It can be seen that M33 performs the most constant PSF along the axis, though resulting in a quite wide spot. On the other side, M9 performs alternatively focused and defocused PSFs, with M17 having an intermediate behavior.

If we compare the PSF in the BIP produced by the M9 and M33 lenses, we see that the M33 produces a more uniform PSF. The M9 produces a strong annular sidelobe that will deteriorate the image in the BIP. We will confirm this comparison with the study of the extended object images in the next section.

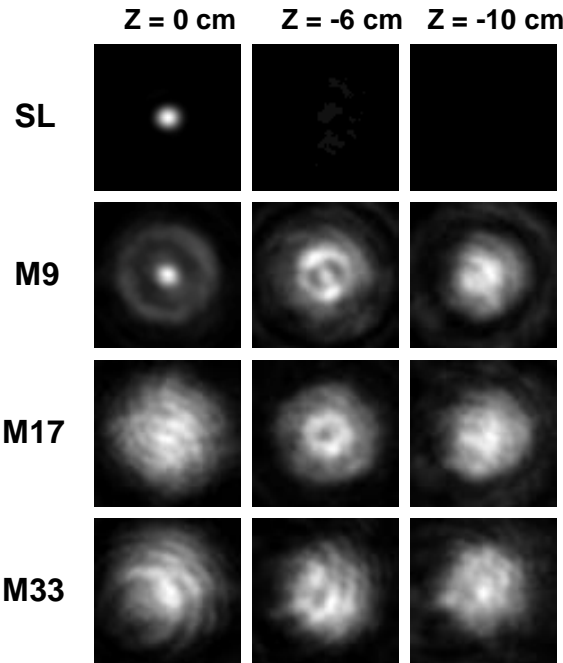


Fig. 9. PSF of the simple and multiplexed lenses, captured at three different planes.

### 3.3 Extended object images

We use in this experiment two types of objects: a Siemens star and a resolution target. In order to compare the responses of lenses with a different amount of multiplexed lenses we captured images of the Siemens star and the resolution target at  $Z = 0$  with the M9 and the M33 lenses. The results are summarized in Fig. 10.

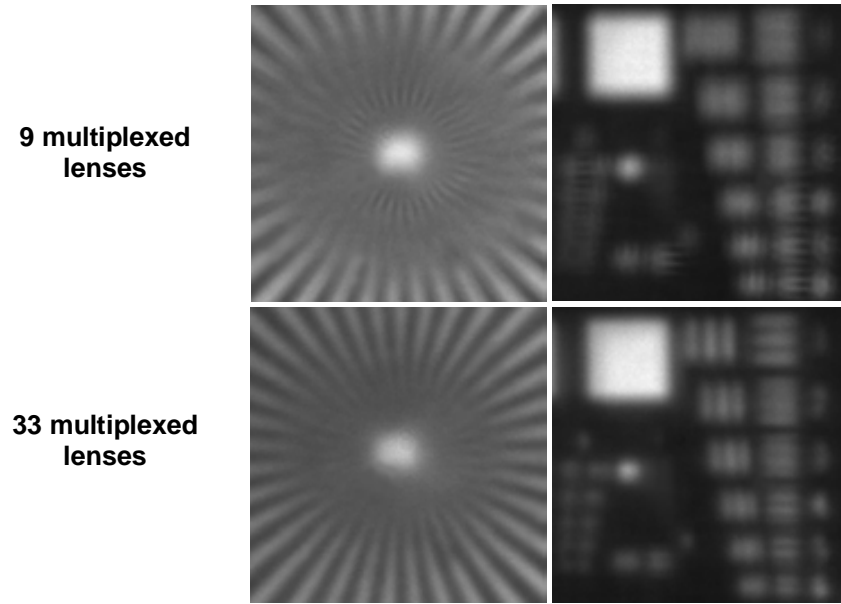


Fig. 10. Images of an enlarged portion of the Siemens star and the resolution test captured at  $Z = 0$  plane when 9 multiplexed lenses and 33 multiplexed lenses are used

It is noticeable from Fig. 10 that some contrast inversions are evident for the M9 lens and zero values for the MTF appear in this case. We can also observe that the M33 lens does not produce contrast inversions in those frequency regions. So, we conclude that the M33 produces a better response in the BIP. These results are in agreement with the MTF's shown in Figs. 5 and 6 and with the PSF's shown in Fig. 9.

Images of the Siemens star are shown in Fig. 11. They are obtained by using the single lens and the multiplexed 33 lenses. The best image plane (BIP) for the single lens is placed at 100 cm from the LCD, we will identify this plane with  $Z=0$ . We also show how the defocus degrades the image as the CCD is farther from that plane. Images were captured when the defocus is of -6 cm and -10 cm. When the multiplexed lens is used the images maintain their quality in the entire range of distances.

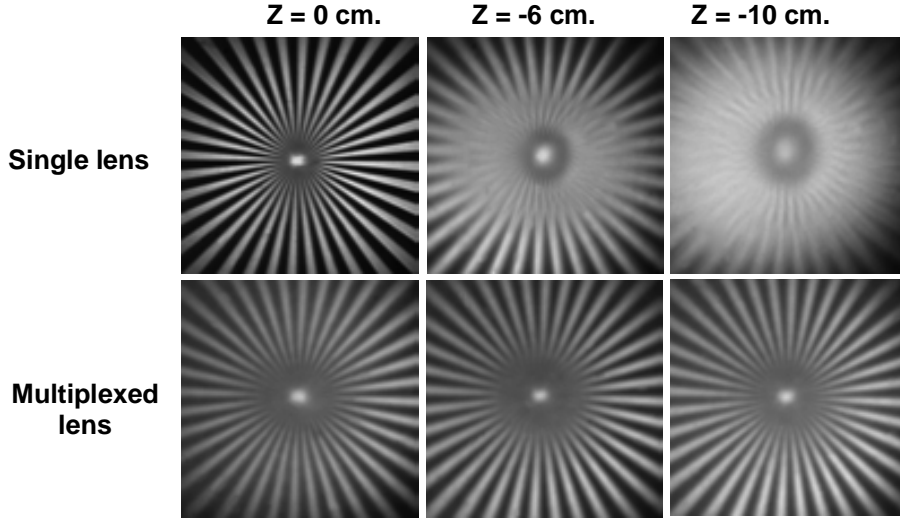


Fig. 11. Images of the Siemens star captured at the best image plane ( $Z = 0$ ) and defocused planes ( $Z = -6$  cm and  $Z = -10$  cm) when a single lens and a multiplexed lens (M33) are used.

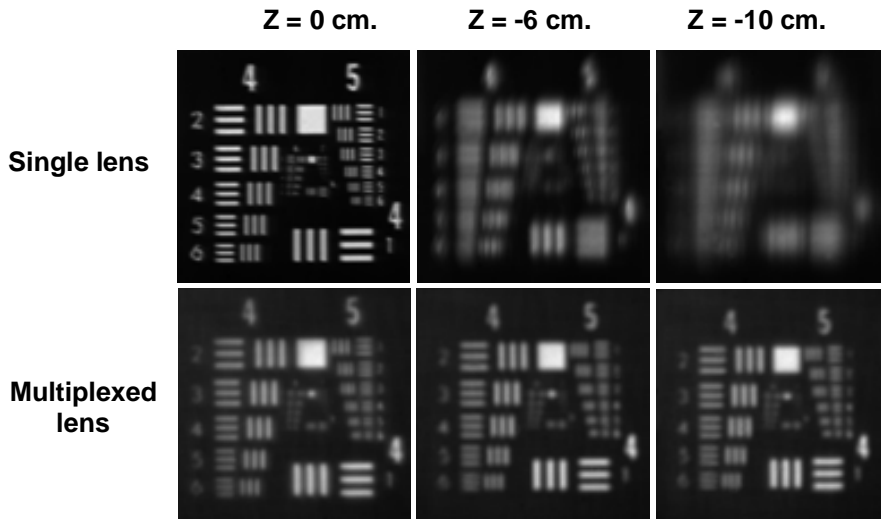


Fig. 12. Images of the resolution target captured at the best image plane ( $Z = 0$ ) and defocused planes ( $Z = -6$  cm and  $Z = -10$  cm) when a single lens and a multiplexed lens (M33) are used.

Images of the resolution target are shown in Fig. 12. They were captured in the same conditions as those corresponding to Fig. 11. It is clear that the M33 lens produces at  $Z=0$ cm lower contrast and there is some decrease in resolution compared with the single lens. Nevertheless, the tests are still focused at the planes  $Z= -6$ cm and  $Z= -10$  cm with the M33 lens. On the contrary, they appear blurred for the single lens in that defocused planes. It is interesting to remark, that the image of the resolution test for the M33 lens is very similar at the three planes. That means that the image quality (resolution, etc.) along the extended focal depth is maintained.

#### **4. Conclusions**

In this work we propose a combination of several diffractive lenses written onto a single programmable LCD to produce high focal depth. The lenses are spatially multiplexed in a random scheme onto the LCD. We choose an arbitrary focal range of 20 cm that is much wider than of the single lens (SL). Then, we study multiplexed lenses with different number of lenses to produce a good axial response. We show that the SL (single lens) produces a FWHM (full width at half maximum) of 1 cm, and the best multiplexed lens (M33) produces a FWHM of about 20 cm.

To analyze the quality of the image, different studies have been done. First, we compare the MTF of the single lens with that produced with the multiplexed lenses. In our case the multiplexing of 33 lenses (M33 lens) produces the best MTF in the defocused planes in comparison with the other multiplexed lenses. This MTF presents neither contrast inversions nor zero MTF values. Secondly, we have measured the PSF in different defocused planes to choose the multiplexed lens that produces the most constant PSF in the focal range. These experimental results show that in our case the M33 is the best solution. Thirdly, we compare experimental results with extended objects for the single lens and the M33 lens. These experimental results confirm that using this multiplexed lens the image quality with extended objects is very good in the defocused planes along the focal range.

#### **Acknowledgments**

We acknowledge financial support from the Spanish Ministerio de Ciencia y Tecnología (grant BFM2003-06273-C02-01/FISI) and from Generalitat de Catalunya (grant ACI2003-42). C. Iemmi gratefully acknowledges the support of the Universidad de Buenos Aires and Consejo Nacional de Investigaciones Científicas y Técnicas (Argentina).

# Tailoring the depth of focus for optical imaging systems using a Fourier transform approach

Jeffrey A. Davis and C. Stewart Tuvey

*San Diego State University, Department of Physics, San Diego, California 92182, USA*

Octavio López-Coronado, Juan Campos, and María J. Yzuel

*Departamento de Física, Universidad Autónoma de Barcelona, 08193 Bellaterra, Spain*

Claudio Iemmi

*Departamento de Física, Facultad de Ciencias Exactas y Naturales, Universidad de Buenos Aires, (1428) Buenos Aires, Argentina*

Received November 22, 2006; revised December 14, 2006; accepted December 14, 2006;  
posted January 19, 2007 (Doc. ID 77345); published March 5, 2007

We show how to tailor the depth of focus for an optical system using pupil functions obtained from a Fourier transform approach. These complex amplitude and phase pupil functions are encoded onto a single liquid-crystal spatial light modulator. Experimental results show excellent agreement with theory and indicate the power of this approach. © 2007 Optical Society of America

*OCIS codes:* 110.0110, 110.2990, 090.1970, 230.6120, 230.3720.

The transverse and axial imaging capabilities of optical systems can be improved by using specially designed pupil functions with such design goals as superresolution and extended depth of focus. An extremely powerful approach for studying axial imaging was first introduced by McCutchen,<sup>1</sup> where the axial intensity response near the focus is given by the one-dimensional Fourier transform of the radially symmetric pupil function expressed in  $r^2$  coordinates. The advantage of the Fourier transform formalism is that it gives some intuitive guidance for the design of new pupil functions. Although some theoretical results have been obtained with this formalism,<sup>2–4</sup> much of the theoretical effort has gone into numerical simulations in which various design parameters are optimized.<sup>5</sup>

Experimental results are surprisingly limited because of the difficulty in constructing these pupil functions. Binary phase diffractive optical elements,<sup>5,6</sup> consisting of annular rings, have been fabricated and produced good results. Amplitude pupil functions, consisting of polynomial series, have been encoded<sup>7,8</sup> onto liquid-crystal spatial light modulators (LCSLMs). More recently, combined amplitude and phase pupil functions were reported<sup>9</sup> in an attempt to increase the information encoded on the pupil function.

In this Letter we directly utilize the Fourier transform approach to generate pupil functions that create desired depth of focus distributions. Several goals are pupil functions that create a long uniform (rectangular) depth of focus, a triangular depth of focus where the intensity increases to a maximum at the focal point and then decreases, and finally a dual focus dependence consisting of two separated rectangular regions. These complex (amplitude and phase) pupil functions are then encoded onto a single LCSLM. In practice, we must use iterative techniques to overcome the limitations imposed by the limited number

of pixels on the LCSLM. Experimental results are extremely good.

Next we outline the theory of these pupil functions. We assume an axially symmetric lens function  $t(r)$  written as the product of a converging lens with focal length  $f$  and a complex pupil function  $p(r)$  as  $t(f,r) = p(r)\exp(-ikr^2/2f)$ . Using Fresnel diffraction and assuming axial symmetry, the scalar electric field at the origin of the viewing plane ( $x_2=y_2=0$ ) located a distance  $z \approx f$  from the input plane is given by

$$E(x_2=0, y_2=0, z)$$

$$= \frac{i}{\lambda z} \int_0^a p(r) \exp\left(\frac{-ikr^2}{2f}\right) \exp\left(\frac{ikr^2}{2z}\right) 2\pi r dr. \quad (1)$$

Here  $a$  is the radius of the pupil function. We ignore constant phase terms and  $k=2\pi/\lambda$ , where  $\lambda$  is the wavelength. We define normalized axial coordinates  $u=a^2/2\lambda z$  and  $u_0=a^2/2\lambda f$ . We approximate the leading  $1/z$  term by  $1/f$  (Ref. 10) to simplify the equation. In practice, this leads to an error of less than 4% that cannot be seen in the experimental results. Next we define the variable  $s=r^2/a^2-0.5$  that varies from -0.5 to +0.5. The integral is now symmetric with respect to the new origin and can be rewritten as a Fourier transform integral by extending the limits of integration to infinity as

$$E'(u) \approx \int_{-\infty}^{\infty} q(s) \exp(-i2\pi u_0 s) \exp(i2\pi u s) ds. \quad (2)$$

Here the pupil function is rewritten in terms of the new variables as  $q(s)$ .

Because the Fourier transform of the product of two functions is the convolution of their Fourier transforms, we rewrite the integral of Eq. (2) as

$$E'(u) \approx \delta(u - u_0) \otimes Q(u). \quad (3)$$

Consequently the axial electric field  $E'(u)$  is proportional to the Fourier transform  $Q(u)$  of the pupil function  $q(s)$  expressed in  $s$  coordinates. For a rectangular pupil function, the electric field is a sinc function in the  $u$  direction centered at the focal point of the lens. As the pupil aperture  $a$  decreases, the focus broadens along the  $z$  axis. We can relate the  $u$  and  $z$  dimensions by using  $u - u_0 \approx a^2(z - f)/(2\lambda f^2)$ .

The initial results using the fast Fourier transform (FFT) were good, but there were problems (such as the Gibbs overshoot in the rectangle response functions) because the pupil function is spatially limited by the size of our LCSLM. Consequently we used an iterative design procedure<sup>11,12</sup> as outlined in Fig. 1 to improve the results. Figure 1(a) shows the desired output axial response function  $E'(u)$  (a rectangle, for example). We use discrete Fourier transforms having  $N_1=512$  points (or samples) and define the axial response function over a limited region of  $m$  points (from  $u_1$  to  $u_2$ ). By performing the Fourier transform, we obtain the complex transmission of the pupil  $q(s)$  as shown in Fig. 1(b). We cannot use this entire distribution because of the finite size of the LCSLM. Consequently we truncate the pupil function to  $N_2=256$  points, where the regions outside the pupil ( $s_1-s_2$ ) are made equal to zero as shown in Fig. 1(c). By inverse Fourier transformation we obtain the axial distribution  $Q(u)$  in Fig. 1(d), and we find that it does not coincide with the desired one because of the restrictions mentioned above.

To improve the results, we impose additional restrictions. In the region  $(u_1-u_2)$  we restore the originally designed magnitude of the axial distribution. The axial phase distribution is used as a degree of freedom. Outside this region the magnitude is truncated if it exceeds a given percent (5% for this example) of the maximum magnitude in the region  $(u_1-u_2)$ . Then a new axial distribution is obtained. We continued the process until the mean square error was 0.01 (in the case of the double rectangle, we were limited to a value of 0.1). Typically this required about 1000 iterations. However, because of the efficiency of the FFT algorithm, this typically required a few seconds.

After this procedure is completed, the pupil function  $q(s)$  must be rescaled to the radial coordinates as  $p(r)$ . This rescaling spreads the central radial portion and compresses the outer parts. This compression can create problems because fast oscillations in the

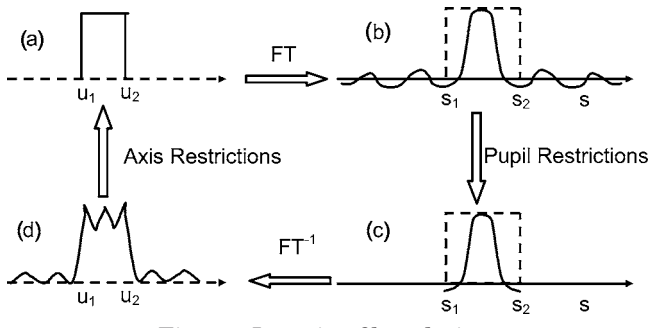


Fig. 1. Iterative filter design.

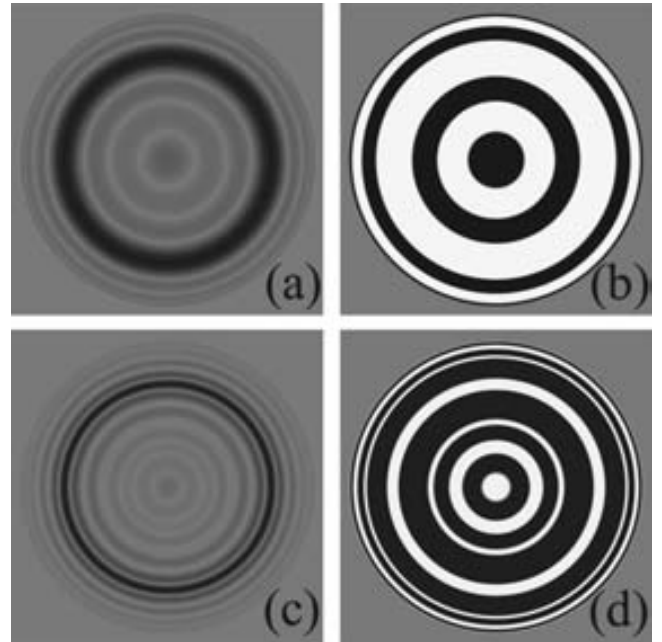


Fig. 2. Amplitude and phase distributions for functions that give an axial response: (a), (b) rectangle having 9 points; (c), (d) two 9-point rectangles separated by 21 points.

pupil function are difficult to encode onto the limited pixel structure of the LCSLM.

To demonstrate this approach, we designed several pupil functions. Figure 2 shows the amplitude and phase for pupil functions  $p(r)$  that yield a rectangular [Figs. 2(a) and 2(b)] and two-separated-rectangle [Figs. 2(c) and 2(d)] axial response functions. Using the simple Fourier transform relation between the widths of the rectangle and sinc functions, the axial distance in  $z$  coordinates is related to the number of samples in the rectangle function as

$$L = (2m\lambda f^2 N_2) / (N_1 a^2). \quad (4)$$

The experimental setup is similar to that reported earlier.<sup>8</sup> Linearly polarized light from an argon laser is spatially filtered, expanded, and collimated. The pupil functions are encoded onto a parallel-aligned nematic LCSLM manufactured by Seiko Epson with  $640 \times 480$  pixels having dimensions of  $42 \mu\text{m}$  on a 1.3 in. display.<sup>13</sup> Each pixel acts as an electrically controllable phase plate where the total phase shift exceeds  $2\pi$  rad as a function of gray level at the argon laser wavelength of 514.5 nm. The light is focused by a 38.1 cm focal length Space Optics Research Labs lens. Because the focal spot size from the lens is extremely small, we magnify it with a  $20\times$  microscope objective lens. We fix the distance between the microscope objective and the detector, and by shifting the assembly (objective plus CCD camera) along the axis, we measure the peak intensity in the transverse plane at different axial distances.

Our LCSLM is easily capable of encoding the phase information. Amplitude information is then encoded onto this phase-only medium by spatially modulating the phase pattern with the amplitude portion of the pupil function.<sup>14</sup> As the phase depth increases, the in-

tensity diffracted into the first order increases, while the zero-order intensity decreases. We first multiply the pupil function with a linear phase grating having a period  $d=6$  pixels. Now the total phase is the sum of the pupil phase term with the grating phase. Finally, we multiply this phase pattern by the magnitude of the pupil function so that the total phase is given by  $\exp[i|p(r)|[\phi(r)+2\pi x/d]]$ . Here the phase is in the range  $[-\pi, \pi]$ , and the amplitude is defined in the range  $[0 \leq |p(r)| \leq 1]$ .

Experimental results are shown in Fig. 3. Figure 3(a) shows the axial intensity distribution for a clear pupil having a radius of 10 mm. The depth of focus measured between the minima of the sinc-squared intensity distribution is 2.8 mm, in excellent agreement with theory. Figures 3(b)–3(d) show the axial distributions for a series of pupil functions having initial lengths of  $m=9, 21, 41$  points in the Fourier transform program. The depth of focus now increases up to 30 mm. Next we designed a pupil function to produce an electric field that varied axially as  $\sqrt{z}$  and a triangular intensity distribution with a length equivalent to 41 points. Figure 3(e) shows the experimental triangular intensity distribution. Finally, Fig. 3(f) shows the output where we programmed two rectangle functions having widths of 15 points separated by 25 points. Experimental error is about 10%, caused by fluctuations in the laser intensity and vibrations.

There are several limitations with this approach. The transmission efficiency of these pupil functions is

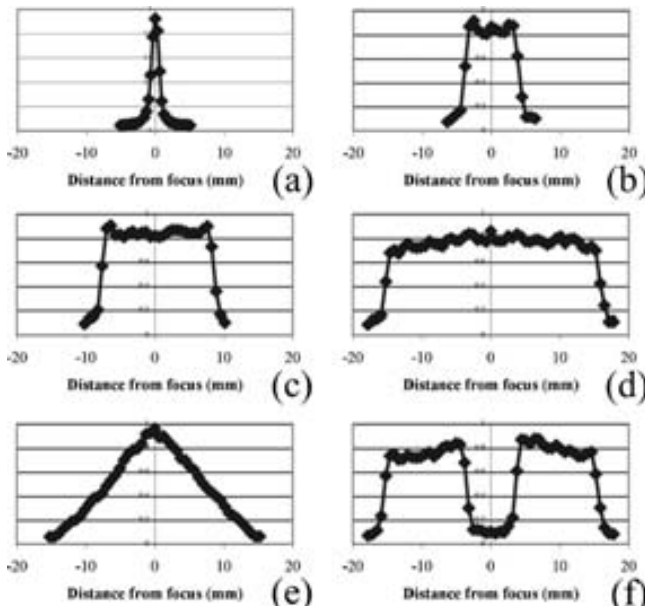


Fig. 3. Axial intensity response (arbitrary units) obtained for (a) uniform pupil, (b) 9 point rectangle, (c) 21 point rectangle, (d) 41 point rectangle, (e) triangle, (f) two 15 point rectangles separated by 25 points.

reduced because the complex pupils absorb some of the incident light. There are also difficulties in implementing the pupil function designs. As the length of the distribution in the  $u$  domain decreases, the information available for the pupil decreases—we have fewer sidelobes to encode. This causes low pass filtering of the output response. On the other hand, as the  $u$  domain length increases, the number of sidelobes increases. Now it is much more difficult to encode the rapidly varying pupil function (particularly when it is rewritten into the  $r$  domain) with the limited number of pixels.

Nevertheless, the experimental results are excellent and agree well with the predictions of Eq. (4). For the case of Fig. 3(c), we have extended the depth of focus by a factor of over 20 compared with the original open pupil. This approach shows the power of the Fourier transform formalism and shows that these kinds of complicated pupil functions can be easily constructed with a single LCSLM to obtain a desired axial response of an optical system.

We acknowledge financial support from the Spanish Ministerio de Ciencia y Tecnología (grant FIS2006-13037-C02-01). C. Iemmi gratefully acknowledges the support of the Universidad de Buenos Aires and Consejo Nacional de Investigaciones Científicas y Técnicas (Argentina). We thank Tomio Sonehara of Seiko Epson Corporation for the use of the LCD and Don Cottrell for his computer program. J. A. Davis's e-mail address is jdavis@sciences.sdsu.edu.

## References

1. C. W. McCutchen, *J. Opt. Soc. Am.* **54**, 240 (1964).
2. J. Ojeda-Castañeda, L. R. Berriel-Valdos, and E. Montes, *Opt. Lett.* **10**, 520 (1985).
3. J. Ojeda-Castañeda, E. Tepichin, and A. Diaz, *Appl. Opt.* **28**, 2666 (1989).
4. J. Ojeda-Castañeda and L. R. Berriel-Valdos, *Appl. Opt.* **29**, 994 (1990).
5. J. Jia, C. Zhou, Z. Sun, and L. Liu, *Appl. Opt.* **43**, 2112 (2004), and references therein.
6. H. Liu, Y. Yan, and G. Jin, *Appl. Opt.* **40**, 2316 (2001).
7. J. A. Davis, J. C. Escalera, J. Campos, A. Marquez, M. J. Yzuel, and C. Iemmi, *Opt. Lett.* **24**, 628 (1999).
8. A. Marquez, C. Iemmi, J. C. Escalera, J. Campos, S. Ledesma, J. A. Davis, and M. J. Yzuel, *Appl. Opt.* **40**, 2316 (2001).
9. P. N. Gundu and E. Hack, *Opt. Express* **13**, 2835 (2005).
10. M. V. Klein, *Optics* (Wiley, 1970), Chap. 9.3.
11. J. Rosen and J. Shamir, *Opt. Lett.* **16**, 752 (1991).
12. D. C. Youla and H. Webb, *IEEE Trans. Med. Imaging MI-1*, 81 (1982).
13. J. A. Davis, P. Tsai, D. M. Cottrell, T. Sonehara, and J. Amako, *Opt. Eng.* **38**, 1051 (1999).
14. J. A. Davis, D. M. Cottrell, J. Campos, M. J. Yzuel, and I. Moreno, *Appl. Opt.* **38**, 5004 (1999).